VARIATIONAL METHODS FOR MODELING AND SIMULATION OF TOOL-TISSUE INTERACTION

XIONG LINFEI

(B.Eng. Huazhong University of Science and Technology, China)

A THESIS SUBMITTED FOR THE DEGREE OF DOCTOR OF PHILOSOPHY

NATIONAL UNIVERSITY OF SINGAPORE

2014

DECLARATION

I hereby declare that the thesis is my original work and it has been written by me in its entirety.

I have duly acknowledged all the sources of information which have been used in the thesis.

This thesis has not been submitted for any degree in any university previously.

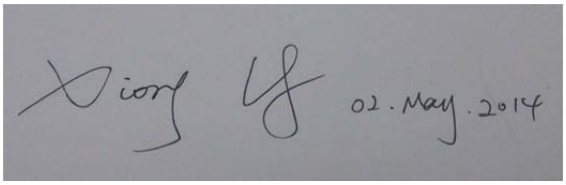

Xiong Linfei

02 May 2014

ACKNOWLEDGEMENT

First and foremost, I sincerely thank Dr. Chui Chee Kong and Prof Teo Chee Leong, my supervisors, for their enthusiastic and continuous support and guidance. I would send special thanks to Dr. Chui Chee Kong for his insightful suggestions and critical comments which are quite important to my PhD studies. During my PhD studies, he provided me not only with the technical guidance, but also strong encouragement and kind affection.

I am grateful to Mr. Chng Chin Boon, Mr. Yang Tao, Dr. Fu Yabo, Dr. Wen Rong and many other friends for their invaluable friendship, advice and help during my PhD studies. Without their help and encouragement, I would not have carried out this study smoothly.

I also thank Mr. Sakthi, Mrs. Ooi, Ms. Tshin and Mdm. Hamidah in the Control and Mechatronics Lab for their help.

I would especially thank my parents and wife. My hard-working parents have sacrificed their lives for my life and provided unconditional love and care. I love them so much, and I would not have made it this far without them. My wife has always stood by my side and I love her dearly and thank her for all her advice and support. Their love gives me the strength to move forward.

XIONG LINFEI

02 May 2014

Contents

Summary

Virtual reality based surgical simulators provide a safe and effective way for medical training, pre-operative surgical planning and robot assisted surgeries. One of the main constraints in the development of high-fidelity simulators is realistic modeling of medical procedures involving tool-tissue interaction. The soft tissue constitutive laws, organ geometry, and the shape of the surgical tool interacting with the organ are factors that affect the modeling realism of medical simulation. Nonlinear mechanical property is an important attribute of the soft tissue that needs to be considered in realistic deformation simulation. Using variational principles, this dissertation investigates nonlinear soft tissue deformation modeling and tool-tissue interaction simulation.

Since mechanical response of biological soft tissue always exhibits a large variance due to its complex microstructure and different loading conditions, a probabilistic approach was proposed to model the uncertainties in human artery tissue deformation. Material parameters of the artery tissue were represented by a statistical function with normal distribution. Mean and standard deviation of the material parameters were determined using Genetic Algorithm (GA) and inverse mean-value first-order second-moment (IMVFOSM) method respectively. This approach was verified using computer simulation with Monte-Carlo (MC) method and by comparisons between predicted results and experimental data. The resultant biomechanical model increases the accuracy of medical simulation as they explicitly takes into account the heterogeneity of the mechanical soft biological tissues. Mechanical properties of vascular tissue during division were studied. An optimization method was introduced to estimate the spring and damper parameters of the viscoelastic model. Experiments were performed on human iliac arteries with laparoscopic scissors, similar to the surgical task of cutting a blood vessel. The experimental data are modeled using linear viscoelastic constitutive equations.

Nonlinear mechanical behaviors of gallbladder tissue were investigated with GA based variational approach. Mechanical experiments on porcine

gallbladder tissue were performed to study tissue deformation. An exponential strain energy function with a new volumetric function was proposed to model the mechanical properties of gallbladder tissue. Comparisons between predicted deformation and that of the experimental data on gallbladder tissues demonstrate good applicability of this reality based variational approach. A surgical simulation system based on the variational approach was also developed with haptic guidance. Both the reaction force and guidance force are modeled with different priorities in the simulation system. The user is physically guided through the ideal motion path with a haptic device, giving the user a kinesthetic understanding of the task. The simulation system was applied in tracheal reconstruction surgery as well as an edutainment manipulation task on rubber duck.

Finally, a variational based computational approach was proposed to model degradation process of biodegradable clips. Biodegradable material is widely applied in wound closure surgeries as it can help to maintain wound closure until the wound is healed. The degradation process which considers both material and geometry of the device as well as its deployment was modeled as an energy minimization problem that was iteratively solved using active contour and incremental finite element methods. Strain energy of the micro-clip during degradation was modeled using active contour formulation. Degradation rate is calculated from strain energy using the proposed transformation. By relating strain energy to material degradation, the degradation process was simulated with a degradation map. The simulating results agreed with that of the in-vivo and in-vitro experimental results, which validated our work.

This dissertation presents an advanced study of biomechanical modeling of soft tissue using variational methods. The biomechanical models were successfully implemented in medical simulation for surgical training planning as well as medical device design.

List of Tables

List of Figures

List of Symbols

$:$	Inner product of two second-order tensors
∂	Partial differential
Σ	Summation
∇	Gradient
$\sqrt{\ }$	Square root
$\|\|$	Vector norm
$\int$	Integration
e	Euler number
$\min(\cdot)$	Minimum
$\ln(\cdot)$	Natural logarithm
$\exp(\cdot)$	Exponential function
$\sin(\cdot)$	Sine function
$\cos(\cdot)$	Cosine function

List of Abbreviations

ALE	Arbitrary-Lagrangian-Eulerian
BEM	boundary element method
CDF	cumulative distribution function
CT	computerized tomography
DC	direct calculating
EFFD	extended free form deformation
FE	finite element
FFD	free form deformation
GA	genetic algorithm
GVF	gradient vector flow
HTK	Histidine Tryptophan Ketoglutarate
IMVFOSM	inverse mean-value first-order second-moment
L-H	Legendre-Hadamard
MC	Monte Carol
MIS	minimally invasive surgery
MRA	magnetic resonance angiography
MRI	magnetic resonance imaging
PDE	partial differential equation
TL	total laryngectomy
VP	voice prosthesis

Chapter 1 Introduction

1.1 Background and motivation

For minimally invasive surgeries, surgeons are required to be highly skilled to perform the surgical operations [1]. Mastering and assessing operation skills for the doctors can be difficult. Medical simulation is particularly attractive in the field of surgical training because it avoids the participation of patients for skills practice and enables the trainees to be trained before treating humans [2]. Virtual reality based surgical simulators present a safe, realistic, and efficient way for surgical training, practice, and pre-operative planning. These simulators simulate human anatomy environment and generate realistic mechanical responses of human organs. Using medical simulators, new surgeons can improve their surgical skills after exercising on a variety of complex cases and receive feedback on their performance. Surgical simulation systems are also useful for pre- and intra-operative planning of medical procedures. Surgical and interventional radiology procedures often require a patient-specific plan prior to performing an operation. Thus, simulation systems which account for patient-specific anatomical details and tissue properties can benefit the surgeons as well as increase the accuracy of the surgical procedures [3, 4].

The key requirements in surgical simulation is establishing realistic human anatomical environment and presenting accurate biomechanical responses of organs during surgical procedures for the purposes of training, planning, and assessing patient outcomes in a risk-free environment [4]. Developing realistic virtual reality based surgical simulation system demands the acquisition of specific biomechanical tissue information, development of efficient computation strategies, employment of acceptable validation protocols, and integration of advanced haptic rendering technologies [5]. A high-fidelity surgical simulation system requires appropriately presentation of soft tissue deformation during interactions similar to that of actual surgical manipulations. The boundary conditions of soft tissues must be physically well defined and

their interactions with tools should be updated in real-time in order to create a realistic visual and haptic interface.

The nonlinear mechanical response is an important attribute of soft tissue properties which relates to simulation accuracy, and needs to be considered for deformation simulation and haptic rendering in surgical simulation. Experimental procedures such as inflation tests [6, 7], biaxial tests[8], as well as tension and indentation tests [9-12] have been performed to study the mechanical properties of soft biological tissue. These experiments showed that the mechanical behavior of soft biological tissue was elastic, highly nonlinear and anisotropic under finite strains, which is usually modeled within the framework of hyperelasticity.

However, for realistic surgical simulation, there exists a trade-off between computational speed and biomechanical simulation accuracy. Feedback from surgeons reveals that a bad simulator is worse than no simulation, they also insist that simulators must be realistic enough so that the errors are resulted from incorrect manipulation of surgeons but not from the virtual environment [13]. Relationship between computational speed and simulation accuracy for different applications are summarized in Figure 1.1. Scientific analysis is aiming at validating physical hypothesis of soft tissue for the design of new procedures or implants. In this case, the accuracy of deformation is far more important than computation time. On the other hand, surgery planning for predicting the outcome of surgery or rehearsing complex operations, requiring less computation time (from 30s to one hour) since several trials may be necessary. For surgical procedure training, computation time of the level of 0.1s is required in order to achieve smooth user interaction whereas the accuracy of deformation is not of primary importance [5]. In this dissertation, we put our efforts to investigate the nonlinear mechanical properties of biological soft tissue using computation approaches. The objective is to provide an effective approach for realistic modeling and simulation of tool tissue interaction. The findings of this work are utilized to build high-fidelity medical simulation system.

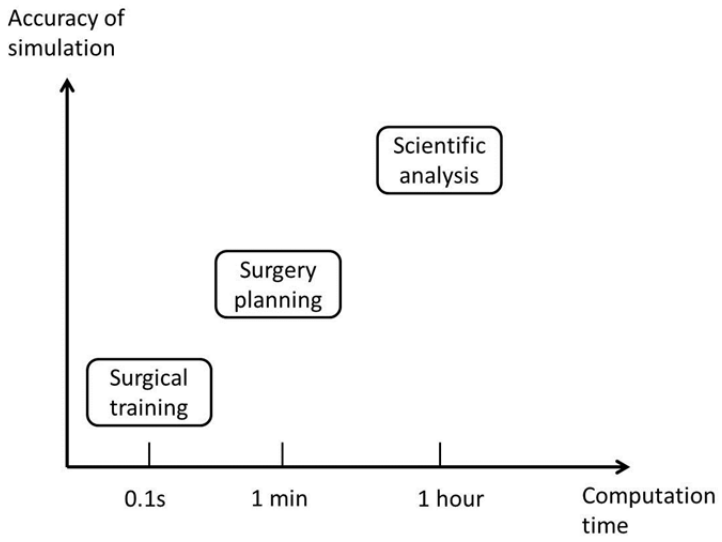

Figure.1.1 Time accuracy requirement of soft tissue modeling

1.2 Variational methods for soft tissue modeling

Many studies have been conducted to investigate the biomechanical models of soft tissue. Deformable models for soft tissue deformation can be classified into two categories: physics based and non-physics based. Physics based methods are based on continuum mechanical principles, and could obtain accurate simulation results by directly solving the partial differential equations (PDEs) using numerical or computational methods. Some of the prevailing methods include the Finite element (FE) method [14], boundary element method (BEM) [15], point-based method [16], and reduced model [17]. Non-physics based models use intuitive methods instead of solving PDE. For example, the mass-spring model [18] uses point masses connected by a network of springs to represent continuous material, and meshless shape matching model [19] computes deformations based on geometry shapes. Numerical or computational models based on mechanical engineering principles are employed to model the deformation of soft tissue realistically [20]. They aim to provide accurate soft tissue modeling results while reducing the computation cost. However, the balance between computational cost and accuracy remains a research problem.

Variational principles for biomechanical systems, such as elasto-viscoelastic behavior, have been known for a while, but have received renewed attention in

recent years. These principles can be written in a continuous or in an incremental framework. In particular, a variational formulation of constitutive models for standard generalized materials, including irreversible, dissipative, and possibly rate-dependent behaviors, was proposed [21, 22] initially in an isothermal context, and later extended to a fully coupled thermo-mechanical context in [23]. These variational approaches could provide appropriate mathematical basis for developing models of non-cohesive granular media [24], porous plasticity [25], and nonlinear finite viscoelasticity [26].

The variational models can serve as an appropriate compensatory method to model the nonlinear mechanical properties of soft tissue. Unlike the traditional finite element method that always needs to consider the boundary condition in interaction process, under the assumption of incompressible nonlinear body [27], variational methods can be used for modeling of nonlinear biological soft tissue deformation in the finite deformation regime. By defining the modeling problem as an energy minimization process, the material parameters of nonlinear model can be characterized within the variational framework. The approach is qualified as variational since the constitutive updates consist of a minimization problem within each load increment [26]. It displays great advantages when dealing with nonlinear materials in an inexpensive computationally way.

1.3 Organizations

The overall structure of the study takes the form of seven chapters, including this introductory chapter. Chapter 2 begins by reviewing the literature on surgical simulation in the context of nonphysical based and physical based models and variational modeling of soft tissue deformation. Chapter 3 describes the variational principles of this dissertation study. Chapter 4 presents an investigation on statistical modeling of the uncertainties of human artery tissue using probabilistic approach, and characterization of material parameters in human vascular soft tissue during division. Chapter 5 presents the study of constitutive laws for hyperelastic tissue and implementation for surgical simulation with haptic rendering, as well as surgical simulation in combination with haptic guidance. Chapter 6 discusses effects of strain energy

from tool-tissue interaction process on degradation mechanism of biodegradable materials. Finally, the thesis concludes in Chapter 7 with a discussion on future research in the area of realistic modeling of tool-tissue interactions.

1.4 Contributions

The major contributions of this dissertation are:

- **Quantitative study the uncertainties in mechanical properties of human arterial tissue using probabilistic approach**

With the variational principles, a new probabilistic approach was proposed to model the uncertainties of human arterial tissue deformation by assuming that the instantaneous stress at a specific strain varies according to normal distribution. Material parameters of the artery tissue were modeled with a combined logarithmic and polynomial energy equation and characterized with the experimental results obtained from human arteries. The statistical model is able to present the soft tissue properties accurately. The interaction between the uncertainty on the observations and the uncertainty on the estimated parameters is a major phenomenon to consider when using biomechanical models for medical simulation. By taking into account the inhomogeneous mechanical properties of human biological tissue, the study can contribute to realistic virtual simulation as well as an acceptable computational approach for medical device validation.

- **Variationally modeling the nonlinear mechanical properties of gallbladder organ and haptic implementation of the modeling results**

We investigated the variational principles for biomechanical modeling of gallbladder tissue. Mechanical experiments on porcine gallbladder tissue are carried out to investigate soft tissue deformation properties. An exponential strain energy function was proposed to describe the mechanical behavior of the gallbladder tissue while the material parameters were calibrated with a genetic algorithm based variational approach. The gallbladder tissue model is assigned with hyperelastic properties and implemented in a medical simulation

system with haptic feedback. The nonlinear tissue model provides a realistic material model for advanced surgical simulation.

- **Computation modeling of tool-tissue interaction process and their effects on degradation process of biodegradable materials**

Strain energy function is always accounting for the soft tissue deformation modeling. The degradation process of the biodegradable clips is assumed to be highly related to the strain energy on the clips resulted from tool-tissue interaction process. The tool-tissue interaction process between biodegradable clips and porcine vocal fold tissue was first modeled using FE analysis while the FE results were used to calculate the strain energy of the clips using active contour. Degradation process was defined as an energy minimization process and solved within the variational framework. The degradation rate and geometries of the clip during degradation was computed based on the physical energy, and calibrated by experimental results. This work presents a comprehensive study on the tool-tissue interaction and their effect on the degradation process of biodegradable materials.

Chapter 2 Literature Review

Surgical simulation creates an efficient and safe platform for new surgeons to gain necessary medical skills while reducing the needs for animals, cadavers, and patients [28]. A goal of surgical simulation is the generation of realistic human anatomical and physiological responses to surgical manipulations for the purposes of training, planning, and assessing patient outcomes in a risk-free environment [4]. It aims to assist medical practitioners by allowing them to visualize, feel, and be fully immersed in a realistic environment. The simulator should accurately represent the anatomical details and deformation of the organ as well as provide realistic haptic feedback of tool-tissue interaction.

Advanced modeling algorithms are important for accurate soft tissue deformation modeling and haptic force feedback. During the past decades, there has been growing interest in the medical and computer science field around the simulation of medical procedures [5]. Computational modeling and numerical methods have demonstrated their abilities in solving complex boundary value problems for soft tissue modeling [29]. Different algorithms have been proposed for computational modeling of soft tissue deformation. These algorithms can be divided into two categories: Non-physical based models, such as free form deformation [30] and deformable splines [31] which are based on pure mathematical representation of the object's surface and do not generally provide a realistic simulation of its mechanical behavior. Another category is physical based models, which can be classified into two types: Non-continuum mechanics based methods, e.g., mass-spring models [32] and continuum mechanics based methods, e.g., finite element methods [33]. This chapter will review the related works in soft tissue modeling.

2.1 Non-physical based computational methods

The non-physical computational methods for tool-tissue interaction modeling include free-form deformation methods [34] and deformable splines [35]. These algorithms are based on pure mathematical representation of the

object's surface, which fail to provide a realistic simulation of its mechanical behavior. In such cases, physical accuracy is sacrificed for computational efficiency and the system has no knowledge about the material properties of the object being deformed [36]. The mostly used non-physical based model is free form deformation model.

Free form deformation (FFD) is a space-warping technology that plays an important role in computer-assisted geometric design and soft tissue deformation animation [36]. Some useful deformation operations, which were independent of control points, were developed by Barr in 1984 [37]. Complex deformations, once achieved only by skilled and laborious manipulation of numerous control points, could now be presented by applying these operators to an object in a hierarchical fashion. However, the actions of Barr's model were constrained to against a single axis which reduces the potential of the model for complex structure modeling. The restrictions of the model made it only suitable for modeling of lattice shape.

To conquer the shape constraints of FFD, Extended Free Form Deformation (EFFD) was proposed by Coquillart [38]. It allows the user to define the shape of a lattice, which in turn induces the shape of the deformation. Animated Free-Form Deformation[39], in which the deformation tool differentiates itself from the object instead of interpolating the metamorphosis of the 3D lattice which lies around the deformable object, was also proposed by Coquillart for animating deformations. This technique allows reusing of deformations for other objects and provides better control over the deformation.

A hierarchical transformation model of the motion of the breast was developed by Rueckert [40] for non-rigid registration of contrast-enhanced breast MRI. The local breast motion was described by a FFD based B-splines while the global motion of the breast was modeled by an affine transformation. This FFD based non-rigid registration algorithm shows better performance to recover the motion and deformation of the breast than rigid or affine registration algorithms. Liver motion during respiratory cycle was studied by Rohlfing using an intensity-based FFD registration algorithm [41]. The intensity based non-rigid image registration approach can achieve a

satisfactory level in abdominal organ motion modeling. The intensity-based nonrigid registration algorithm was extended by using a novel regularization term to constrain the deformation for breast images registration [42]. The novel regularization term is a local volume-preservation (incompressibility) constraint, which is motivated by the assumption that soft tissue is incompressible for small deformations and short time periods. The intensity-based free-form non-rigid registration algorithm was improved by incorporation of the incompressible feature as it greatly reduces the problem of shrinkage of contrast-enhanced structures while allowing motion artifacts to be substantially reduced.

FFD enables smooth deformations of arbitrary structures, provides local control over deformations, and serves as a computationally efficient algorithm that is easy to implement. It can be extended in complex modeling work which is usually carried out with physical based models[43, 44].

B-spline solids are employed to model skeletal muscle for the purpose of building a data library of reusable, deformable muscles that are reconstructed from actual muscle data[45]. Techniques are developed to construct continuous representations of volume from discrete data. B-spline solids are represented as mathematical three-dimensional vector functions in order to obtain muscle fibre bundle orientations. As B-spline solids can be defined completely with its control points and knot vectors, they can require significantly less storage than a dense set of polygons.

Interphase correlation of the images during the respiratory process are studied with B-spline registration models, intermediate phases are interpolated by starting from two or three sets of 3D CT images acquired at different phase points[46]. It demonstrates that the organ deformation during the breathing process can be well modelled with a B-Spline deformable algorithm.

Deformable splines are also utilized in motion tracking for medical applications. By formulating model parameters as tensor products of B-splines, algorithms are proposed to quickly reconstruct left ventricle geometry/motion from extracted boundary contours and tracked planar tags in MR images [47].

Furthermore, a thin plate spline model is developed for representing the heart surface deformations[48]. The thin plate spline was extended to warp to the stereo scenario, enabling efficient 3D tracking of the beating heart using stereo endoscopic images. However, deformable splines are still quite complex and computationally costlier than spring-mass type models which will be introduced in next section, without actually offering better realism.

2.2 Physical based computational methods

This section discusses the physical based computational methods that are employed in medical simulation.

2.2.1 Non-continuum discrete models

Among the physical based models, the discrete models, such as the mass-spring systems[49] and Chain-mail representational models [50], are widely used in soft tissue deformation modeling due to their low computational cost and easily implementation [50-52]. Mass-spring models are usually utilized in soft tissue deformation for solving linear elastic problems. For elastic materials, Hooke's law represents the material behavior and relates the unknown stresses and strains in following constitutive equation.

$$\sigma = C : \varepsilon \tag{2.2.1}$$

where σ is the Cauchy stress tensor, C is the fourth-order stiffness tensor, ε is the infinitesimal strain tensor, and $A : B = A_{ij} B_{ij}$ is the inner product of two second-order tensors (summation over repeated indices is implied).

Many works have been done under the framework of linear elasticity using mass-spring models. Mass-spring models were first proposed to model facial deformation [53, 54]. These early works solve static problems of Hooke's law. After that, dynamic models were introduced to model skin, fat and muscle tissues [49, 55, 56]. Some studies have employed mass-spring-damper models to simulate tissue deformation, but they fail to provide detail information on the tissue properties required for the deformation simulation [54, 57, 58]. On the other hand, a sophisticated apparatus was used for data acquisition to

enable virtual ultrasound display of the human thigh as well as force feedback to the user [59]. The human thigh model was represented by a mass-spring system which was characterized in an earlier study conducted by the same author [60]. The two layer model was made up of a mesh of masses and linear springs, and a set of nonlinear springs orthogonal to the surface mesh to model volumetric effects. Realistic haptic force feedback was enabled by incorporating a buffer model between the physical model and haptic device. The buffer model was defined by a set of parameters and was continuously adapted in order to fit the values provided by the physical model. This computationally simple model can estimate the interaction force according to the physical model at haptic update rates.

Although the mass-spring model can provide a fast computation and easy implementation, they are not appropriate for the modeling of complex soft tissue deformation in surgery. Primarily, most mass-spring systems are not convergent [61]. As the mesh is refined, the simulation does not converge on the true solution. Instead, the behavior of the model is dependent on the mesh resolution and topology. In practice, spring constants are often chosen arbitrarily, and one can present little quantitatively about the material being modeled. In addition, there is often coupling between the various spring types. For medical applications, as well as virtual garment simulation in the textile industry, greater accuracy is required.

In order to overcome the accuracy problem in modeling of nonlinear biological soft tissues, many researchers have explored new approaches to implement the mass-spring methods. Basafa [62], in his study on realistic and efficient simulation of liver surgery, proposed an extension of the mass-spring modeling approach for more realistic force formation behavior while maintaining the capability of real-time response. Schwartz [63] introduced an extension of the linear elastic tensor–mass method for fast computation of nonlinear viscoelastic mechanical forces and deformations for the simulation of biological soft tissues with the aim of developing a simulation tool for the planning of cryogenic surgical treatment of liver cancer. The Voigt model was initially considered to approximate the properties of liver tissues. However, it

was later discovered, from experiments, that a linear model is not suitable for modeling this application under various needle penetration loads [63].

Mass-spring models may be combined with other models to achieve a balance in computational efficiency and modeling accuracy. A combined mass spring and tensional integrity method is proposed and applied to simulate the diaphragm motion [64]. A hybrid model which may allow real time deformations and cuttings of anatomical structures was proposed [65]. The quasi-static pre-compute elastic FE model introduced by the authors was computationally efficient but did not allow topology change. Meanwhile, the mass-spring model is well suited for the simulation of tearing and cutting, but a limited number of elements are allowed for real-time simulation. So the authors combined the above models in order to optimize the trade-off between computation time and visual realism of the simulation. Similar study which combined mass-spring models and Boundary Element Method (BEM) was also proposed recently [66]. In this study, a BEM model is used to compute the global deformation while a mass-spring model is employed to interactively model the dynamic behaviours of organs. The hybrid model is suitable for interactive surgical training applications, and provides visually accurate results in simulating the deformation of biological soft tissues with experimental inputs.

Problems still exist in relating mass-spring parameters with real material parameters. The parameters of mass-spring models are typically determined in an ad hoc fashion through trial-and-error which is not directly based on continuum mechanics of deformable objects [67]. Algorithms have been proposed to find alternative ways in determining the model parameters, in which the parameters are determined using a finite element model as a reference model by minimizing the error the stiffness matrices of the finite element and mass-spring models through an optimization algorithm.

2.2.2 Continuum mechanics based computational methods

The computational methods which are based on continuum mechanics are discussed in this section. The most computationally demanding soft tissue

modeling methods are that relying on the equations of continuum mechanics. These equations are regarded as the most accurate mathematical description available for modeling the nonlinear mechanical behavior of soft biological tissue.

Nonlinear elasticity is an important attribute of soft tissue mechanical properties, which is used to modeling the tool-tissue interaction when strains are larger than 2%. The nonlinear stress-strain behavior of biological tissue is usually described by hyperelasticity models [68]. The hyperelastic material is characterized by assuming that the material behavior can be described by means of a strain energy density function--$W(\boldsymbol{F})$, from which the stress-strain relationships can be derived. These materials can generally be considered to be isotropic, incompressible and strain rate independent. The stress in the material resulted from deformation can be obtained from

$$P = \frac{\partial W(F)}{\partial F}, \tag{2.2.2}$$

where P presents the first Piola-Kirchhoff stress tensor and F presents the deformation gradient tensor.

Among the strain energy density functions, Ogden and Mooney-Rivlin strain energy density formulations present as an accurate representation of the constitutive laws for the biological tissues[69], which are also employed in our studies.

In the Ogden material model[70], the strain energy density is expressed in terms of the principal stretches λ_j, $j = 1,2,3$ as:

$$W(\lambda_1, \lambda_2, \lambda_3) = \sum_{p=1}^{N} \frac{\mu_p}{\alpha_p} (\lambda_1^{\alpha_p} + \lambda_2^{\alpha_p} + \lambda_3^{\alpha_p} - 3), \tag{2.2.3}$$

where N, μ_p and α_p are material constants. Under the assumption of incompressibility ($J = \lambda_1\lambda_2\lambda_3 = 1$), Eq.(2.2.3) can be rewritten as

$$W(\lambda_1,\lambda_2)=\sum_{p=1}^{N}\frac{\mu_p}{\alpha_p}(\lambda_1^{\alpha_p}+\lambda_2^{\alpha_p}+\lambda_1^{-\alpha_p}\lambda_2^{-\alpha_p}-3)\,. \tag{2.2.4}$$

The Mooney-Rivlin material was originally developed for rubber, but it has often been applied to model (incompressible) biological tissue. The Mooney-Rivlin material takes the form of a linear combination of principle invariants I_i:

$$W=C_1(\overline{I}_1-3)+C_2(\overline{I}_2-3)\,, \tag{2.2.5}$$

where C_1 and C_2 are empirically determined material constants, and I_1 and I_2 are the first and the second invariant of the unimodular component of the left Cauchy–Green deformation tensor:

$$\overline{I}_1=J^{-2/3}I_1, \tag{2.2.6}$$

$$\overline{I}_2=J^{-4/3}I_2\,, \tag{2.2.7}$$

where $I_1=\lambda_1^2+\lambda_2^2+\lambda_3^2;\ I_2=\lambda_1^2\lambda_2^2+\lambda_2^2\lambda_3^2+\lambda_3^2\lambda_1^2$ and $J=\det(F)$.

Finite Element (FE) methods are widely used numerical techniques for finding approximate solutions to Partial Differential Equations (PDE). Most physical phenomena can be modeled using differential and integral equations. Finite element models are well suited to compute accurate and complex deformation of soft tissue. In order to achieve realistic simulation of biological soft tissue deformation, computations can be extremely time-consuming under conditions of large deformation and moving boundaries. However, modern computers have revolutionized the field of numerical methods and have facilitated the processing of large problems that once lay beyond our reach [36]. The FE methods are utilized in the tool-tissue interaction modeling work in the degradation process simulation of bioresorbable materials in Chapter 6.

The FE method only produces a linear system of algebraic equations if applied to a linear PDE. Bro-Nielsen and Cotin [71] use linearized finite elements for surgery simulation. They achieve significant speedup by simulating only the

visible surface nodes (condensation), similar to the BEM. Linear FE model was also utilized in simulation of laparoscopic cholecystectomy surgery [72].

The study of nonlinear solid mechanics, specifically hyperelasticity, provides a feasible approach to analyze the large deformation problems. Guillaume Picinbono [73] proposed a deformable model which is based on nonlinear elasticity, anisotropic behavior, and the finite element method. It solves the problem of rotational invariance and considers the anisotropic behavior and the incompressibility properties of biological tissues. Furthermore, they optimized the computation time of this model by computing the nonlinear part of the force only for the parts of the mesh which undergo large displacements. The simulation results, as shown in Figure.2.1 and Figure.2.2, indicate that the nonlinear based methods are able to deal with the large deformation problem.

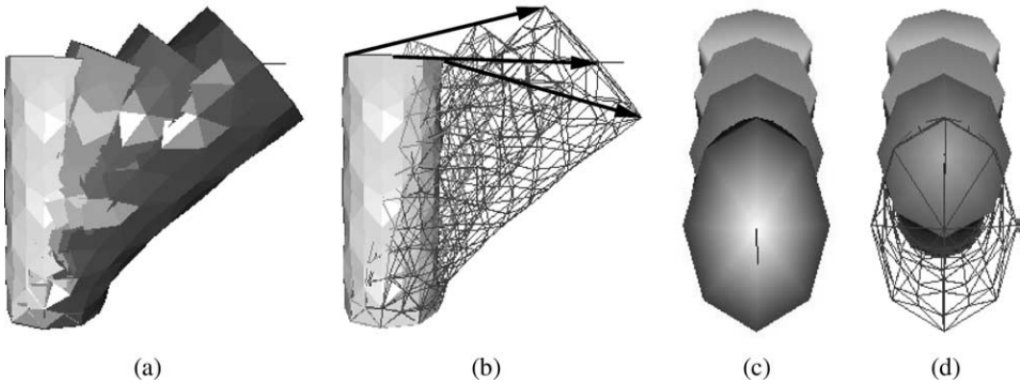

Figure.2.1 Deformations of linear classic cylinder. (a) and (b) side view; (c) and (d) top view

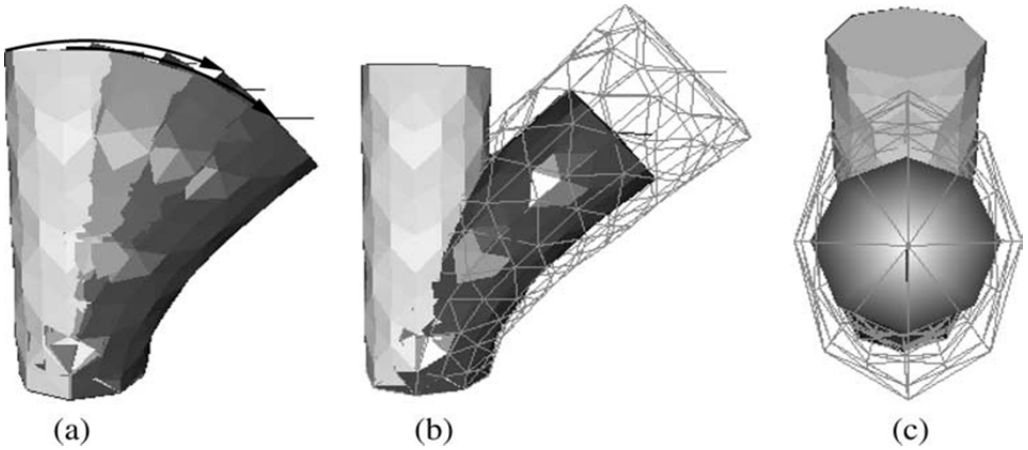

Figure.2.2 Deformations of nonlinear cylinder. (a) and (b) side view; (c) top view. Comparisons between linear (wireframe) and nonlinear model (solid rendering) are indicated in (b) and (c) [73]

In order to develop more accurate constitutive models, researchers have used experimental data and elaborate setups to populate the coefficients of the strain energy function. Carter [74] carried out several indentation tests on sheep and pig liver, pig spleen ex vivo, and human liver in vivo for the development of a laparoscopic surgical simulator. An exponential equation that relates the stress to the stretch ratio, developed by Fung [68], was used for characterization of the material parameters. Davies [75] performed large and small probe indentation experiments on un-perfused and perfused pig spleen for potential use in surgical simulators. An exponential stress-strain law was employed to study the mechanical properties of the soft tissue as an incompressible, homogeneous, isotropic nonlinear elastic material. The goal of their study was to underscore the fact that experimental studies are required to build realistic tool-tissue interaction models, and the hyperelastic model of exponential form is suitable for modeling pig spleen. In Hu's work [76], the authors compared their simulation results through FE analysis with results obtained from others hyperelastic models, while Chui [77] investigated the strain energy functions that were combinations of polynomial, exponential, and logarithmic forms. Chui [77] concluded that both the Mooney-Rivlin model [78, 79] with nine material constants and the combined strain energy of polynomial and logarithmic form with three material constants were able to fit the experimental data on liver tissue. The lowest root mean square error of 29.78 ± 17.67 Pa was observed between analytical and experimental results for the tension experiments where the maximum stresses were in the order of 3.5 kPa.

Arterial tissues have also been studied by Holzapfel using hyperelastic anisotropic models[80]. The authors proposed an approach in which arterial walls are approximated as two-layer thick-walled tubes, with each layer modeled as a highly deformable fiber-reinforced composite. This leads to a fully three-dimensional anisotropic material description of the artery incorporating histological information. This approach provides insight into the nature of the stress distribution across the arterial wall, and therefore offers the potential for a detailed study of the mechanical functionality of arteries. The mechanical behavior of large deformations was characterized with FE

modeling via hyperelastic and viscoelastic models[81]. Considering the influence of the boundary conditions, the material model was designed and integrated into an inverse FEM optimization algorithm to estimate the material parameters of porcine liver tissue. They attempted to minimize the discrepancy between the experiment and simulation results by changing the tissue models. Despite the additional simulation, it was still difficult to obtain the expected results. Therefore, further improvement is needed for the simulation with consideration of the material nonlinearity, the anatomical structure (anisotropic, non-homogeneous, etc.) of the organs, and the boundary conditions of the experiments.

Despite their accuracy and robustness, finite element techniques still suffer from certain drawbacks in real time simulation. First, the boundary condition decides whether the simulation is accurate, the complexity of human body always becomes a constraint for accurate simulation. Furthermore, large deformations and nonlinear response of tissues cause the finite elements to behave badly or totally fail unless re-meshing is performed. Finally, change of topology, e.g., during the simulation of surgical cutting necessitates re-meshing which destroys any pre-computed data, increases the number of computations on the fly and seriously degrades real time performance. For mass-spring systems, although it is simple and computational inexpensive, it is difficult to determine the parameters of hundreds of thousands of springs, dampers and masses to represent the global behavior of the tissue especially for the nonlinear or viscoelastic behavior. Moreover, it is difficult to enforce global properties like incompressibility when using such models and the problem is exacerbated when one tries to use a relatively few particles to reduce computational time.

2.3 Variational modeling methods

In solving modeling problems arising from mathematical physics and biomechanical engineering, it is often possible to replace the problem of integrating a differential equation with an equivalent problem of seeking a function that gives a minimum value of some integral. Problems of this type are called variational problems. The methods that allow us to reduce the

problem of integrating a differential equation to the equivalent variational problem are usually called variational methods [82].

Based on the assumption of incompressible feature such as that of Ogden's model [27], variational methods can be utilized to model the deformation of tissue by solving energy minimization problem in finite regime. The classical variational principles are formulated for nonlinear problems by considering incremental deformation of a continuum. G.Horrigmoe [83] first proposed the major variational principles of solid mechanics for nonlinear problems. It demonstrated how the classical incremental variational principles can be modified by relaxing the continuity requirements between adjoining elements. The work demonstrates how the variational principles can be adopted to finite element method and how associated finite element models arisen.

Many hydrated biological tissues, including artery, cartilage and skin, will experience large deformation over a relatively short period of time, especially under laboratory test conditions where normal physical restraints are absent. Accurate predictions of material behavior thus require a theoretical model capable of representing both geometric and material nonlinearities. As a precursor, the continuum mixture theory for finite deformation, quasistatic poroelasticity with constituent incompressibility is reformulated within the variational framework in Levenston's work [84].

After that, Fancello [85] presented a computationally inexpensive general framework for constitutive viscoelastic models. Since the constitutive updates obey a minimum principle with each load increment, the approach can be qualified as variational based. Due to its variational characteristic, it provides appropriate mathematical structure for further applications like, for example, error estimation. Moreover, it has the appealing characteristic that different materials can be modelled by means of the definition of constitutive potentials depending on eigenvalues of strains and strain-rate.

Cotin developed an interactively deformable model for surgery simulation by using the concept of active surfaces [86]. By solving an energy minimizing problem using the variational approach, the elasticity and flexibility can be

mathematically represented. The spring model was implemented to model the deformation as totally elastic. However, the biomechanical property of the soft tissue was not represented in the model. A general variational approach for finite viscoelastic models was presented in Fancello's work [85], numerical simulations based on Kelvin-Maxwell models in the work illustrate the advantages of the particular variational approach in dealing with nonlinear problem.

Variational based modeling methods have many applications in soft tissue deformation modeling. Realistic and efficient modeling and animation of skin for both humans and animals requires attention on how the skin stretches and moves, as well as how it forms wrinkles and folds. A combined kinematic and variational approach is provided to model the wrinkle formation as an integral part of skin deformation [87], which is especially useful in generating wrinkles on skin meshes where the resolution of the mesh is too large for wrinkle to manifest them clearly. They employed a formulation to model skin elasticity that minimizes an energy functional containing stretching and bending energy and skin tension terms inherent in the anchoring of skin to the underlying layers.

In order to simulate the impact and wave induced damage in biological tissues. Tamer El Sayed [88] presented a fully variational constitutive model of isotropic soft biological tissues which includes Ogden-type hyperelasticity, finite viscosity, deviatoric and volumetric plasticity, rate and microinertia effects. Fitting results of Franceschini's experimental works [89] is shown in Figure 2.3. The model can be used to predict a wide range of experimentally observed behavior, including hysteresis, cyclic softening, rate effects, and plastic deformation.

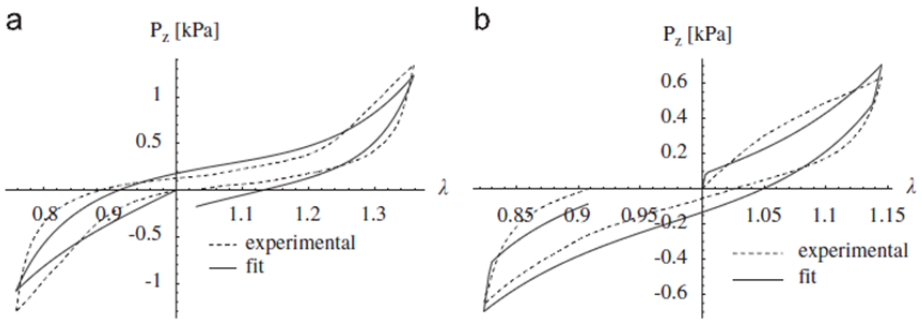

Figure.2.3 Model fits of Franceschini et al[89]. one-cycle compression-tension (a) and tension-compression (b) tests on specimens of white matter. The X axis denotes the stretch ratio for the experimental data while the Y axis indicates the nominal stress

In addition, anisotropic hyperelastic properties was also studied by Schroder [90]. They focused on materially stable anisotropic energy for soft tissue in the sense of the Legendre-Hadamard (L-H) condition. Polyconvex stored energy functions were constructed in order to satisfy the L-H condition. The polyconvex stored energy was adapted to two reference models reflecting characteristic stress-strain relations of soft tissues. The results demonstrated that the polyconvex model is able to represent the same essential physically observed material behavior as the reference models. However, the standard reference formulations for anisotropic hyperelasticity have problems on material stability.

Another related research is done by Massoptier and Sergio on segmenting three dimensional liver surfaces automatically from images obtained via CT or MR by using the graph-cut technique [91] and the Gradient Vector Flow (GVF) snake [92]. The results of the two techniques are compared for best contribution in Figure 2.4. Active contour in GVF is used to obtain an accurate surface that approximates the real liver closely. Its application in the segmentation of CT images resulted in good processing time and quality. However, this technique is prone to assuming a mistaken boundary for related particles located inside but close to the liver surface. They could be considered to be outside the region of interest [91]. This error is undesired and it is addressed by the graph cut technique for more accurate automatic image segmentation. This method investigates the mean and standard deviation of liver samples in determining the error margin and hence, the accurate boundary of the liver region based on the voxels, edges and vertices of the

liver from the CT images. Three dimensional segmentations were evaluated and the error in implementing the graph-cut technique was lower than that applying the GVF technique.

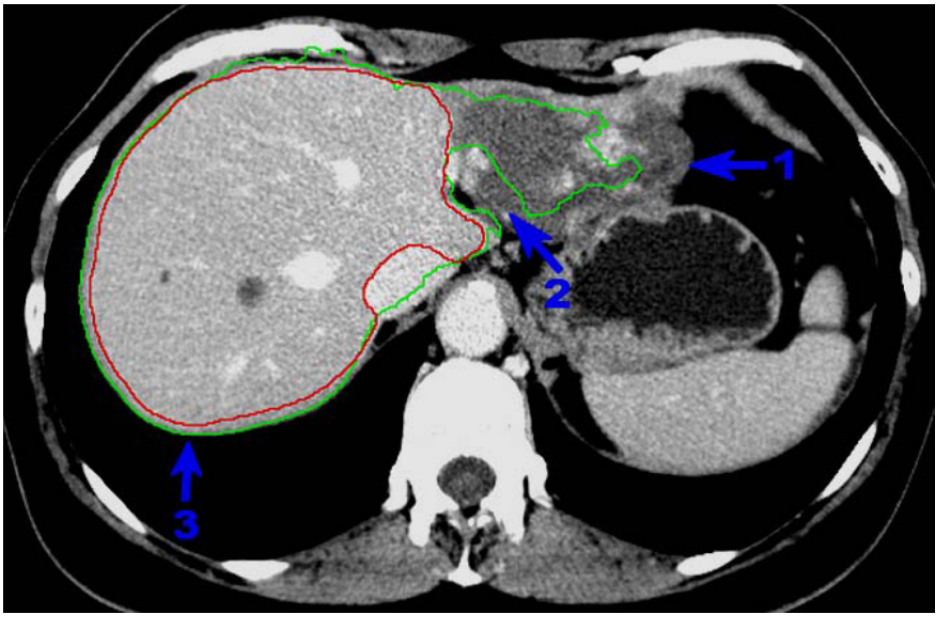

Figure.2.4 Visual comparisons between the graph-cut method (outer line) and the active contour segmentation (inner line)

Chapter 3 Mathematical Modeling of Soft Tissue Deformation

This chapter introduces the mathematical models that we have been using to model soft tissue deformation. Using conventional notation, let $F = \nabla x$ denotes the gradient of deformation at an arbitrary point of the material, and let $C = F^T F$ denotes the right Cauchy-Green strain tensor. We assume that the biological soft tissue can be represented as a hyperelastic material. The main assumption in hyperelasticity is the existence of a potential function W which only depends on the value of strains and the Piola-Kirchhoff stress tensor,

$$P = \partial W(F) / \partial F \,. \tag{3.1}$$

Assuming the satisfaction of compatibility and constitutive equations, the equilibrium problem may be defined by the minimization of the potential energy

$$\min_{x \in K} H(x) = \min_{x \in K} (\int_{\Omega_0} W(F(x)) d\Omega_0 - [\int_{\Omega_0} b_0 \bullet x d\Omega_0 + \int_{\Gamma_0} f_0 \bullet x d\Gamma_0]) \,, \tag{3.2}$$

where K is the set of admissible deformations.

Meanwhile, the stress of an inelastic path dependent dissipative phenomenon cannot be obtained just form the value of final strains. In order to represent the stress of an inelastic path dependent dissipative phenomenon, history of the deformation process is presented incrementally using dissipative variables[21, 93]. They can be modelled by pseudo potentials within the interval of a load increment as

$$P_{n+1} = \partial W(F_{n+1}; \varepsilon_n) / \partial F_{n+1} \,, \tag{3.3}$$

where ε denotes a set of external and internal variables:

$$\varepsilon = \{F, F^i, Q\} \,, \tag{3.4}$$

$$F = F^e F^i = F^e F^v = F^e F^p \,, \tag{3.5}$$

$$F^e = F F^{i-1} \,. \tag{3.6}$$

The tensors F^e and F^i ($i \in \{v, p...\}$) denote the respective elastic and inelastic parts of the gradient of deformations, *v* and *p* denote the viscous and plastic parts of the deformation, respectively. Q contains all the remaining internal variables. The sub-indices *n* and *n+1* indicate the beginning and ending of the load increment and it is supposed that all quantities at time *n* are known.

The potential $W(F_{n+1};\varepsilon_n)$ of inelastic problems is derived as following:

$$W(F_{n+1};\varepsilon_n) = \min_{\substack{F^i_{n+1} \\ Q_{n+1}}} \{W(\varepsilon_{n+1}) - W(\varepsilon_n) + \Delta t\psi(\tilde{F}^i, \tilde{Q}; \varepsilon_n)\}, \tag{3.7}$$

where $\tilde{F}(F_{n+1},\varepsilon_n)$, $\tilde{F}^i(F^i_{n+1},\varepsilon_n)$ and $\tilde{Q}(Q_{n+1},\varepsilon_n)$ are suitable incremental approximations of the rate variables $\dot{F}$, $\dot{F}^i$,and $\dot{Q}$ respectively. The potentials *W*, and ψ may represent different expressions depending on the particular model needed, such as viscoelastic and hyperelastic models. Δt is the time increment. The minimization problem with respect to the internal variables F^i_{n+1} and Q_{n+1} provides an evolution path of these variables within the time step and eliminates them from the potential *W*, and hence it is dependent only on the gradient of deformation F_{n+1} .

Within this variational framework, the variational problem in hyperelasticity material can be solved by customized approaches with specific problems.

For Fung type material, we will illustrate the solution based on GA. It is assumed that the strain energy admit decomposition into deviatoric and volumetric parts [88, 94]. The strain-energy decompositions are

$$W = W_{dev} + W_{vol}, \tag{3.8}$$

$$W_{dev} = \frac{c}{2}(e^Q - 1), \tag{3.9}$$

$$Q = a_1E_\theta^2 + a_2E_z^2 + a_3E_r^2 + 2(a_4E_\theta E_z + a_5E_zE_r + a_6E_\theta E_r), \tag{3.10}$$

$$W_{vol} = f(J), \tag{3.11}$$

where E_j denotes the Green strain tensor components, c expresses the units of stress (force/area), and a_1,a_2,a_3,a_4,a_5 and a_6 are dimensionless constants r, θ, z, denotes the radial, circumferential, and axial directions in polar coordinates.; $J = \det(F)$ is the determinant of deformation gradient.

Substitute Eq. (3.8-3.11) into Eq. (3.1), the engineering stress of the material can be obtained. Hence, the relationship between engineering stress and engineering strain can also be found. The genetic algorithm is employed for parameters identification. A collection of n experimental results is available for model parameter identification, through a data set of the form

$$\{[x_i, y_i]_{i=1,\ldots,N_p}\}, \tag{3.12}$$

where x_i is the experimental strain measure while y_i is the corresponding recordings of stress measure, N_p is the number of data points collected from the experiment. The best-fit values of selected parameters

$$p = \{\{p_m\}_{m=1,\ldots,P}\}, \tag{3.13}$$

are sought, P is the total number of selected parameters, under simple bounds of the form

$$p \in D = [p_1^{lb}, p_1^{ub}] \times \cdots \times [p_P^{lb}, p_P^{ub}]. \tag{3.14}$$

With the parameter set p_i, numerical simulations of the experiments can be employed to get a set of predictions

$$\{[x_i, y_i(p)]_{i=1,\ldots,N_p}\}. \tag{3.15}$$

The fitness function is given as following:

$$f(p) = \sum_{i}^{N} (y_i(p) - y_i)^2 . \tag{3.16}$$

This leads to the multivariate minimization problem

$$\min_{p \in D} f(p), \tag{3.17}$$

which is expected to be non-convex and affected by multiple local optima[95]. This solution is applied in Chapter 4 and 5 to determine the material parameters of different soft tissue.

Incremental FE based methods are employed in solving the variational problem in simulation of the degradation of biodegradable materials. The total energy of the system W is minimized if the differential with deformation is zero.

The state of minimal energy corresponds to

$$\frac{\partial W}{\partial F} = 0 . \tag{3.18}$$

Apply Taylor expansion of W around an initial guess $F(0)= (x(0), y(0)) = [(x_1(0), y_1(0)), (x_2(0), y_2(0)),(x_3(0),y_3(0))\dots(x_N(0),y_N(0))]^T$ of the equilibrium state gives

$$\begin{aligned} W \approx W(F(0)) + \left.\frac{\partial W}{\partial F}\right|_{F=F(0)} \cdot (F - F(0)) \\ + \frac{1}{2}(F - F(0))^T \cdot \left.\frac{\partial^2 W}{\partial F \partial F}\right|_{F=F(0)} \cdot (F - F(0)) \end{aligned} . \tag{3.19}$$

Substitute Eq. (3.18) into Eq. (3.17) yields the following governing equation of the element displacement u,

$$K \cdot u = P , \tag{3.20}$$

where

$$K = \left.\frac{\partial^2 W}{\partial F \partial F}\right|_{F=F(0)} , \tag{3.21}$$

$$P = -\left.\frac{\partial W}{\partial F}\right|_{F=F(0)} . \tag{3.22}$$

K denotes the stiffness and P denotes the non-equilibrium force of the system element. For the whole system, Eq. (3.19) must be solved iteratively until P reaches zero, $P=0$, which indicates that there is no non-equilibrium force to drive the element to move.

For minimization problems, FE model will converge and achieve stability if the total energy W decreases during every iteration step. Since the non-equilibrium force $P = -\left.\frac{\partial W}{\partial F}\right|_{F=F_{new}(0)}$ represents the steepest descent direction of total energy W, the stability and convergence are ensured if

$$P \cdot u > 0 , \tag{3.23}$$

where u is the displacement increment. A sufficient condition for Eq. (3.23) is that the stiffness matrix K is positively definite.

Each element will reach its minimum energy after the above iterative steps, which is the stable energy state of the subject. This incremental FE based solution is particularly applied to model the degradation process of bioresorbable materials in Chapter 6.

Chapter 4 Modeling Vascular Tissue Mechanical Properties

Based on the underlying mathematical models described in the previous chapter, this chapter illustrates the application of mathematical models to represent the mechanical properties of human vascular tissue. The uncertainties of human arteries' mechanical characteristics are studied in Section 4.1. We proposed a probabilistic approach to model the uncertainties of human artery tissue properties. The mechanical properties of artery tissue during division in laparoscopic surgery are also investigated in Section 4.2.

4.1 Characterization of human artery tissue

We investigated the biomechanical properties of human artery tissue during elongation tests using a probabilistic approach in this section. Accurate modelling of biomechanical properties of artery tissue is important for developing realistic medical simulation systems which are commonly used in surgical training, planning and treatment, and diagnostic tools for vascular diseases. With the advancements in medical imaging technologies and mapping tools, model personalization has generated a lot of research interest [96, 97]. Model personalization which is defined as the adaptation of a generic model to a specific patient model based on available clinical data enables the application of computational models in clinical practice by validating the models with patient data. This section characterizes the patient specific material parameters and validates the models using experimental data of human iliac vessels.

Nonlinear mechanical property is an important attribute of the artery tissue which can contribute to modelling accuracy, and hence needs to be considered for realistic deformation simulation and haptic rendering in surgical simulation of the arterial wall. Experimental procedures such as inflation tests [7], biaxial tests[8], as well as tension and indentation tests[9, 10] have been performed to study the mechanical properties of arteries tissue. The experiments revealed

that arteries are elastic, highly nonlinear and anisotropic under finite strains, and could be adequately modelled within the framework of hyperelasticity.

Many constitutive models have been proposed for mathematical description of the mechanical behavior of artery tissue [69, 98, 99]. Strain energy based models are able to provide comprehensive understanding of the inter-relationship between stress and strain. In [11], the combined logarithmic and polynomial model was reported to perform better than the combined exponential and polynomial model [99] in modelling the stress-strain relationship of liver tissue. In [12], the combined logarithmic and polynomial model has been utilized for realistic modelling of porcine artery tissue. Structural strain energy function is proposed to study the arterial tissue [100]. The proposed function includes the wavy nature of the collagen and the fraction of both elastin and collagen contained in the media, which can be determined by histology. The waviness of the collagen is assumed to be distributed log-logistically. The novel strain energy function is found to behave similarly to that of Holzapfel et al.[69], both succeed in describing the typical S-shaped pressure-radius curves with comparable quality of fit.

Tension tests have been performed on human artery tissue to study its nonlinear biomechanical properties. Due to varying micro-structural composition of tissue specimens and inherent noises from experimental instruments, the measured stress-strain data often comprise of a number of stress-strain curves with large deviations [101]. Material parameters of soft tissue model are usually characterized using the mean stress-strain curve and ignoring the stress-strain curve deviations. However, it is important to incorporate the inherent stiffness variations for realistic medical simulation. These inherent stiffness variations of artery tissue may be modeled using probabilistic uncertainty analysis. The applicability of probabilistic uncertainty analysis has been demonstrated in evaluating structural reliability [102, 103], and knee ligamentous constraint analysis [104]. A probabilistic method was proposed to model the mechanical properties of liver tissues in [105]. To our best knowledge, no report has been published on probabilistic analysis of human artery for characterization and deformation simulation in the literature.

In this study, we introduce the probabilistic approach to model the inhomogeneity, specifically the stiffness variations of human artery tissue. Cyclic tension tests in longitudinal and circumferential directions were performed on human arteries. The arteries are highly inhomogeneous with large variances in stress-strain curves. We assume that the experimental stress values at a certain strain are distributed according to normal distribution. A combined logarithmic and polynomial constitutive equation [12] is employed to model the average stress-strain relationship of human artery tissue in circumferential and longitudinal directions. The material parameters are expressed as a statistical function with normal distribution. The mean values of the material parameters are identified using GA while the standard deviation of the material parameters are determined using direct calculation method (DC) and inverse mean-value first-order second-moment (IMVFOSM) method, respectively. The probabilistic approach is then verified using Monte-Carlo (MC) method and demonstrates good correspondence with cumulative distribution function (CDF) between simulated and experimental stress-strain data. Validation of the material parameters are carried out with experimental human artery data.

Section 4.1.1 describes the experiments carried out on human arterial tissue. In Section 4.1.2, the probabilistic approach is introduced and material parameters are determined from the scattered experimental stress-strain data. Section 4.1.3 presents the MC simulations which are used to verify the correctness of the derivation process of the material parameters. In Section 4.1.4, the feasibility of calculated material parameters is evaluated using experimental data. Finally, Section 4.1.5 presents a brief summary and critique of the study including a discussion on the implication of our findings towards future study.

4.1.1 Elongation tests on artery samples

There are three types of arteries: elastic, mixed and muscular. Abdominal aorta, femoral artery and popliteal artery are examples of elastic, mixed and muscular arteries respectively [106]. Uniaxial elongation tests were performed on 20 samples of human femoral arteries in circumferential and longitudinal directions. The experiments were carried out with a mechanical property

measurement system which was designed to meet the requirements of automated environment control, testing, and data collection for biological tissue [12]. The measurement system consists of five main sections: fixture, execution, circulation, measurement, and computing section, which is shown in Figure 4.1.1. Stepper motor (CTP21 DANAHER) driven translational stages were employed to carry out elongation. A large distance laser sensor (optoNCDT 1401-200, Micro-epsilon) was mounted on the translation stage to form a close-loop control for positioning. Load cells (LCM UF series) were employed to measure force imposed on specimen. Human femoral arteries were obtained from human donors and stored in an ice box with Histidine Tryptophan Ketoglutarate (HTK) solution before experiment. The arteries were intended for organ transplant, and the donors' identities were protected in according to an approved Institutional Review Board protocol. All arterial specimens were excised from the distal end of the abdominal aorta, with lengths between 40-50 mm and diameters between 6-11 mm. During experiment, the artery specimen was immersed in Krebs Ringer solution at 37℃ throughout the experiment, with pH value maintained at 7.3-7.4 using carbon dioxide.

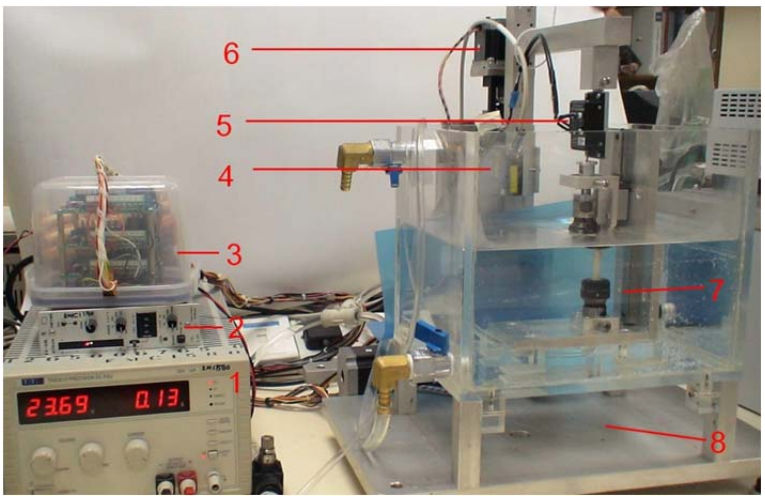

Figure.4.1.1 The mechanical testing system; (1) power source (2) Strain gauge amplified for load cell and pressure transducer(not shown), (3) Stepper motor control, (4) Distance laser sensor, (5) Load cell, (6) translational stage with stepper motor. (7) clamping feature and fixture, (8) base.

Specimens were tested in circumferential and longitudinal directions, respectively. A ring segment was sliced off from one end of each arterial

specimen and tested in circumferential direction. The remaining section of the specimen was used to perform tests in the longitudinal direction. All specimens were preconditioned before data collection over a course of at least five cycles, allowing the specimens to reach a steady state with no further changes occurred on the stress-strain curves [68, 107]. During the experiments, force and displacement data were measured and recorded. Stretch ratio λ was calculated by dividing instantaneous gauge length by its original length while engineering stress T was calculated by dividing the instantaneous load by the original cross-sectional area. Strain ε can be expressed as $\lambda - 1$. The tension tests were performed until the stretch ratio reached 1.55 for both directions at a ramping speed of 2.5 mm/s.

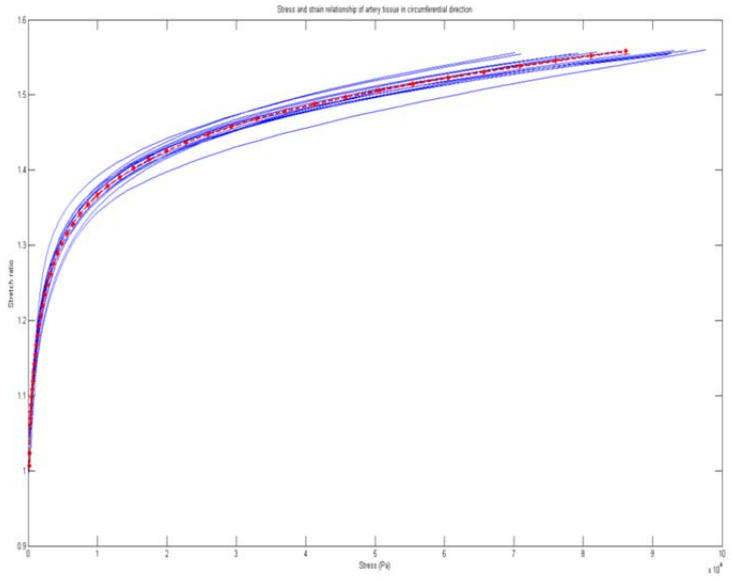

(a)

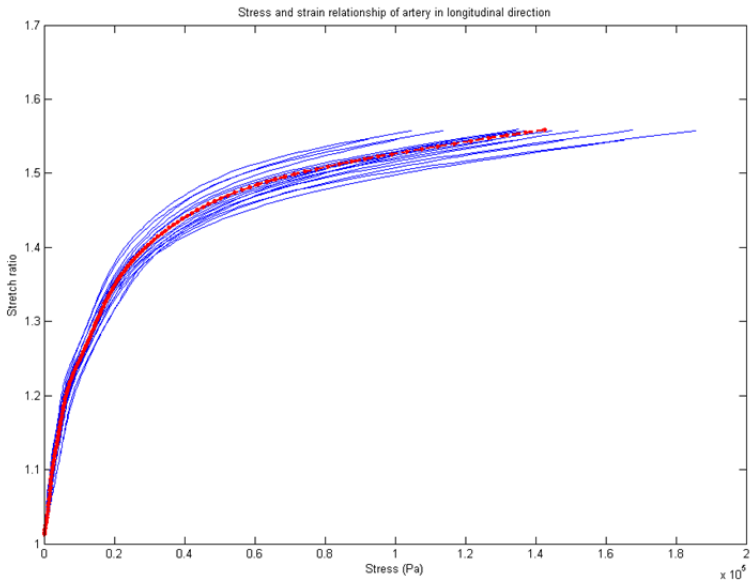

(b)

Figure.4.1.2 Stress and strain distribution of artery tissue. (a) Circumferential; (b) Longitudinal directions. Blue solid line (—) denotes the random selected experimental curves; red short dash line (--) is the mean value curve of the experimental curves

Two sets of scattered stress-stain curves which represent the data in circumferential and longitudinal directions were plotted together with its mean curve in Figure.4.1.2. Each set includes twenty curves. The experimental stress with respect to a specific stretch ratio is assumed to vary according to normal distribution. Mean value and standard deviation of stress is calculated as:

$$\mu_T = \frac{1}{N}\sum_{i=1}^{N} T_i \,, \tag{4.1.1}$$

$$\sigma_{T_i} = \sqrt{\frac{1}{N}\sum_{i=1}^{N}(T_i - \mu_T)^2} \,, \tag{4.1.2}$$

where σ_{T_i} denotes the experimental stress value and N is the number of experimental stress values. Experimental results of minimum, mean and maximum stress-strain curve are also illustrated in Figure.4.1.3. The probability density function (PDF) of the stress values calculated using Eq. 4.1.1 and Eq.4.1.2 at three different strain values are plotted in Figure.4.1.3. The normal distribution assumption is tested through Shapiro-Wilk test [108].

The average probabilities of normality in circumferential and longitudinal directions are 0.7185 and 0.7237, which validate our assumption.

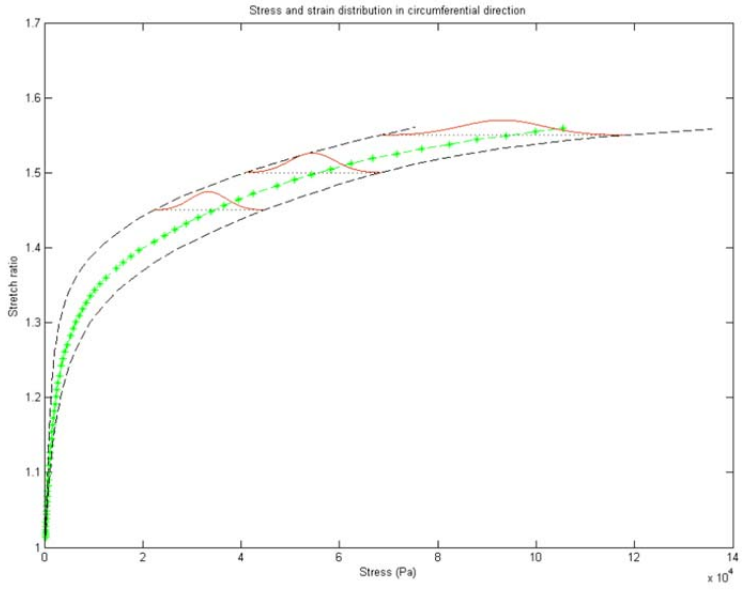

(a)

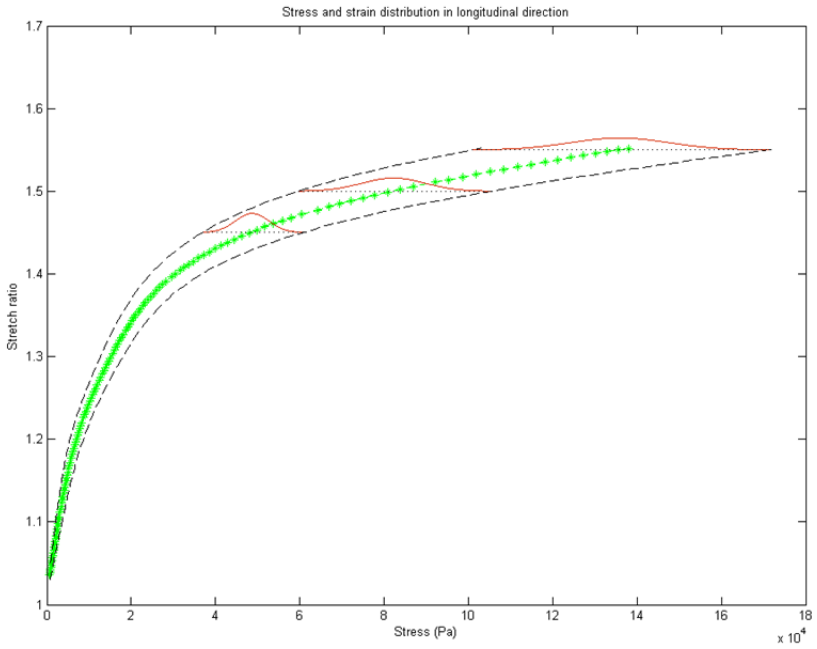

(b)

Figure.4.1.3 Stress and strain relationship of artery tissue. (a) Circumferential direction; (b) Longitudinal direction. Green (-*) mean Black (--) maximum and minimum values of stress. Normal distribution of stress values is illustrated along horizontal bars using red solid line

4.1.2 Probabilistic approach

Probabilistic method is used for material parameter identification of artery tissue. Deformation of artery tissue is considered as a structural problem that can be solved using the probabilistic method.

4.1.2.1 Strain energy function of artery tissue

The artery tissue is represented by a 7-constant combined logarithmic and polynomial energy function[12]. The combined logarithmic and polynomial constitutive equation performs well in modelling highly nonlinear mechanical behaviours: the polynomial component is dominant at low strain while the logarithmic component is dominant at high strain.

$$W = -\frac{C_1}{2}\ln(1-u) + \frac{q}{2}, \tag{4.1.3}$$

where

$$u = \frac{1}{2}C_2(I_1-3)^2 + \frac{1}{2}C_3(I_4-1)^2 + C_4(I_1-3)(I_4-1), \tag{4.1.4}$$

$$q = C_5(I_1-3)^2 + C_6(I_4-1)^2 + 2C_7(I_1-3)(I_4-1). \tag{4.1.5}$$

W denotes the strain energy function, $C_1....C_7$ are the material parameters, I_1, I_2 and I_4 are strain invariants which are functions of stretch ratio λ, $I_1 = \lambda^2 + 2/\lambda$, $I_4 = \lambda^2$.

With the combined logarithmic and polynomial energy function, relationship between engineering stress T and stretch ratio λ is derived as follows:

$$\begin{aligned} T = f(\lambda) = &\left(\frac{2C_1(C_2(\lambda^2+\frac{2}{\lambda}-3)+C_4(\lambda^2-1))}{1-G/2} + 2C_5(\lambda^2+\frac{2}{\lambda}-3) + 2C_7(\lambda^2-1)\right)(\lambda-1/\lambda^2), \\ &+\left(\frac{2C_1(C_3(\lambda^2-1)+C_4(\lambda^2+\frac{2}{\lambda}-3))}{1-G/2} + 2C_6(\lambda^2-1) + 2C_7(\lambda^2+\frac{2}{\lambda}-3)\right)\lambda \end{aligned} \tag{4.1.6}$$

where $$G = C_2(\lambda^2+\frac{2}{\lambda}-3) - C_3(\lambda^2-1)^2 + 2C_4(\lambda^2+\frac{2}{\lambda}-3)(\lambda^2-1). \tag{4.1.7}$$

Material parameters of the mean stress-strain curve can be characterized using the above equation.

4.1.2.2 Identification of material parameters for the mean value

The identification process was carried out using Genetic Algorithm (GA). GA is an effective global search method which is well suited for the minimization of non-convex objective functions.

The mean value curve is available for material parameter identification through a data set of the form

$$\{[x_i, y_i]_{i=1,\ldots,N_p}\}, \tag{4.1.8}$$

where x_i is the experimental strain measure while y_i is the corresponding recordings of stress measure, N_p is the number of data points collected from the experiment.

The best-fit values of selected parameters

$$C_T = \{\{C_N\}_{N=1,\ldots,7}\}, \tag{4.1.9}$$

are sought. With the parameter set C_T, numerical simulations of the experiments can be employed to obtain a set of predictions

$$\{[x_i, y_i(C_T)]_{i=1,\ldots,N_p}\}. \tag{4.1.10}$$

The fitness function is:

$$R(C_T) = \sum_{i}^{N} (y_i(C_T) - y_i)^2 . \tag{4.1.11}$$

This lead to the multivariate minimization problem

$$\min_{C \in D} R(C_T), \tag{4.1.12}$$

which is expected to be non-convex and affected by multiple local optima[95].

Starting with random values assigned to parameters data set C_T as the initial solution population, the algorithm will evaluate their level of fitness in the problem domain and create a new set of approximations based on breeding the better evaluated solutions. By repeating the selection, crossover and mutation procedures of the GA, the evolution of populations of individuals that are better suited to their environment than their parents are obtained. The minimum value of $R(C_T)$ is reached, too. An initial population of nearly 100 individuals was used along with a selection percentage of 0.1 and a crossover percentage of 0.7. The algorithm converges to minima after approximately 100 generations while the number of total evolution generations is set to be 150. The comparison between simulated results and mean experimental values are illustrated as following:

Table.4.1.1 Estimated mean values of material parameters.

Material parameters	C_1	C_2	C_3	C_4	C_5	C_6	C_7	R^2	RMSE
Circumferential	-43.28	1735	-390	-818.4	383500	53230	-135000	0.9911	3216
Longitudinal	0.012	783.3	-107.6	-299.6	615400	92230	-228100	0.9857	3455

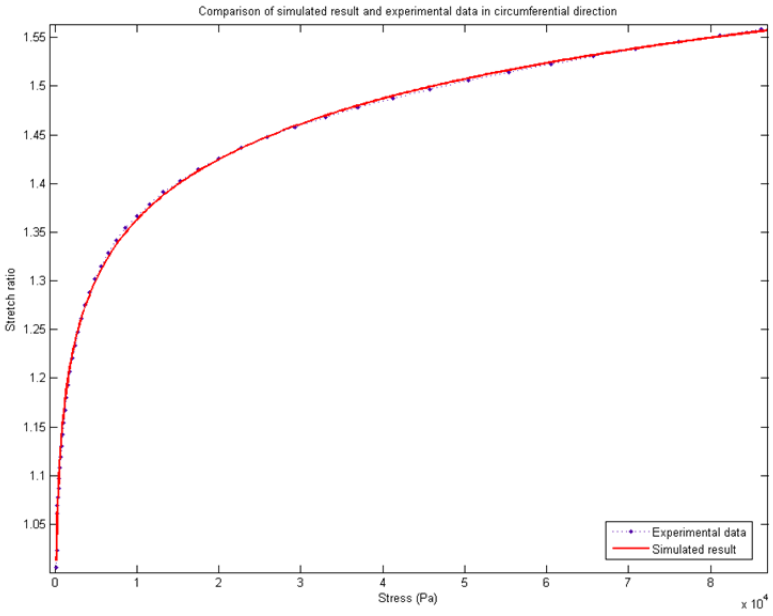

(a)

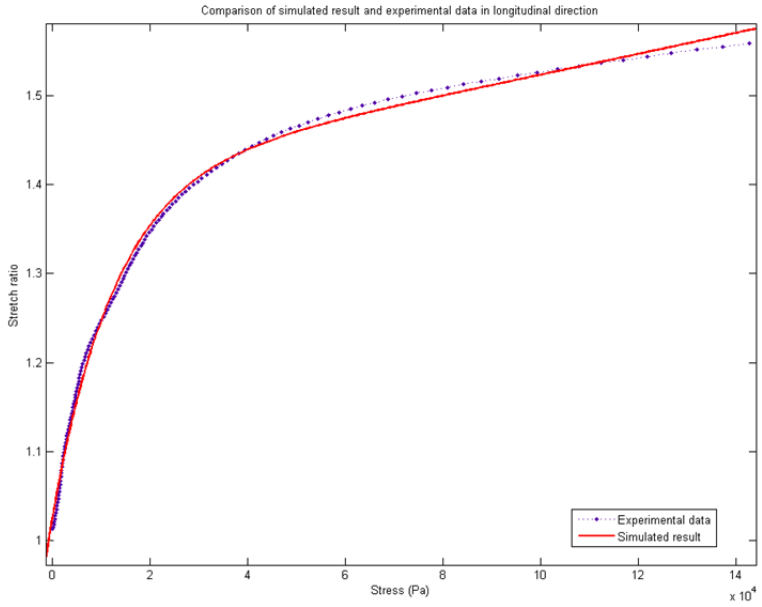

(b)

Figure.4.1.4 Comparison of simulated result and experimental mean value. (a) Circumferential direction; (b) Longitudinal direction

The similar curve patterns in circumferential and longitudinal indicate that C_5, C_6 and C_7 are the dominate parameters. It can be seen from the graphs that the simulated results fit better in circumferential direction than that of longitudinal direction. This may be due to extensive stress in the longitudinal direction. The maximum force limitation of the experiment instrument also causes more noises in the longitudinal direction and this lead to further measurement errors.

4.1.2.3 Standard deviation of material parameters

Two methods were employed to calculate the standard deviation of material parameters. The first method is called direct calculating method (DC method), which first performs the material parameter identification process directly on each set of experimental data and then calculates the standard deviation with the obtained material parameters. The second method is the Inverse mean-value first-order second-moment (IMVFOSM) method.

The IMVFOSM method is derived as follows. By taking Taylor expansion of Eq.4.1.3, the performance function is linearized at the mean values of material parameters:

$$T \cong f(\mu_C) + \sum_{i=1}^{n} \left.\frac{\partial f}{\partial C_i}\right|_{\mu_C} (C_i - \mu_{C_i}), \tag{4.1.13}$$

where $\mu_C = [\mu_{C_1}, \mu_{C_2} \cdots \mu_{C_7}]^T$ is the mean values of $C = [C_1, C_2, \cdots C_7]^T$. The standard deviation and mean value of predicated T can be estimated by

$$\sigma_T \cong \sqrt{\sum_{i=1}^{n} \left(\left.\frac{\partial f}{\partial C_i}\right|_{\mu_C} \sigma_{C_i}\right)^2}, \tag{4.1.14}$$

$$\mu_T \cong f(\mu_C), \tag{4.1.15}$$

where σ_{C_i} denotes the standard deviation of material parameter C_i.

Since the standard deviation σ_T of experimental engineering stress and $\partial f / \partial C_i$ can be calculated, the standard deviation of material parameter σ_{C_i} can be determined by the IMVFOSM method. Numerical values of $\partial f / \partial C_i$ and standard deviation of experimental stress in circumferential and longitudinal directions at different strain stages are shown in Tables.4.1.2 and 4.1.3 respectively.

Table.4.1.2 Numerical values of $\partial f / \partial C_i$ and standard deviation at different strain stages in circumferential direction

Strain	$\frac{\partial f}{\partial C_1}$	$\frac{\partial f}{\partial C_2}$	$\frac{\partial f}{\partial C_3}$	$\frac{\partial f}{\partial C_4}$	$\frac{\partial f}{\partial C_5}$	$\frac{\partial f}{\partial C_6}$	$\frac{\partial f}{\partial C_7}$	σ_T
1.25	8.6597	0.3077	-0.2791	0.6428	0.1983	1.4063	1.0925	386.9
1.30	8.8451	0.3586	-0.2954	0.7972	0.3236	1.7940	1.5714	619.6
1.35	9.3227	0.4337	-0.3470	1.0182	0.4872	2.2208	2.1389	989.2
1.40	10.1522	0.5477	-0.4455	1.3535	0.6915	2.6880	2.7964	1603
1.45	11.4918	0.7318	-0.6259	1.9048	0.9389	3.1973	3.5457	2608
1.50	13.6997	1.0622	-0.9814	2.9218	1.2315	3.7500	4.3889	5019
1.55	17.6804	1.7682	-1.8074	5.1716	1.5710	4.3478	5.3280	8132

Table.4.1.3 Numerical values of $\partial f / \partial C_i$ and standard deviation at different strain stages in longitudinal direction

Strain	$\frac{\partial f}{\partial C_1}$	$\frac{\partial f}{\partial C_2}$	$\frac{\partial f}{\partial C_3}$	$\frac{\partial f}{\partial C_4}$	$\frac{\partial f}{\partial C_5}$	$\frac{\partial f}{\partial C_6}$	$\frac{\partial f}{\partial C_7}$	σ_T
1.25	6.1846	-1.61e-04	4.93e-05	-3.81e-04	0.1983	1.4063	1.0925	904.4
1.30	6.1370	-1.84e-04	4.67e-05	-4.56e-04	0.3236	1.7940	1.5714	1134
1.35	6.2629	-2.17e-04	5.17e-05	-5.59e-04	0.4872	2.2208	2.1389	1488
1.40	6.5768	-2.66e-04	6.41e-05	-7.08e-04	0.6915	2.6880	2.7964	2383
1.45	7.1408	-3.40e-04	8.74e-05	-9.37e-04	0.9389	3.1973	3.5457	4878
1.50	8.0995	-4.64e-04	1.32e-05	-0.0013	1.2315	3.7500	4.3889	10368
1.55	9.8000	-7.01e-04	2.26e-05	-0.0021	1.5710	4.3478	5.3280	18145

The estimation of standard deviation of material parameter is carried out using the GA in order to find the most representative data set along the stress-strain curve. Tables 4.1.4 and 4.1.5 compare the standard deviation of material parameters using the DC method and IMVFOSM method.

Table.4.1.4 Standard deviation of artery material parameters in circumferential direction

Material parameters	C_1	C_2	C_3	C_4	C_5	C_6	C_7
μ_{C_i} (Pa)	-43.28	1735	-390	-818.4	383500	53230	-135000
DC σ_{C_i} (Pa)	54.1	947.4	199.6	434.4	1877.3	305.7	705.8
IMVFOSM σ_{C_i}	64.9	315.5	682.3	757.4	449.7	133.0	146.3

Table.4.1.5 Standard deviation of artery material parameters in longitudinal direction

Material parameters	C_1	C_2	C_3	C_4	C_5	C_6	C_7
μ_{C_i} (Pa)	-20.38	-184.1	-1.72	53.77	440700	60480	-154300
DC σ_{C_i} (Pa)	269.0	745.1	72.2	235.1	303.8	816.6	1442.1
IMVFOSM σ_{C_i} (Pa)	105.1	637.6	170.5	241.6	184.7	701.3	909.0

From the tables, it can be concluded that under the same conditions, IMVFOSM method yields a smaller standard deviation of material parameters σ_{C_i} than that of the direct calculating method.

4.1.3 Verification using Monte Carlo Simulation

In order to verify the accuracy of the probabilistic material parameters estimation method, Monte Carlo (MC) method is used. The MC methods is a sampling method [109-113] often used in computer simulations of physical and mathematical systems when it is infeasible to compute an exact result with a deterministic algorithm [114]. Eq.4.1.6 is performed for 10000 times with the parameters displayed in Table 4.1.4 and 4.1.5 using MATLAB.

Stress CDFs calculated from DC and IMVFOSM methods at strain values of 1.25, 1.30, 1.35, 1.40, 1.45, 1.50 and 1.55 are plotted in Figure.4.1.5. The MC simulation is able to provide smooth CDF curves in both circumferential and longitudinal directions. The results also reveal that simulated stress CDFs of both DC method and IMVFOSM method can correspond well with that of the experimental stress CDFs. Nevertheless, material parameters calculated using IMVFOSM method has performed better than that of DC method with a closer match.

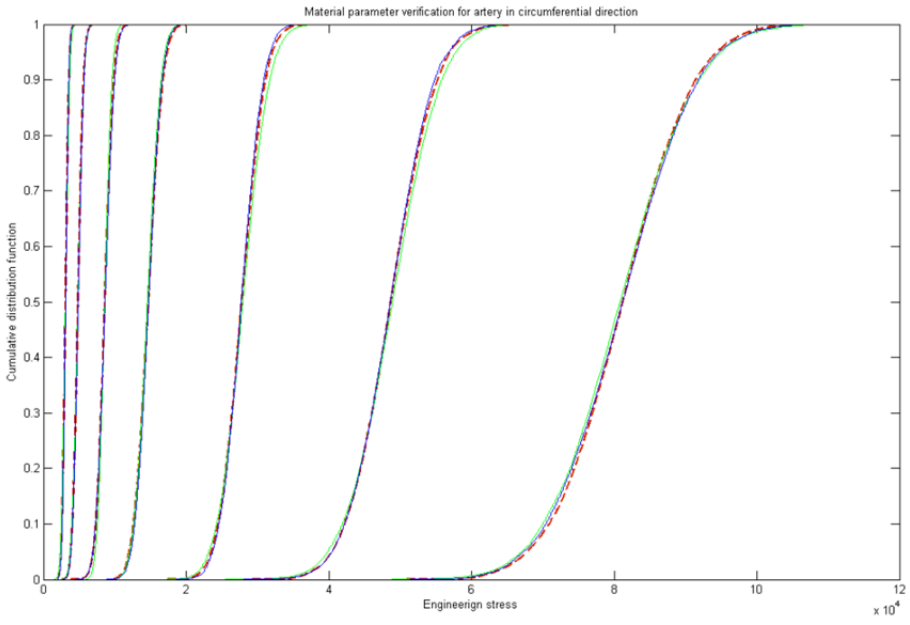

(a)

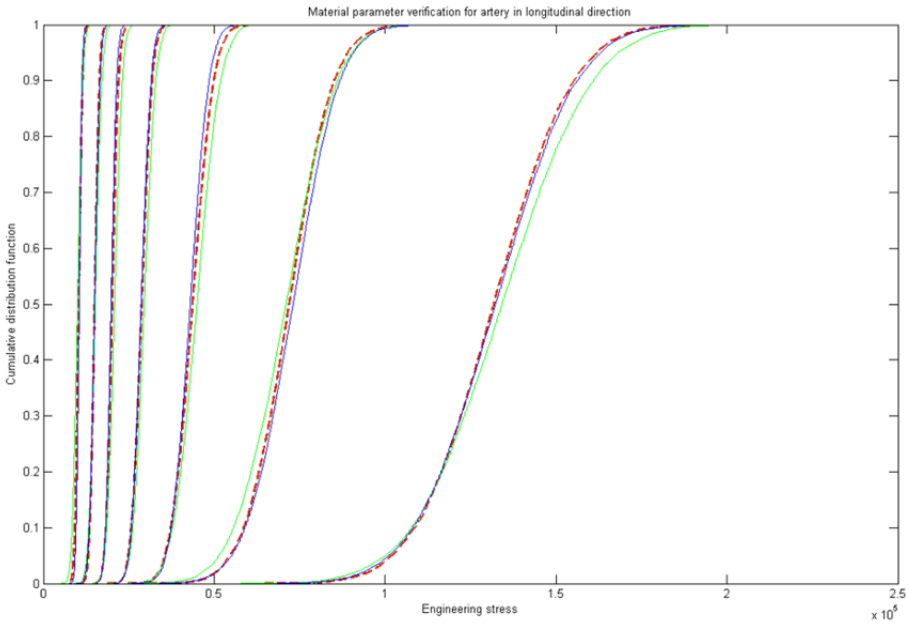

(b)

Figure.4.1.5 CDFs of Engineering stress for artery tissue at seven strain values of 1.25, 1.30, 1.35, 1.40, 1.45, 1.50 and 1.55 from left to right. Red dash line is the experimental CDFs; green heavy line is the CDFs from 10000 evaluations with direct calculated material parameters; blue thin line is the CDFs from 10000 evaluations with material parameters calculated from IMVFOSM method. (a) Circumferential direction; (b) Longitudinal direction

4.1.4 Validation of the proposed approach

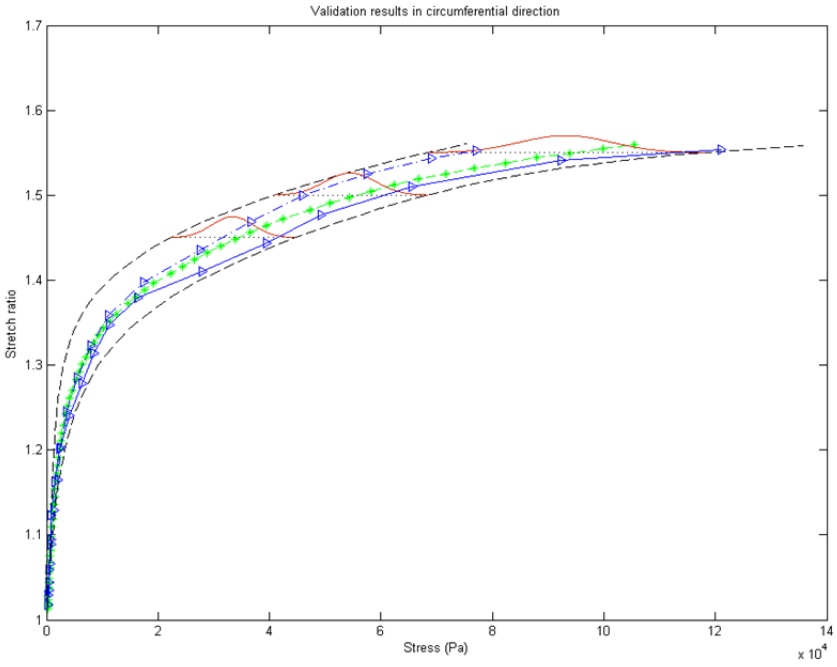

(a)

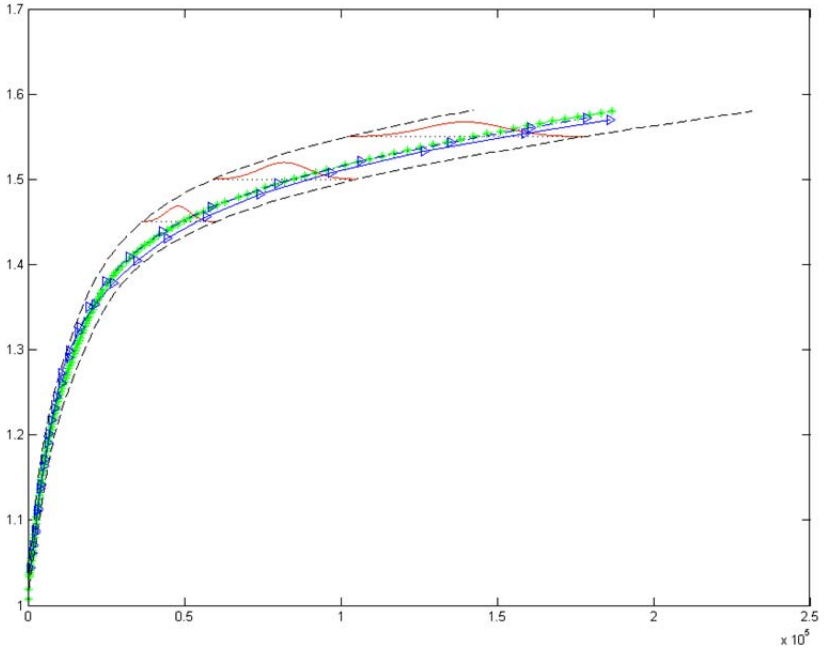

(b)

Figure.4.1.6 Stress and strain relationship of artery tissue. (a) Circumferential direction; (b) Longitudinal direction. Green (-*) mean values of stress, black (--) maximum and minimum values of stress, blue (—·) experimental data from Yamada's study, blue solid line is the experimental data from Sommer's work. Normal distribution of stress values is illustrated along horizontal bars

Three-sigma rule is widely used in industrial quality control which states that nearly all values (99.7%) lie within 3 standard deviations of the mean in a normal distribution [115]. It can also serve as an efficient tool for researchers to select useful data from the clinical dataset in scientific research. In this work, the 3-sigma rule is employed for the validation of the proposed model.

Historical tension experimental results of human femoral arteries were obtained from previous works [116, 117]. They were plotted together with simulated results in Figure.4.1.6. Although some parts of these curves are near to the minimum bound in longitudinal direction, the referenced experimental stress–strain curves still located within the three standard deviations from the mean ($\mu_T - 3\sigma_T$, $\mu_T + 3\sigma_T$) value of the simulated stress-strain curve calculated from results of the proposed approach. The results validate that the stress-strain relationship of human arterial tissues could be predicted using the nondeterministic material parameters.

4.1.5 Discussions and conclusions

Performance of an engineering system is usually influenced by many unavoidable uncertainties[118]. Similarly, medical simulation based on soft tissue modelling is also subjected to unavoidable uncertainties. Accurate modeling of soft tissue properties is a challenging task even for a simple case [119]. The challenges are classified into following categories.

Characteristics of biological tissue always vary among different subjects. The mechanical response of artery tissue is determined by a multitude of factors such as age, sex, species [120-122], vessel size and position along their length [123]. Experimental results of different specimens always exhibit a strong variability. In this case, the probabilistic modeling method which considers the systematic derivation of human tissue parameters serves as an appropriate approach to model the mechanical inhomogeneity of soft tissue.

Modeling inherently requires some simplification, thus the degree of realism of the model compared to the observations is limited by the initial assumptions that make the model valid. Finding the appropriate level of details in a model in order to fit it to the data as well as obtain meaningful predictions would require great efforts. Multiple parameters sets that satisfy the observations with similar accuracy serve as a good approach for realistic soft tissue modeling. In this work, the artery tissue was modeled with combined logarithmic and polynomial energy function. The energy function is capable of accurately modeling the nonlinear mechanical property of human artery tissues while the validity of this approach is confirmed by MC simulations.

The mathematical models describing complex dynamics will result in nonlinear formulations. Interactions between the model parameters, the model variables and the observations have a great influence on the model performance. The material models often include large number of parameters needed to be estimated. The parameter estimation problems for such models are in general difficult to solve. Genetic algorithm is utilized since it is suitable for characterization of model parameters with large parameters due to their ability to explore the entire search space looking for global minima[124].

Moreover, the parameter characterization problem will also result in non-unique solutions, where experimental observations could have resulted from a range of possible parameter sets instead of a unique set. Thus methods for estimating patient-specific parameters should consider these challenges in providing not only point estimates for the parameters but also ranges of possible parameters.

Previous works on soft tissue uncertainties analysis using probabilistic modelling have already been extensively covered. A probabilistic approach was provided for the computerized tracking of arterial walls in ultrasound image sequences [125]. Segmentation of blood vessels on magnetic resonance angiography (MRA) images was studied with a physically justified adaptive probabilistic model [126]. A probabilistic framework was also introduced for systematic descriptor selection of Minimally invasive surgery (MIS) feature tracking and deformation recovery [127]. However, there is no report on probabilistic uncertainty analysis for human artery tissue deformation simulations. Although it is very difficult to model all the uncertainties concerning the challenges above, accurate modelling of the human artery tissue inhomogeneity is noteworthy for realistic medical simulation. Probabilistic modelling approach provides a powerful tool for the study of quantitatively determine the impact of multiple variables on specific performance of human artery tissue.

In this section, we introduced a probabilistic material characterization approach which is based on genetic algorithm. Standard deviation of the material parameters is calculated using DC and IMVFOSM methods separately. The outstanding performance of IMVFOSM method in MC simulations demonstrates its better applicability in calculating standard deviation of the material parameters. The calculated results were also evaluated using relevant data from other studies on stress-strain relationships of human arteries. The accuracy of our uncertainties estimation can be improved by increasing the capacity and diversity of the sample size. The data set which indicates a reasonable stress-strain range can be utilized as reference in the virtual simulation of artery tissue. The combined logarithmic and

polynomial energy function is able to model the human arterial behavior accurately, and our proposed probabilistic approach is also applicable to be employed in other constitutive models, such as the Holzapfel model or Ogden model. The statistical model is able to represent the soft tissue properties. To the best of our knowledge, this is the first study which utilizes a statistical model to study the inhomogeneous mechanical properties of human arterial tissue.

4.2 Vascular tissue division analysis

In this section, mechanical properties of vascular tissue division during laparoscopic surgery were investigated. Laparoscopic is a popular technique for the treatment of various kinds of human diseases and injuries. The advantage of laparoscopic surgery is to replace the relatively large cuts in open surgery by small perforation holes, serving as entry points for optical and surgical instruments. Performing surgeries under these conditions requires high level of operational skills for the surgeons, which needs intensive training before laparoscopic surgery is confidently carried out. Medical simulation can provide a cost effective way to train the surgeons for required skills and to reduce the use of animal and human cadavers [128]. Many efforts have been devoted in developing surgical simulation system to provide training in laparoscopic surgery [128-130]. Haptic interactions between tool and tissue are important for effective training and improving the training outcome. Accurate modeling of tool-tissue interaction between laparoscopic tools and human arterial wall tissue can provide realistic force experienced by the trainee during laparoscopic surgery training [131]. The objective of our work is to model the cutting force and elasticity of vascular soft tissue during laparoscopic surgery.

Cutting and grasping are two basic tasks for surgical procedures. Although there are many research on tool and tissue interaction, modeling cutting force of blood vessel artery wall with laparoscopic scissors which can provide realistic simulation of surgery did not receive enough attention. Cutting blood vessel with scissors can be divided into two physical procedures: local deformation and fracture [132-134]. During the cutting process, local deformation first happens as the scissor's blade contact the tissue; then when the deformation reaches a certain level, the tissue surface begins to separate and the fracture occurs. This study focuses on the local deformation procedure which analysis the changing of tissue elasticity modulus [135], the fracture process is beyond the scope of this study.

Constitutive modeling of soft tissue mechanical properties is based on tissue biomechanics [68]. Research on mechanical properties of soft biological tissue,

i.e. vessel, liver and tendons, has been popular among researchers in the areas of tissue modeling and surgical simulation. Many spring-damper models have been proposed to help with modeling of tissue mechanics. Buchthal and Kaiser [136] first employed a set of an infinite number of Voigt and Maxwell elements to model the muscle fiber. A nonlinear application of the Kelvin model based on a sequence of springs of different natural length was proposed by Viidik [137]. The Prony model which is similar to Kelvin model is more capable of modeling organic materials accuracy as longer oscillations occurred on the Hooke's model [138]. This study provides a new approach to analyze the elasticity modulus of vascular soft tissue during deformation based on the spring and damper model.

Besides the spring and damper models, the genetic algorithm (GA) has also been successfully applied in characterization of material parameters. Khalil proposed a non-gradient-based scheme for solving the inverse elasticity problem and elasticity reconstruction of soft tissue [139]. The scheme applied the FE method and GA for elasticity characterization of atherosclerotic plaques in diseased arteries successfully. Pandit and Wang utilized GAs for the development of a two layer three-dimensional constitutive model for porcine coronary arteries and comprised genetic algorithms with experimental testing to determine the material properties of each of the two layers [140]. However, less attention has been paid to the tissue deformation during cutting process, and this is the value of this work.

Differ from previous work [141], this study employs a spring and damper model to investigate the mechanical properties of the human vessel and then implemented with an optimization method GA. For visco-elastic material, the elasticity modulus changes according to the environmental factors, such as the temperature and compression degree. The model is applied in this study to simulate the nonlinearity of elasticity modulus relative to tissue deformation during the cutting process on human iliac artery. From the experimental result obtained, we observed that the proposed spring and damper model can give us a close description of the elasticity modulus. Moreover, with the

implementation of genetic algorithm, the result can be optimized to a satisfied level as the generations increased to a certain degree.

4.2.1Modeling of the surgical tool

The shape of the laparoscopic tools is always long and slender so that the surgeon could reach the tissue within the body via the keyhole on the skin.

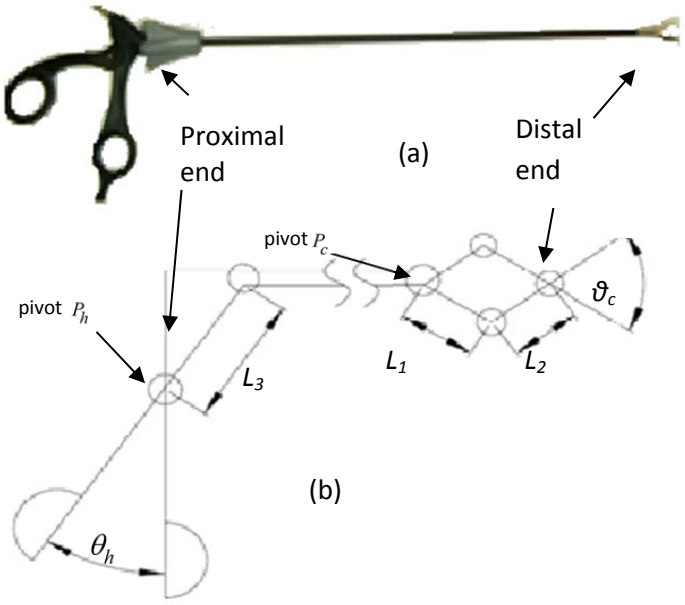

Figure.4.2.1 Laparoscopic scissors used in this section. (a) Aesculap laparoscopic scissors, Model :PO004R; (b) Schematic view of the linage mechanism of laparoscopic surgical instrument

Based on previous studies[128, 141], the torque ratio at the cutting pivot P_c to handle pivot P_h is expressed as

$$\frac{\tau_c}{\tau_h} = \frac{L_2 \cos\theta_h}{2L_3}\left[\sin(\theta_c/2) + \frac{L_2 \sin(\theta_c/2)/2L_1}{\sqrt{1 - L_2 \sin(\theta_c/2)/L_1}}\right], \tag{4.2.1}$$

where τ_c and τ_h are torques on the distal end and handle end respectively.

The normalized cutting force on the handle part with respect to thickness of cutting object is expressed as

$$f_h = \frac{x_c \cdot \cos\frac{\theta_c}{2} \cdot \exp(k_1 \frac{\theta_c}{\theta_{copen}}) / k_2 \cdot \frac{\Delta h}{h}}{\frac{RL_2 \cos\theta_h}{2L_3}\left[\sin(\theta_c / 2) + \frac{L_2 \sin(\theta_c / 2) / 2L_1}{\sqrt{1 - L_2 \sin(\theta_c / 2) / L_1}}\right]}. \quad (4.2.2)$$

Although there is no direct measurement on force and angle at the cutting or distal end, the force on the cutting blade F_c along with the angle displacement $\Delta\theta$c can be calculated from Eq. 4.2.1 and Eq. 4.2.2 using the data measured from the handle or proximal end, thus enable us to compute the relative tissue displacement in response to cutting force.

4.2.2 Soft tissue modeling

To model the cutting force during local deformation, elasticity is a key parameter in generating the reactive force. Elasticity considers the elastic nature of the tissue but does not account for the energy loss in the tissue which is of viscous nature. Vascular soft tissue, like most soft tissues, combines elastic and viscous behaviors. It possesses the features of hysteresis, relaxation and creep that are prominent features of viscoelasticity.

Our experiment was carried out with a constant angular speed, so the contact force and tissue displacement were measured in the same time. The two common ways to model the viscoelasticity of vascular soft tissue are linear viscoelastic model and nonlinear viscoelastic model. To simulate the cutting process, as the angular displacement was very small and the experiment was performed in a constant angular speed, we propose a spring and damper model which is modified from the Kelvin model to model the vascular soft tissue (Figure. 4.2.3).

Maxwell, Voigt and Kelvin are the models commonly implemented in soft tissue modeling [136, 137] (Figure. 4.2.2 (a), (b),(c)). The notations, F, η and μ_i represent the force acting on the model, viscosity coefficient of damper and spring constants respectively.

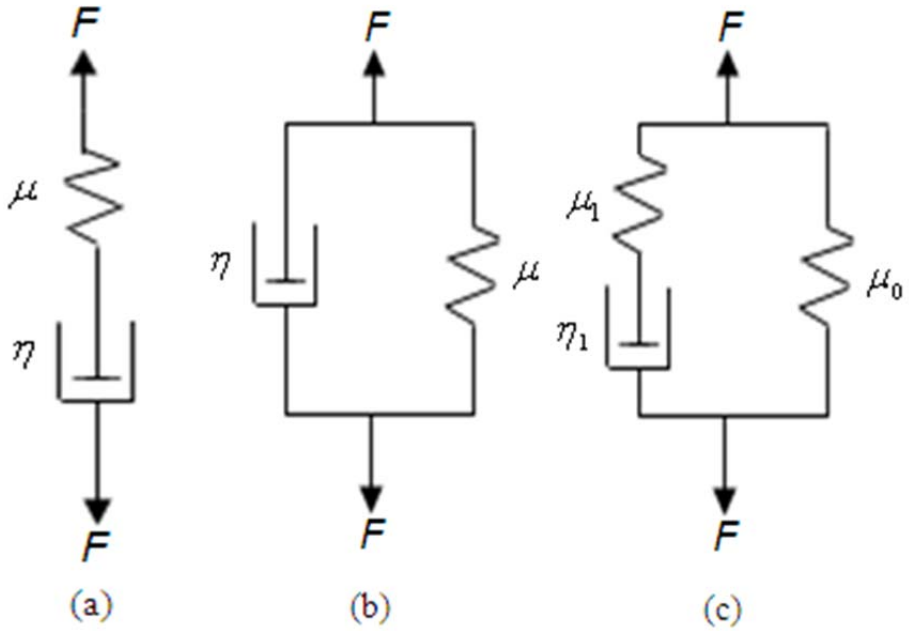

Figure.4.2.2 Mass spring models used in medical simulation. (a) Maxwell model; (b) Voigt model; (c) Kelvin model

In this study, we analyze the local deformation process which is the minimal deformation prior to the break strain for laparoscopic scissor to divide the vascular soft tissue. Hence, we may consider the vascular soft tissue model as a linear viscoelastic model.

In order to select the appropriate model for this study, we have compared the curve fitting results of the Maxwell, Voigt and Kelvin model with the experimental data. After a small modification to the Kelvin model, the proposed modified Kevin model performs better than the other models in representing the experimental data with highest R-square values. The modified Kelvin model is used as the mechanical model in this study.

The mathematical equations governing the proposed model (Figure. 4.2.3) are as follows:

$$F + \tau_\varepsilon \dot{F} = E_R \left(u + \tau_\sigma \dot{u} \right) . \tag{4.2.3}$$

where $$\tau_\varepsilon = \frac{\eta_1}{\mu_1}, \tau_\sigma = \frac{\eta_1}{\mu_0}\left(1 + \frac{\mu_0}{\mu_1}\right), E_R = \mu_0$$

Cutting was performed on test samples to obtain relevant force and displacement results under a constant velocity. The stress-strain stiffness relationship can be easily calculated from these results.

4.2.3 Tool-tissue interaction modeling

The tool-tissue interaction model as shown in Figure.4.2.3 using the proposed mass-spring model can be derived via Laplace transformation. Eq. 4.2.6 is the resultant mathematical representation.

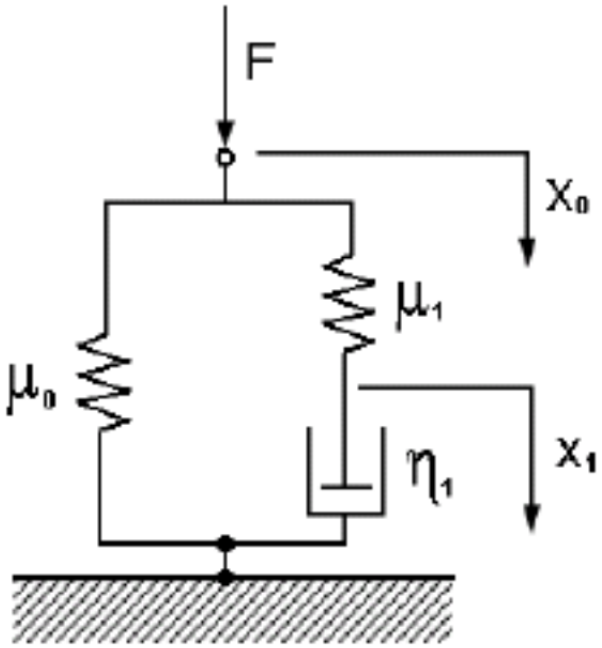

Figure.4.2.3 Modified model with variables

The relationship between total displacement x_0 and pressure force F can be represented as following:

$$x_0 = \left(\frac{\mu_1}{\mu_0 + \mu_1} \right) x_1 + \frac{F}{\mu_0 + \mu_1}, \tag{4.2.4}$$

where μ_0 and μ_1 are the spring coefficients.

The velocity of the damper can be described by Eq. 4.2.5.

$$\dot{x}_1 = \frac{\mu_1}{\eta_1} x_0 - \frac{\mu_1}{\eta_1} x_1 , \tag{4.2.5}$$

where η_1 is the viscosity coefficients.

The relationship between force and displacement u (same as x_0 in the Figure. 4.2.3) can be obtained using:

$$F(t) = F(0)e^{-t\frac{\mu_1}{\eta_1}} + \mu_0 u\left(1 - e^{-t\frac{\mu_1}{\eta_1}}\right). \quad (4.2.6)$$

In order to analyze the mechanical properties of the vascular soft tissue using the proposed model, the force data are divided into two parts corresponding to the local deformation process and fracture process. The peak force occurs at the point separating the two processes. Simulation was conducted with the force data from local deformation process. With the force data and the angular displacement measured at the handle of the surgical tool during the experiment, the force on the cutting blade along with the displacement at the cutting end can be calculated.

The force reading will be recorded from zero to peak value as the cutting process move from local deformation to fracture. In this case, the coefficient *F(0)* in Eq.4.2.6 is assumed to be zero. The average velocity of the scissors' blade during local deformation is calculated as:

$$v = wl\,, \quad (4.2.7)$$

where w is the angular speed of motor, and l denotes the average length from the contact area to the pivot of the scissors' blade.

From Eq.4.2.7 and the time t in Eq.4.2.6 equates to u/v,

$$F(u) = \mu_0 u\left(1 - e^{-\frac{u}{v}\frac{\mu_1}{\eta_1}}\right). \quad (4.2.8)$$

This equation successfully connects the force with tissue displacement together. The elasticity modulus of a material can be used to calculate the force as it exerts under specific strain by Eq. 4.2.9:

$$F = EA_0\Delta L / L_0\,, \quad (4.2.9)$$

where F is the force exerted by the material when compressed or stretched by ΔL, A_0 is the original cross-sectional area through which the force is applied; ΔL is the total displacement; L_0 is the original length of the object; E is the elasticity modulus.

Hooke's law can be derived from this formula, which describes the stiffness of an ideal spring

$$F = (EA_0 / L_0)\Delta L = kx, \tag{4.2.10}$$

where k is the spring constant, and $k = EA_0 / L_0, x = \Delta L$.

Therefore, with Eq.4.2.8 and Eq. 4.2.10, we can derive the following equation:

$$F(u) = \mu_0 u\left(1 - e^{-\frac{u}{v}\frac{\mu_1}{\eta_1}}\right) = ku = \frac{EA_0}{L_0}u, \tag{4.2.11}$$

where u denotes the displacement.

From Eq.4.2.11 the spring constant and elastic modulus can be derived as,

$$k = \mu_0\left(1 - e^{-\frac{u}{v}\frac{\mu_1}{\eta_1}}\right), \tag{4.2.12}$$

$$E = \mu_0 L_0\left(1 - e^{-\frac{u}{v}\frac{\mu_1}{\eta_1}}\right) / A_0. \tag{4.2.13}$$

From Eq.4.2.8 and Eq.4.2.13, the relationship between cutting force, elasticity modulus and tissue displacement is established. With these equations, we can determine the value of the coefficient in Eq.4.2.11 by curve fitting the experiment data. The elasticity modulus with respect to the proposed mass spring model could be estimated.

4.2.4 Genetic algorithm design

After we obtained the parameters in Eq.4.2.11, genetic algorithm was implemented to determine and optimize the mechanical parameters of the artery wall.

Hyperelastic constitutive models can accurately represent most of the biological soft tissues including the arterial walls, where the nonlinear nature of the stress-strain curve is analyzed by the strain energy functions at high strains. Towards realistic elasticity estimation, however, simpler and more direct linear elastic model are more welcomed by the researchers as the limitations of the results of such estimation are understood.

A body being deformed by an external load or displacement can be described by its constitutive relationship and by stress equilibrium [139]. It is assumed that each point on the boundary of the solid is specified either by a stress or displacement and that *v(x, y, z)* denotes the displacement field as a function of spatial coordinates *(x, y, z)*. Skovoroda [142] proposed the "plane strain inversion equation" for the single unknown shear modulus μ as follows:

$$\frac{\partial^2(\varepsilon_{xy}\mu)}{\partial y^2} - \frac{\partial^2(\varepsilon_{xy}\mu)}{\partial x^2} + 2\frac{\partial^2(\varepsilon_{xx}\mu)}{\partial x \partial y} = 0 . \qquad (4.2.14)$$

Although the direct inversion can solve this set of partial differential equations for the shear modulus efficiently, it is not practical to use direct inversion approach as the solutions are difficult to stabilize. Eq.4.2.14 requires an explicit form for the strain field. However, the strain field is difficult to measure in multi dimension during the cutting process.

To overcome these disadvantages, the partial differential equations can be iteratively inverted by fashioning it into a nonlinear least squares (NLS) problem in order to minimize the residuals between computed and measured mechanical response(i.e., displacement fields).

The resulting system is the Inverse Problem (IP) [143] in elastography, and is written as:

Given v_c: Rp -> Rq, $q \geq p$, solve

$$\min_{E \in R^p} \{\Phi(E) = 1/2 \| v_c(E) - v_a \|^2\}, \tag{4.2.15}$$

where E represents the elastic modulus distribution, a one-dimensional vector $(p=1)$ assuming an isotropic distribution, $v_c(E)$ denotes the computed displacement based on a given E, and v_a is the measured displacement.

The genetic algorithm (GA) [144] is a global search tool that attempts to mimic biological evolution. It begins with a population of potential solutions and evaluates their level of fitness in the problem domain and creates a new set of approximation based on breeding the better evaluated solutions. The cycles of selection leads to the evolution of populations of individuals that are better suited, on average, to their environment than their parents, similar to natural selection.

As it is described in Khalil's work [139], the skeleton underlying different genetic algorithms differs from each other, while the parameters governing the genetic operations are highly problem specific. Choose the right way to represent the data and the population (P) of candidate solutions is the first job. In this case, the optimal elastic modulus value for the lumped material regions given some mechanical responses is the objective we desired. Thus, an array of modulus values will represent a candidate solution. The GA is initialized by generating a distribution of elastic modulus values at random relative to the target modulus and then assigning them to the candidates in the population, of chosen population size.

A fitness value is computed for each candidate solution in the population through the objective function or fitness function; this quantifies how "fit" a candidate is as compared with others, in other words whether it is likely to survive and reproduce. The fitness function on this study is based on the inverse elasticity problems of Eq. 4.2.15 which requires the minimization of a residual between measured and predicted displacement fields.

$$\mathrm{f}_i = \Phi(E_i), \tag{4.2.16}$$

where i represents a particular lumped material region and E_i is the vector of elasticity values for elements in that specific region.

From Eq. 4.2.13, we can get the forward equation that link displacement to the elasticity modulus as follows:

$$v(E) = -\frac{v\eta_1}{\mu_1}\ln(1-\frac{EA_0}{\mu_0 L_0}), \qquad (4.2.17)$$

where η_1, μ_1 *and* μ_0 are parameters which can be figured out from the fitting result of proposed elasticity equation.

The set of candidate solutions was initially populated by randomly generating elasticity values within an order of magnitude of the target values, producing each initial population with 50 candidate solutions. The experimental data is divided into 396 groups to investigate the desired elasticity modulus relative to a particular region. Each group consists of 50 solutions, which will serve as the measured displacement in the fitness function.

4.2.5 Experiment design and results

Figure.4.2.4 illustrates the experimental set up. Laparoscopic scissors were actuated by a stepper motor. Force applied on the handle was measured with a force sensor (Imada DS2 50N). Webcams were employed to take images and measure the angular displacement of the handle and scissors' blades.

Three pieces of human iliac arterial specimen were collected from donors. Thickness of specimens is listed in Table.4.2.1. Krebs ringer solution was sprayed onto the specimens during experiment. The specimens were cut with the laparoscopic scissors at a speed of 0.03 radian/second. In the beginning of each cutting process, the blades of scissors were fully opened (θ_{copen} = 0.6822 radian). It is assumed there was no initial compression force applied onto specimen by the scissors' blades. During the cutting process, force applied on handle F_h and angular displacement of handle θ_h were acquired.

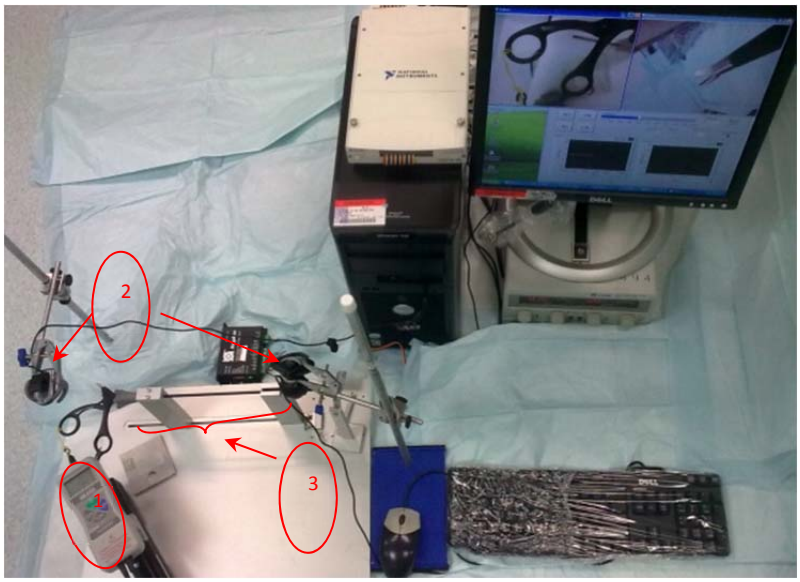

Figure.4.2.4 Experimental set-up. Part 1 indicates the force sensor; Part 2 denotes the webcams; Part 3 is the laparoscopic scissor

Table.4.2.1 Average thickness of specimen, and number of cuts per specimen

Specimen Number	1	2	3
Average thickness (mm)	2.1	3.2	3.2
Number of cuts	1	2	2

The cutting force with respect to the displacement of handle is shown in Figure. 4.2.5. The cutting process can be divided into three regions: 1: contact region (local deformation). 2: cutting region. 3: completion region. This study will focus on the contact region, in which the proposed equations are applied.

From the measure data, the average moving velocity of scissor's blade v is 0.000193 m/s, the inner radius of the blood vessel is 2.5mm, and outer radius is 4mm. After compressing, the original length of the specimen L_0 is 3mm, and as the outer circumference is 25.12mm, thus the cross-sectional area A_0 is about 36mm^2, with these two parameters, we can calculate the experimental elasticity modulus with respect to relative tissue displacement. Figure.4.2.6 and Table.4.2.2 illustrate the fitting results by curve fitting tool of MATLAB and genetic algorithm.

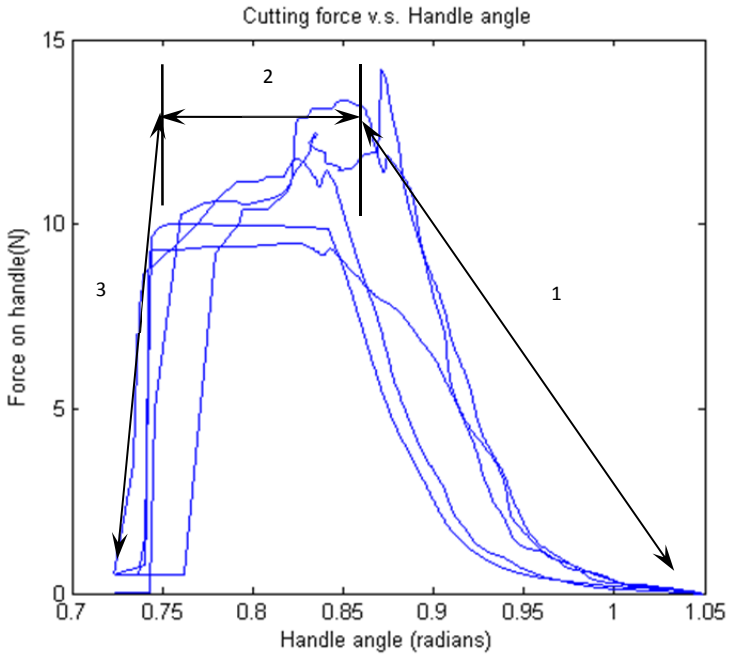

Figure.4.2.5 Three pieces of human iliac artery were cut with five cuts. The cutting process is divided in to three regions. (1) Contact region. (2) Cutting region. (3) Completion region

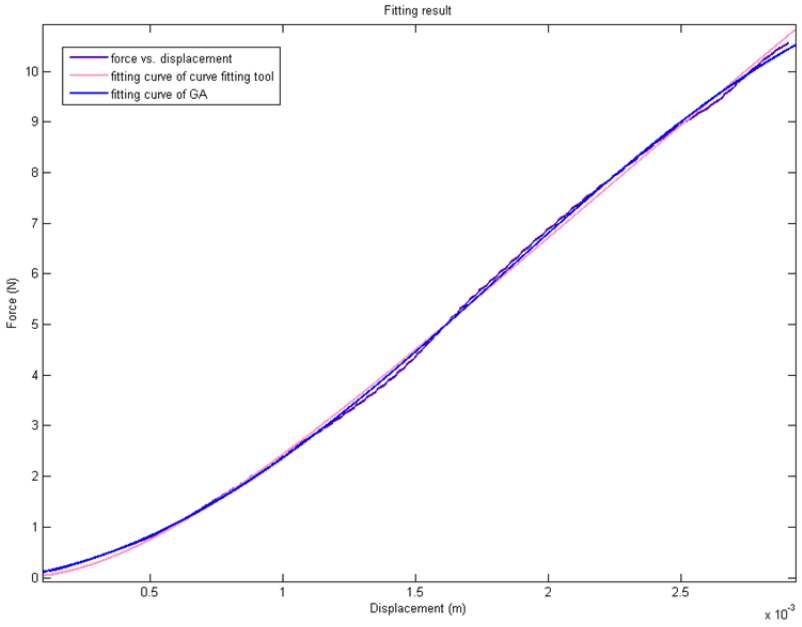

Figure.4.2.6 Fitting result of experimental force using curve fitting and GA

Table.4.2.2 Fitting results of model parameters with experimental data

Name	μ_0	μ_1	η_1	R-square
Value of curve fitting tool	3906	6370	33710	0.9827
Value of GA	3930	109.1	590.6	0.9989

The fitting result shows that the elastic force model is able to fit the average normalized force-displacement angle curve well. Table.4.2.2 shows the fitting result of the parameters in Eq.4.2.11 with different methods. The difference between experimental data and proposed equation illustrated in Figure.4.2.6 may come from the mechanical error and friction of the equipment, and bring about the noise in tissue displacement's measurement.

These results also indicate that the optimization method-GA performs better than the curve fitting tool, which show good ability in coping with the noise of measurement. With enough genetic generations, the initial random elasticity value can converge to the most fitted experimental value.

4.2.6 Discussions and conclusions

Estimation of mechanical parameters in human artery wall is a challenging problem with clinical implications. An accurate mechanics model of soft tissue enables the trainees to get the operation experience through the training of haptic simulation system. The objective of this study is to find an optimal method to estimate the elasticity modulus of human artery wall.

The cutting process of human artery was divided into two processes; the local deformation process was analyzed to obtain the relative elasticity modulus under different displacements. The proposed mechanical model is established with respect to the comparison test among different models. The dynamic modeling of force and tissue interaction was also demonstrated by implementing the proposed tissue model, which is based on the Kelvin model. Validation of the proposed elasticity equation was carried out by curve fitting the experimental data onto the equation. The fitting result shows that the proposed elasticity equation can basically model the elasticity curve based on the experimental data.

An optimization method was also proposed in this work to improve elasticity reconstruction problem. The results showed that the elasticity modulus can be optimized to fit the experimental results well with the increasing of generations.

The proposed mechanical model was used to study the structural mechanics of the human artery tissue whereas the genetic algorithm served to optimize the mechanical characteristics in the local deformation process. While the presented problem focused on the optimization of the local deformation process during the cutting of human artery wall, the proposed method could be applied to other materials and structures. Furthermore, the validated models are mainly linear viscoelastic in nature with the assumption of minimal deformation. However, to cater for larger deformation, nonlinear viscoelastic model has to be considered. Thus, a more refined and complex mechanical model has to be investigated; for example, the quasi-linear viscoelastic model which caters for both minimal and large deformation onto soft tissues. The resulted version could then be used as a general model for both the linear and nonlinear conditions.

Chapter 5 Haptic Rendering for Soft Tissue Deformation

Mathematical models provide physics for realistic rendering of soft tissue deformation, in which the nonlinear mechanical tissue properties can be represented accurately. The constitutive models is first applied to a gallbladder model and implemented in a deformation simulation system with haptic feedback in Section 5.1. It is then utilized in combination with haptic guidance in a surgical training system for tracheal reconstruction in Section 5.2.

5.1 Modeling and simulating of gallbladder tissue

Medical simulation provides a cost effective way for surgical training, and it helps to reduce the need for animal and human cadavers [145, 146]. It has been used to investigate tissue injury mechanisms and improve the design of surgical tools [147]. Medical simulation of surgical training requires a realistic training environment with tool-tissue interaction modelling[148]. Haptic feedback with an accurate tool-tissue interaction model may enhance the realism and effectiveness of surgical training [149].

Biological soft tissue is non-homogeneous and anisotropic. Many studies [68, 77, 150] have explored various mechanical models for different types of soft biological tissue, and the mechanical response of these materials is extremely nonlinear. For instance, the brain tissue is often modeled with hyperelastic constitutive equations [151, 152]. Arterial tissues have been studies by Holzapfel, Ogden and Gasser using hyperelastic anisotropic models [153-155] and by Yang using quasi-linear viscoelastic model [12]. Due to the presence of reinforcement fibers in the extracellular matrix, biological tissues such as the gallbladder wall always exhibit mechanical anisotropy [152, 153, 156].

Gallbladder is a balloon-like material filled up with bile produced from liver. Understanding the mechanical properties of a gallbladder is important for constructing a realistic surgical simulation system for cholecystectomy surgery. Lee et al. proposed a laparoscopic cholecystectomy simulator with a force-feedback device [157]. Although this simulator could improve the realism

through real-time interaction with force feedback and visual feedback, the deformable model was too simple to realistically simulate the biomechanical properties of a gallbladder and its surrounding tissues. A mass-spring-damper gallbladder model for laparoscopic cholecystectomy simulation was proposed by Webster [158]. This model focused on accelerating the computation speed by incorporating an approximate solver that pre-computes the solution to a linear system. Although these works may provide valuable deformable models for gallbladder deformation simulation, the nonlinear mechanical property, which is important for realistic deformation simulation and haptic rendering of surgical simulation, received little attention.

Reality based modeling and simulation can be used to obtain pertinent understanding towards organ and tissue deformation. From the in vitro experiments with porcine gallbladder tissues, we developed an accurate deformable model of the gallbladder representing its wall and organ tissues using nonlinear variational constitutive models. Elongation tests were performed on the gallbladder wall tissue. Nonlinear constitutive laws were derived based on the Fung-type exponential strain energy function, and the anisotropic behavior of gallbladder wall tissue was modeled using the exponential strain energy function. Previous studies on brain tissue [88] and arterial tissue [159] illustrated that the exponential strain energy function can model the tissue anisotropic behavior well. Indentation tests were also carried out on the gallbladder organ. It is assumed that the strain energies admit decomposition into deviatoric and volumetric parts [160, 161]. In this chapter, we introduce a new volumetric function which accounts for the incompressible material behavior in the energy function. The variation approach enables real time simulation of accurate soft tissue deformation. Reality-based modeling and simulation method is also applicable to other hollow organs such as stomach and pancreas.

Section 5.1.1 describes gallbladder organ modeling. Section 5.1.2 describes the in vitro experiments. In Section 5.1.3, the Genetic Algorithm was used to identify the parameters of the deformation model from the experimental data. Section 5.1.4 and Section 5.1.5 present the modeling results for gallbladder

wall and gallbladder tissue, respectively. Section 5.1.6 discusses the applications of the proposed model for deformation simulation and haptic rendering in a surgical simulator. Section 5.1.7 concludes the study with a discussion and introduces some future works. The work flow of this study is shown as follows:

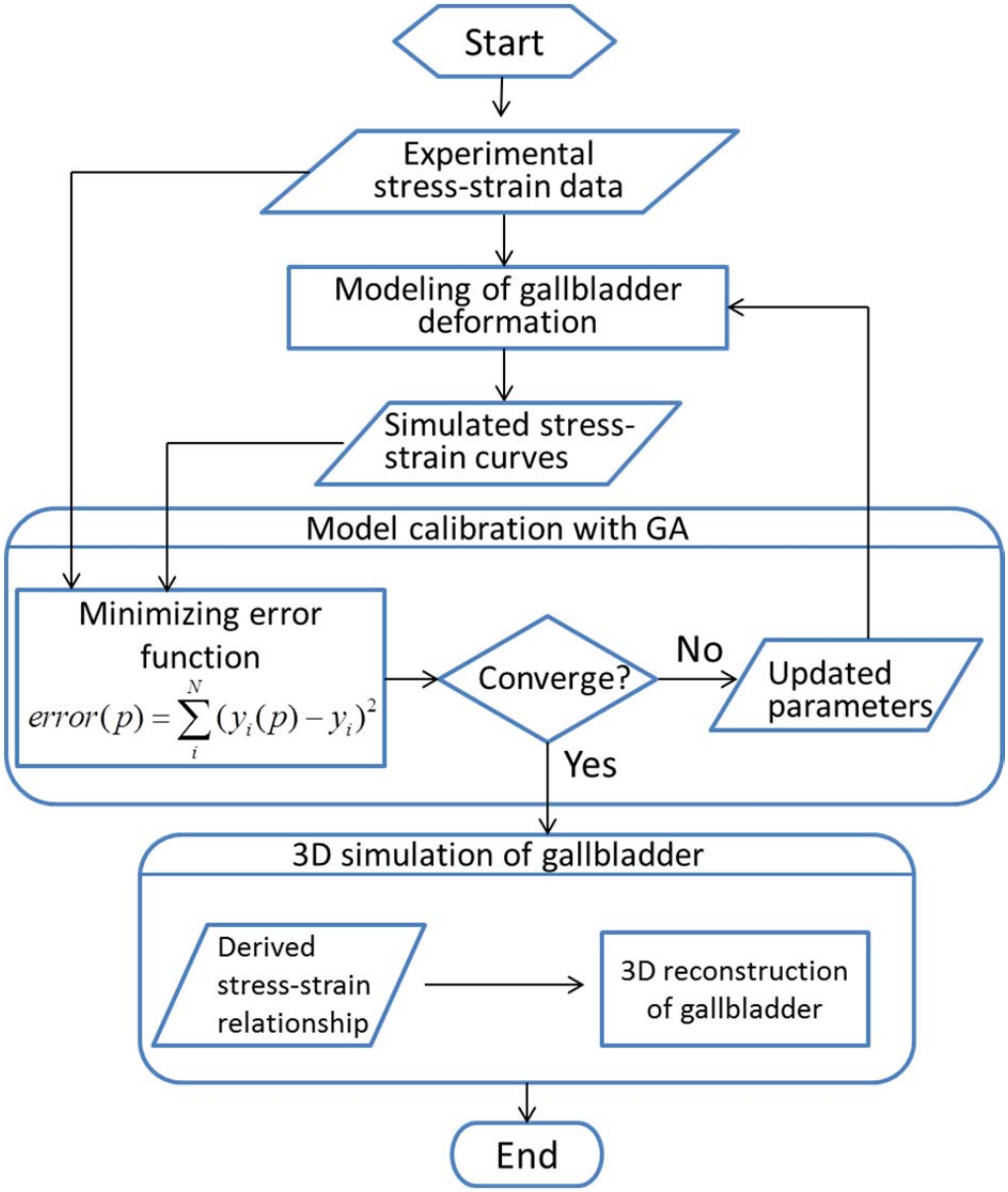

Figure.5.1.1 Work flow of the study

5.1.1 Gallbladder modeling

The proposed gallbladder model is an integrated model comprising the wall and hollow organ body of the gallbladder. Firstly, the gallbladder wall tissue is

modeled using a Fung-type exponential strain energy function. The gallbladder organ is next modeled with our proposed energy model. It combines the exponential strain energy function which accounts for elastic deformation and volumetric energy function that represents the incompressible feature of gallbladder organ.

For anisotropic materials like the gallbladder wall, an exponential strain energy function introduced by Fung [162] is employed to model the mechanical properties of gallbladder wall. It is presented as a function of Green strain tensor components, E_i, and is typically expressed as:

$$W = \frac{c}{2}(e^{Q} - 1), \tag{5.1.1}$$

in which

$$Q = a_1 E_\theta^2 + a_2 E_z^2 + a_3 E_r^2 + 2(a_4 E_\theta E_z + a_5 E_z E_r + a_6 E_\theta E_r), \tag{5.1.2}$$

where W represents the pseudo-strain energy, c expresses the units of stress (force/area), and a_1, a_2, a_3, a_4, a_5 and a_6 are dimensionless constants r, θ, z, denotes the radial, circumferential, and axial directions in polar coordinates .

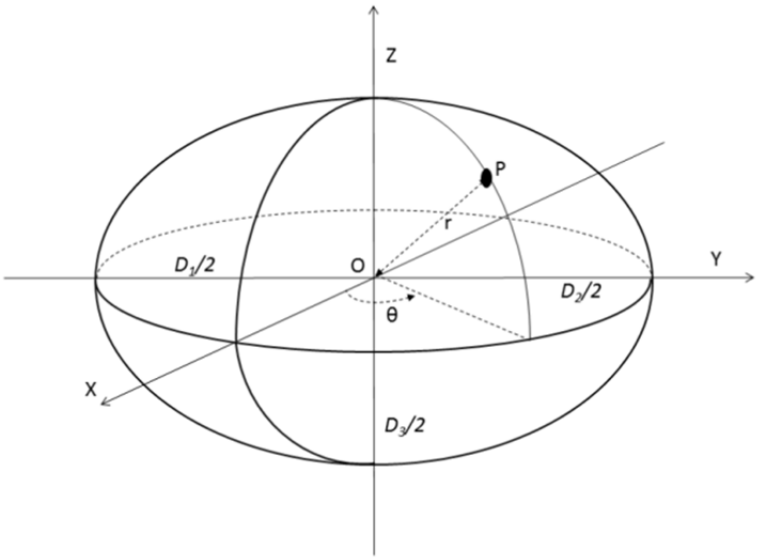

Figure.5.1.2 Geometrical shape of the gallbladder organ in polar coordinates. The major axis length is D_1, the minor axes lengths are D_2, and D_3 ($D_1 > D_2 > D_3$), the gallbladder is subjected to a uniform internal pressure. The stress due to this pressure at a surface point *P* has three components: σ_r (radial), σ_θ (circumferential), and σ_z (axial)

The gallbladder is considered to be a thin-walled elastic ellipsoid membrane. The wall thickness is very thin compared to the circumferential length of the gallbladder wall. Thus it is able to justify the assumption that the normal stress σ_r in the radial direction is negligible compared with the normal stress σ_θ in circumferential direction [162]. Thus, the gallbladder wall is treated as a two-dimensional body subjected only to Kirchhoff stresses S_θ and S_z, which are functions of Green and St.Venant strain E_θ and E_z . σ_θ and σ_z are approximately uniform throughout the wall thickness. Thus, the problem can be reduced into a two-dimension question, and Eq.5.1.2 can be rewritten as:

$$Q = a_1 E_\theta^2 + a_2 E_z^2 + 2a_4 E_\theta E_z \ . \tag{5.1.3}$$

Relationships between Kirchhoff stresses, Green stresses, strain ratio and exponential strain energy functions are given as following:

$$S_\theta = \frac{\sigma_\theta}{\lambda_\theta^2} = \frac{\partial W}{\partial E_\theta}, \tag{5.1.4}$$

$$S_z = \frac{\sigma_z}{\lambda_z^2} = \frac{\partial W}{\partial E_z}, \tag{5.1.5}$$

where λ_θ and λ_z denotes the stretch ratios of the middle surface of the gallbladder wall in the circumferential and axial directions, and

$$E_\theta = \frac{1}{2}(\lambda_\theta^2 - 1), \tag{5.1.6}$$

$$E_z = \frac{1}{2}(\lambda_z^2 - 1). \tag{5.1.7}$$

Thus, the relationship between normal stress and stretch ratio is shown as follows:

$$\sigma_\theta = \lambda_\theta^2 \cdot \frac{\partial W}{\partial E_\theta} = c \cdot \lambda_\theta^2 \cdot (a_1 E_\theta + a_4 E_z) \cdot e^Q, \tag{5.1.8}$$

$$\sigma_z = \lambda_z^2 \cdot \frac{\partial W}{\partial E_z} = c \cdot \lambda_z^2 \cdot (a_4 E_\theta + a_2 E_z) \cdot e^Q. \tag{5.1.9}$$

Gallbladder organ is assumed to be an incompressible object made of rubber-like biological nonlinear material. In analyzing the behavior of biological nonlinear materials, the deviatoric and volumetric decoupling of the strain energy function is frequently applied [88], and the two parts can be treated independently. The energy model for the gallbladder organ is shown in Eq. 5.1.10. The exponential strain energy function (Eq.5.1.11) in the gallbladder wall model can serve as the deviatoric part.

$$W = W_{dev} + W_{vol}, \tag{5.1.10}$$

where $$W_{dev} = \frac{c}{2}(e^{(a_1E_\theta^2 + a_2E_z^2 + 2a_4E_\theta E_z)} - 1). \tag{5.1.11}$$

Our volumetric strain energy function is derived based on the proposed function (Eq.5.1.12) in literature [160]. Eq.5.1.12 is able to fulfill all the volumetric conditions for incompressible materials [160]. The volumetric part which accounts for the incompressible feature of gallbladder organ is shown in Eq.5.1.13. A scale parameter *t* is added in the equation so as to fit the shape of the function to experimental data.

$$U = K \cdot [(J-1)^2 + (\ln J)^2]/4, \tag{5.1.12}$$

$$W_{vol} = K \cdot t^{-2}[(J-1)^2 + t(\ln J)^2]/4, \tag{5.1.13}$$

where K (39kPa) denotes the bulk modulus of the material and $J = \lambda_\theta \lambda_z$ is the determinant of the deformation gradient. The relationship between normal stress and stretch ratio for the gallbladder can be derived as:

$$\sigma_\theta = \lambda_\theta^2 \cdot \frac{\partial W}{\partial E_\theta} = \lambda_\theta^2 \cdot (c \cdot (a_1E_\theta + a_4E_z) \cdot e^Q + \frac{K}{4} \cdot t^{-2} \cdot (2E_z + 1 - \frac{\sqrt{2E_z+1}}{\sqrt{2E_\theta+1}} + \frac{t}{2E_\theta+1} \cdot \ln((2E_\theta+1)(2E_z+1)))), \tag{5.1.14}$$

$$\sigma_z = \lambda_z^2 \cdot \frac{\partial W}{\partial E_z} = \lambda_z^2 \cdot (c \cdot (a_4E_\theta + a_2E_z) \cdot e^Q + \frac{K}{4} \cdot t^{-2} \cdot (2E_\theta + 1 - \frac{\sqrt{2E_\theta+1}}{\sqrt{2E_z+1}} + \frac{t}{2E_z+1} \cdot \ln((2E_z+1)(2E_\theta+1)))), \tag{5.1.15}$$

where $E_\theta = \frac{1}{2}(\lambda_\theta^2 - 1)$ and $E_z = \frac{1}{2}(\lambda_z^2 - 1)$ denote the Green strain.

The engineering stress *T*, which is generally measured in biomechanical testing, is expressed as:

$$T_i = \sigma_i / \lambda_i \ , \tag{5.1.16}$$

where *i* denotes circumferential and axial directions.

5.1.2 Experiments

Experiments were carried out with a mechanical property testing system which is the same as in Chapter 4, section 4.1.1. Five porcine gallbladders were obtained from a local slaughterhouse and stored in an ice box with Histidine Tryptophan Ketoglutarate (HTK) solution before experiment. All gallbladder specimens were excised from the end portion of liver organs, with length 90-100 mm and diameters 35-45 mm.

Experiment was conducted in two steps. Firstly, an indentation test (Figure.5.1.3 (a)) was carried out on the gallbladder organ in both longitude and circumferential directions. A stick (made of Fulcure Vero gray by Rapid Prototype) with a diameter of 5mm was used to perform the indentation test on the center of the gallbladder surface. Secondly, an elongation test of gallbladder wall (Figure.5.1.3 (b)) was performed with the same gallbladder, and it was cut into rectangle strips in circumferential and longitudinal direction. The elongation test was carried out with the specimen submerged in Krebs ringer solution (heated to around 40ºC), so as to mimic the internal environment of porcine model. Specimen sizes including length, width and thickness were measured. All specimens were preconditioned before data collection. The specimens would reach a steady state as no further changes occurred on the stress-strain curve after five cycles[68].

During the experiments, force data were collected when the load cell detected the load at positive readings. For the elongation test of gallbladder wall, stretch ratio λ was determined by dividing instantaneous gauge length by its original length, and stress σ was determined by dividing the instantaneous

load by the original cross-sectional area. The elongation test was performed until the stretch ratio of 1.3 in both longitudinal and circumferential directions at a ramping speed of 2.5mm/s.

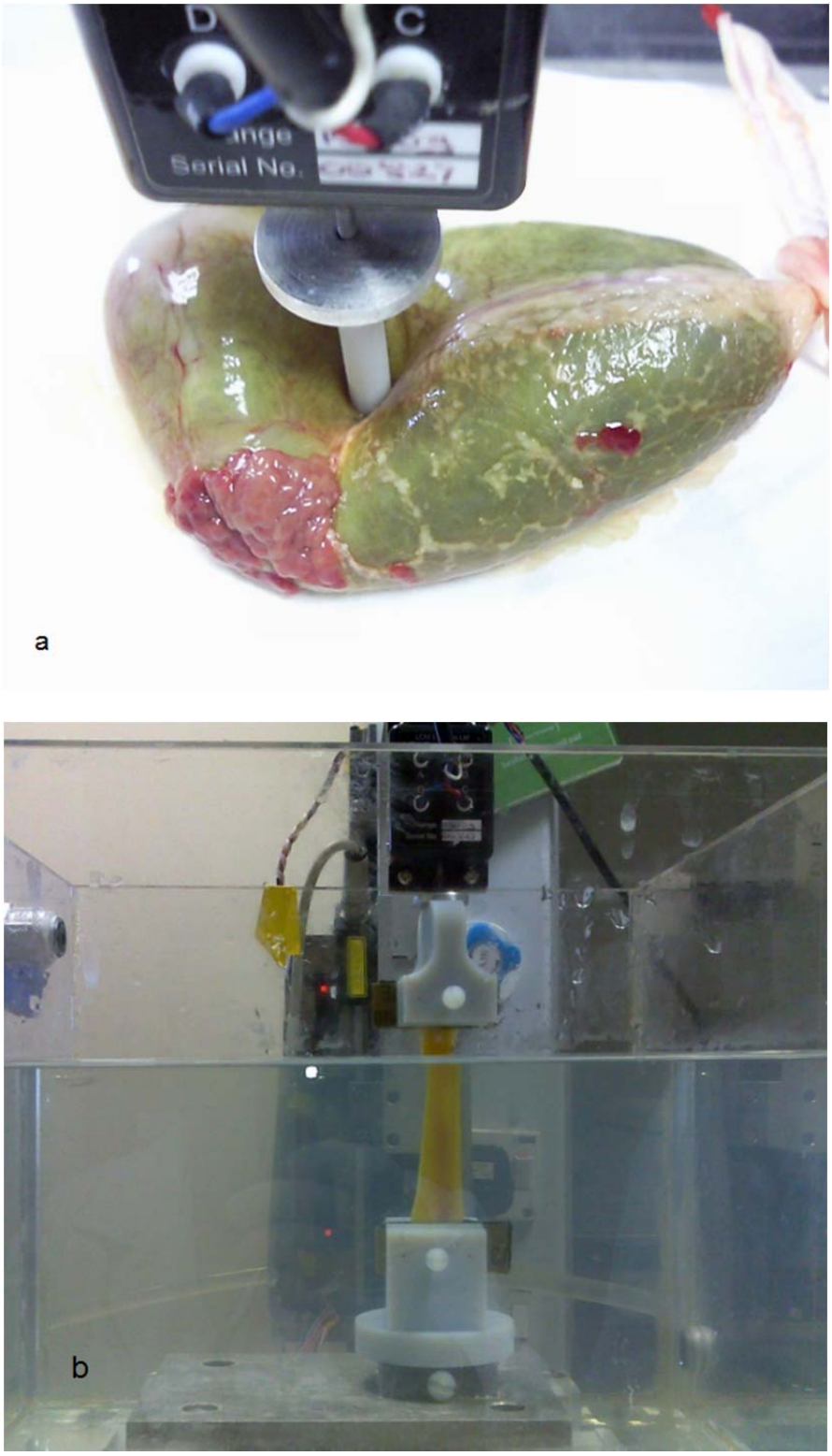

Figure.5.1.3 Images of the experiments. (a) Indentation tests on gallbladder organ; (b) Elongation tests on gallbladder wall tissue

5.1.3 Parameters identification using the Genetic Algorithm

GA is employed for identification of the material parameters. A collection of experimental results is available for model parameter identification, through a data set of the form

$$\{[x_i, y_i]_{i=1,\ldots,N_p}\}, \tag{5.1.17}$$

where x_i is the experimental strain measure while y_i is the corresponding recordings of stress measure, N_p is the number of data points collected from the experiment. The best-fit values of selected parameters

$$p = \{\{p_m\}_{m=1,\ldots,P}\}, \tag{5.1.18}$$

are sought, P is the total number of selected parameters.

With the parameter set p_i, numerical simulations of the experiments can be employed to get a set of predictions

$$\{[x_i, y_i(p)]_{i=1,\ldots,N_p}\}. \tag{5.1.19}$$

The error function for the identification process is given as following:

$$error(p) = \sum_{i}^{N} (y_i(p) - y_i)^2 . \tag{5.1.20}$$

The identification process is solved by minimize the error function, the data set that can provide the minimum error results. After starting with a population of potential solutions, the GA will evaluate their level of fitness in the problem domain and create a new set of approximations based on breeding the better evaluated solutions. By repeating the selection, crossover and mutation procedures, the evolution of populations of individuals that are better suited to their environment than their parents are reached. An initial population of 200 individuals was used along with a selection percentage of 0.1 and a crossover percentage of 0.7. The algorithm would begin to converge to minima after approximately 80 generations while the number of total evolution generations is set to be 200.

A correlation coefficient for the relation between predicted and experimental stress was used to determine the goodness of the fitting result. The root-mean-square error with respect to the mean value was also calculated to evaluate the goodness of the fit.

5.1.4 Gallbladder wall modeling

Uniaxial elongation tests had been performed on five sets of gallbladder tissue in both longitudinal and circumferential directions. The feasibility of the engineering stress equation derived from exponential strain energy function was characterized by GA. The mean stress and standard deviation of the experiment results are shown in Figure.5.1.4. As shown from the graph, the specimens are found to be stiffer in circumferential direction than in longitudinal direction while the standard deviation is also larger in circumferential direction than in longitudinal direction.

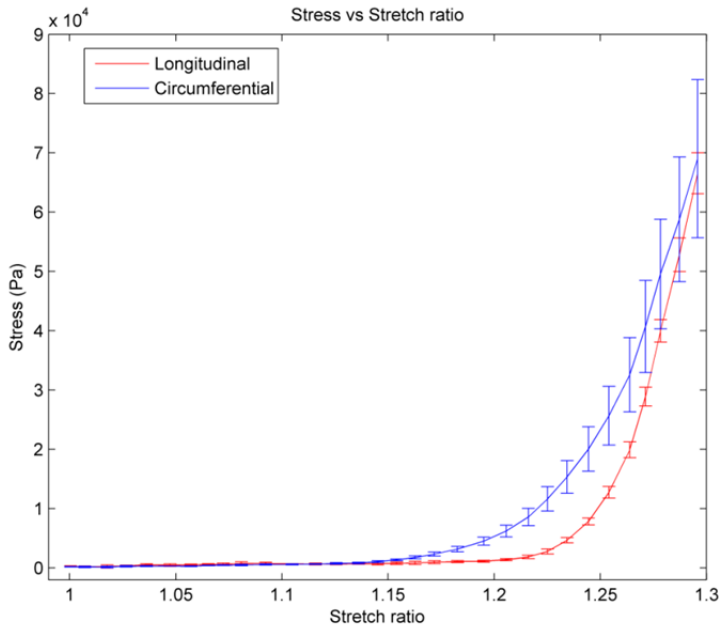

Figure.5.1.4 Experimental results of uniaxial elongation tests on gallbladder wall tissue in longitudinal and circumferential directions. Solid line shows the mean stress of 5 specimens, vertical bar shows the standard deviation of stress

Based on the exponential strain energy model, the engineering stress-strain model was applied to fit the experimental data with GA. The first set of parameters for the uniaxial elongation test was selected as follows:

$$p = \{c, a_1, a_2, a_4\} \text{ (P=4).} \qquad (5.1.21)$$

The GA estimated results are shown in Table.5.1.1 where five sets of parameters are listed. R^2 denotes the coefficient of determination. Comparisons between the mean experimental data and the predicted result from mathematical models for stress-strain in longitudinal and circumferential directions are made in Figure. 5.1.5 (a) and (b), respectively.

Table.5.1.1 Modeling results of the elongation test on the gallbladder wall tissue

		Material Constants			R^2		RMSE	Time
No	c, Pa	a_1	a_2	a_4	Longitudinal	Circumferential		T, s
1	25.71	14.35	18.17	8.97	0.96	0.96	5.45	4.2
2	19.50	18.40	17.25	6.52	0.98	0.99	4.65	3.9
3	16.54	15.7	23.55	4.54	0.99	0.98	6.09	4.2
4	19.24	18.55	15.8	6.09	0.98	0.98	4.70	4.1
5	14.56	18.31	16.46	6.85	0.97	0.97	3.90	4.5
Mean	19.11	17.06	18.25	6.59	0.98	0.98	4.52	4.2
(SD)	3.77	1.72	2.77	1.43	0.01	0.01	0.83	

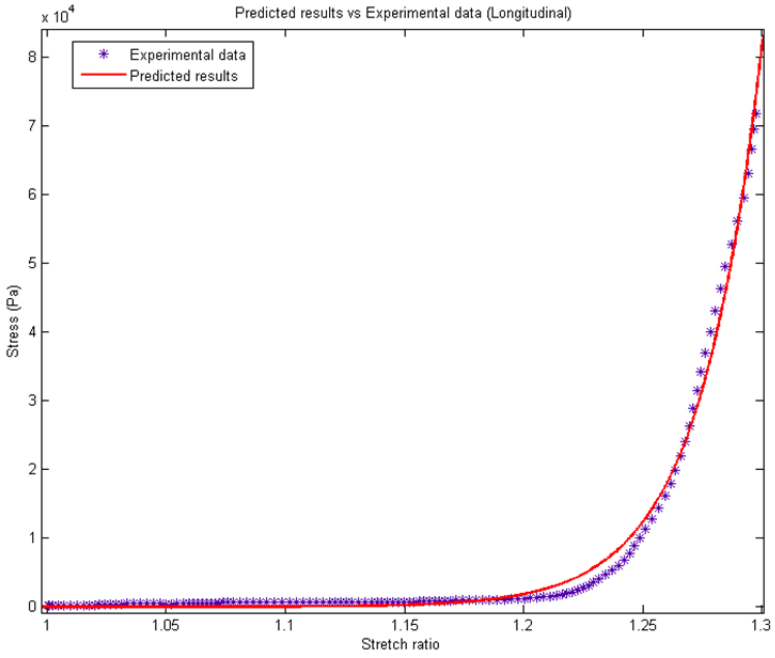

(a)

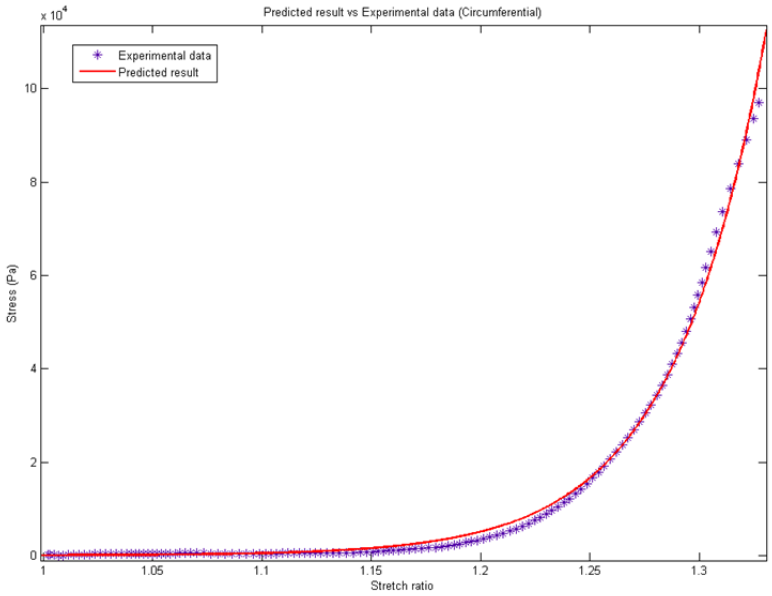

(b)

Figure.5.1.5 Mean experimental data (marked by *) and predicted result (solid line). (a) Longitudinal; (b) Circumferential directions

5.1.5 Gallbladder organ tissue modeling

Uniaxial indentation tests were carried out on the gallbladder bodies before they were cut into strips in both longitudinal and circumferential directions. The mean stress and standard deviation of the experimental results are shown in Figure.5.1.6. As is clear from the graph, the specimens are stiffer in longitudinal direction than in circumferential direction.

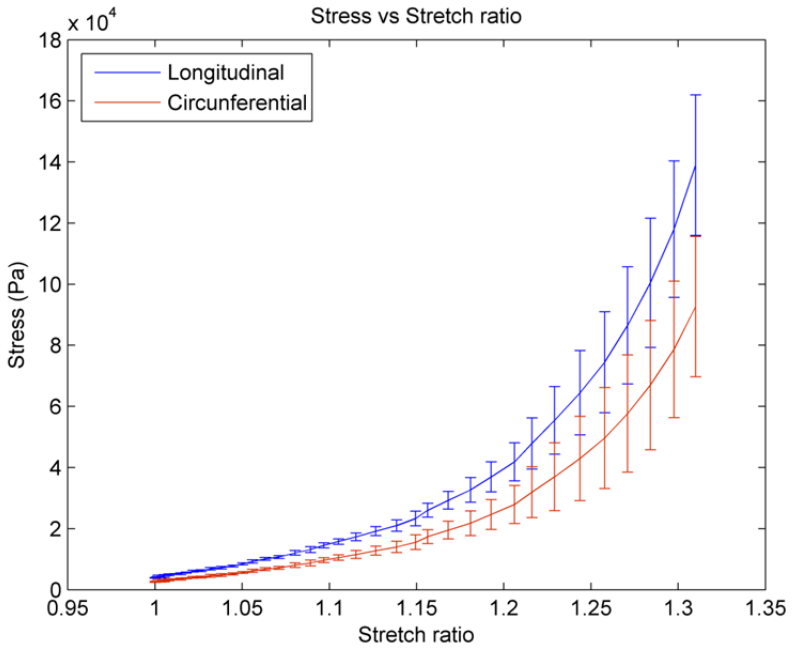

Figure.5.1.6 Experimental results of uniaxial indentation tests on gallbladder organ in longitudinal and circumferential directions. Solid line shows the mean stress of 5 specimens, vertical bar shows the standard deviation of stress

With the volumetric component embedded in the energy function, the engineering stress-strain model could be applied to fit the experimental data using GA. The second set of parameters for the uniaxial indentation test was determined as following:

$$p = \{c, a_1, a_2, a_4, t\} \text{ (P=5).} \qquad (5.1.22)$$

Five sets of GA-estimated results are shown in Table.5.1.2. The estimated parameters are similar to the parameters in previous section. The value of scale parameter t confirms the report in the literature that the value t=9 is suitable for nearly incompressible material [70]. Comparisons between the mean experimental data and predicted result from mathematical model for stress-strain in longitudinal and circumferential directions are made in Figure.5.1.7 (a) and (b), respectively. The predicted stress value is calculated using the mean value of material parameters. Based on the comparisons in the fitting figures and high values in the R square coefficients, we can conclude that the mathematical model is able to fit the experimental data closely.

Table.5.1.2 Modeling results of the indentation test on the gallbladder organ

		Material Constants				R^2		RMSE	Time
No	c, Pa	a_1	a_2	a_4	t	Longitudinal	Circumferential		T, s
1	20.34	19.85	15.32	7.18	8.33	0.95	0.96	5.56	7.1
2	18.70	16.52	16.57	6.98	9.26	0.97	0.97	4.60	6.9
3	17.32	16.83	19.43	5.87	8.67	0.96	0.96	5.34	6.8
4	18.49	15.58	16.75	6.59	9.18	0.97	0.96	4.60	7.0
5	16.75	17.26	17.6	7.1	9.2	0.97	0.96	4.49	6.9
Mean	18.32	17.21	17.13	6.74	8.93	0.96	0.96	4.83	6.9
(SD)	1.24	1.43	1.36	0.48	0.37	0.01	0.005	0.46	

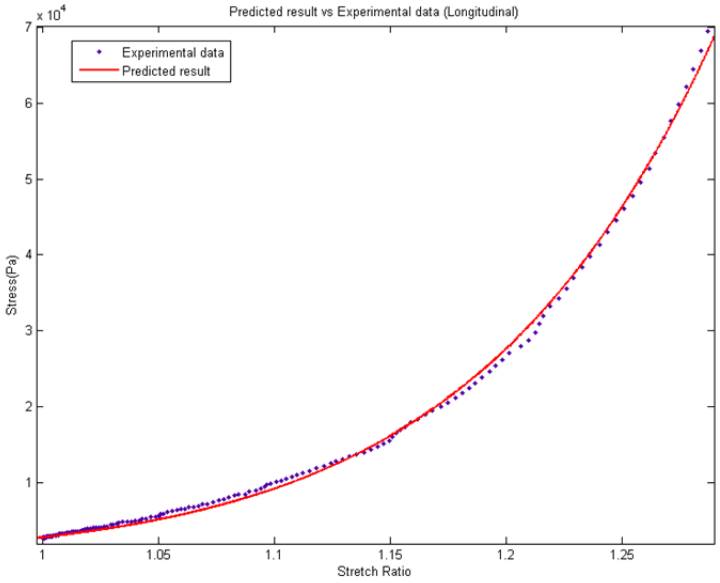

(a)

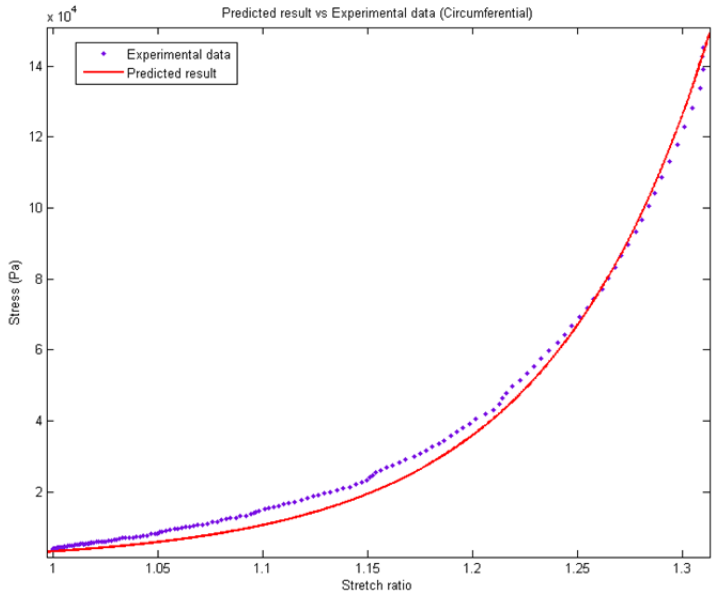

(b)

Figure.5.1.7 Mean experimental data (marked by purple point) and predicted result (red solid line). (a) Longitudinal direction; (b) Circumferential direction

From the predicted stress-strain relationship, it can be seen that variations exist but not very large. The proposed model can fit the experimental data closely which can be observed from the high value of the correlation coefficient. Both the longitudinal and circumferential data of gallbladder wall tissue strain-energy function can be fitted with mean R^2 equal to 0.98, mean RMS errors equal to 4.52% while the mean R^2 of gallbladder organ are 0.96 in both directions and mean RMS errors equals to 4.83%. We found no statistically significant differences between predicted and measured values in Table 5.1.1 and 5.1.2. The inclusion of the volumetric energy component in the gallbladder organ model requires an additional three seconds for solution to converge.

5.1.6 Applications

The gallbladder model was used for interactive deformation simulation and haptic rendering in a medical simulation system. Contours of the gallbladder were first extracted from slices of CT scans using active contour [35], to define the geometry of the gallbladder organ as shown in Figure.5.1.8. The

biomechanical gallbladder model was then reconstructed as shown in Figure.5.1.9.

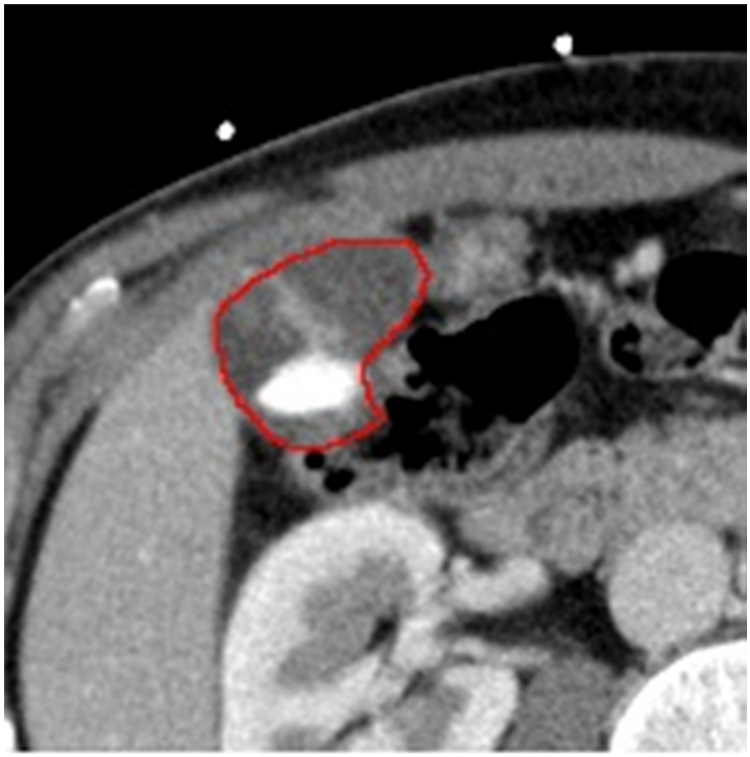

Figure.5.1.8 Segmented contour of gallbladder

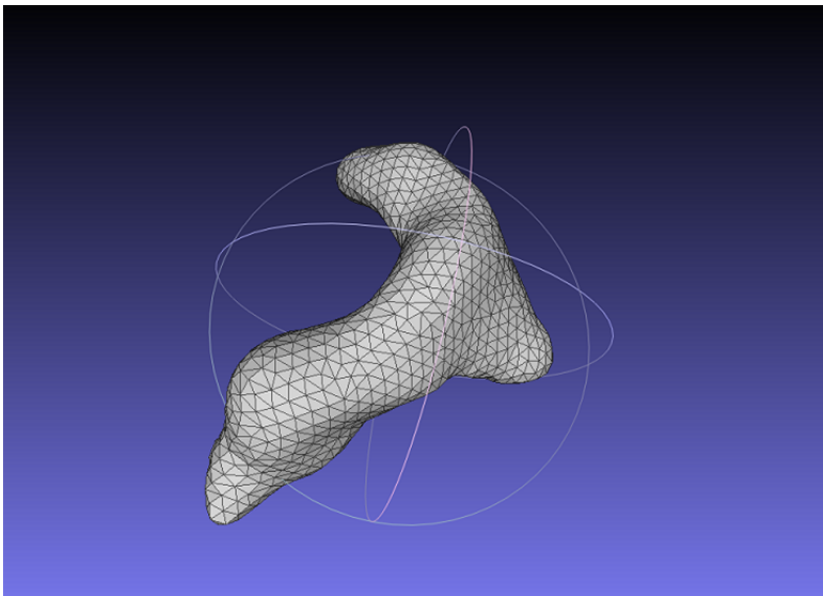

Figure.5.1.9 Constructed 3D gallbladder model

Figure.5.1.10 illustrates the deformation simulation and haptic rendering using the proposed gallbladder model. Haptic feedback during deformation of the

gallbladder organ is provided by the phantom desktop device (Phantom desktop, SensAble Technologies, Inc.). The stress-strain relationship derived for the gallbladder organ was utilized as pre-calculation data set in the calculation of feedback force. Displacement of the mass point on the tissue surface was first obtained from the tool-tissue interaction in the virtual environment, and then strain is calculated. After that, the feedback force from the tissue was calculated based on the derived stress-strain relationship. When the virtual surgical tool, manipulated by the user, contacted the virtual organ, the surface was deformed in real-time at 40~50 frames per second. Simultaneously, the Phantom device can render force feedback to the user at 1000 Hz. The system is therefore able to provide realistic interaction for the operator.

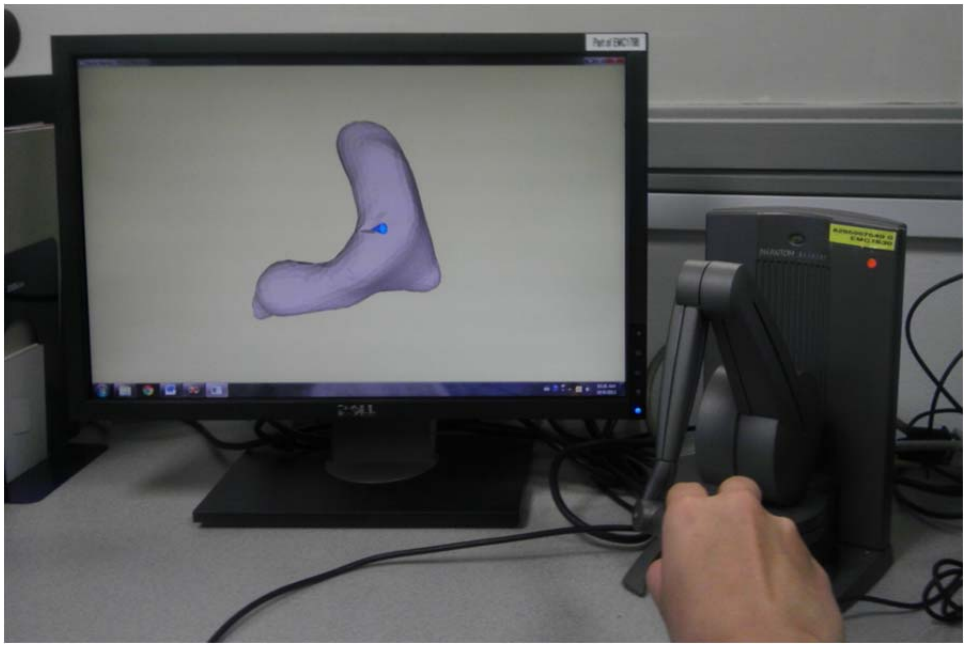

Figure.5.1.10 Interactive manipulation of gallbladder model using haptic interface device

5.1.7 Discussions and conclusions

In this study, the material constants for an exponential strain energy model were determined on the basis of the uniaxial mechanical test. It was demonstrated that the material constants of the gallbladder wall tissue are similar to the material constants of the gallbladder organ. The predicted stress-strain relationship based on the material constant fits closely to the experimental data. This finding validates the feasibility of the proposed model

and the reliability of the material constants for both gallbladder wall tissue and gallbladder organ.

Few studies focus on mechanical behavior of gallbladder tissue. Some studies concentrate on segmentation and 3D shape behavior of gallbladder [163, 164]. While these works can be used for applications for surgical scenarios selection and assistive diagnosis, they fail to provide a realistic deformable model which can simulate the nonlinear material behavior of gallbladder tissue. We have provided material constants of gallbladder wall tissue and gallbladder organ model that have been validated by experiments. There are studies that focus on haptic simulation of laparoscopic cholecystectomy using real-time deformable organ models. Haptic rendering of laparoscopic cholecystectomy presented in these works were based on deformable organ models using the mass-spring model. Although the deformable organ models are able to provide force feedback during virtual operation, they are not accurate enough to capture the nonlinear mechanical properties of gallbladder tissue. The exponential strain energy model implemented in this work is able to calculate the nonlinear deformation force, while providing a faster updating rate in transmitting the force to the haptic device.

Exponential stress strain relationship has been observed in biological tissues in vivo and in vitro [165-167]. The relationship is expedient for organs with reservoir function since low wall stiffness at physiological pressures facilitate wall stretch to accommodate the gall. The steep increase in wall stiffness with higher loads provides a mechanism to avoid overstretch and damage to the tissue. This is in agreement with a previous study which conducted a biomechanical behavior work on bile duct wall [168].

Both the gallbladder tissue and gallbladder organ demonstrate an anisotropic behavior with a larger capacity of stretching in longitudinal direction compared to circumferential direction. Other biological tissues such as arteries also show anisotropy and it was found that the elastic modulus in the circumferential direction was less than that in longitudinal direction [12, 169]. This anisotropic behavior would make the organ tissue elongate more than the increase in the diameter when under pressure. A stiff-walled organ in

circumferential direction would lower the wall stress but increase shear stress and resistance to flow. Elongation further contributes to higher shear stress and resistance to flow. Hence, during obstruction a pressure will build up faster resulting in inhibition of bile production.

Strain energy of gallbladder organ is decomposed into deviatoric and volumetric parts. The deviatoric part, which consists of an exponential strain energy function, accounts for the nonlinear material behavior, whereas the volumetric part, which is represented by a new function proposed in this work, accounts for material incompressibility. The advantage of such a method is that the deviatoric and volumetric parts can be treated as completely independent, which permits their decoupled treatment in the development of finite element analysis. A disadvantage of the decomposition is the increase in computational effort due to the product formula and the derivation stresses and elasticity tangent from the strain energy function, which takes about 3 more seconds for the solution to converge.

A systematic approach is used in this work for the identification of the material parameters. We first formulated an identification procedure based on genetic algorithms and demonstrated the flexibility and versatility of this method by calibrating parameters for gallbladder wall tissue and gallbladder organ under different loading conditions. The GA serves as an efficient method to solve the parameters identification problem with robust results. It contributes to reducing the computational time as it converges to around 80 iterations. The results presented confirm that such an approach has potential to accurately identify the parameters, without explicitly approximating a gradient search direction, which requires considerable computational time. The parameters calculated from GA show less variance and is more robust to local minima “traps.”

Future works will include the replacement of the exponential strain-energy function with the Chui combined energy function [11, 77]. In [11], a combined strain energy based constitutive equation for transversely isotropic biological material is proposed. The improved capability of this equation to model the experimental data compared to its previously disclosed isotropic version

suggests that anisotropic properties of liver tissue should be considered in surgical simulation.

This work provides a nonlinear variational model for the gallbladder tissue, which can be used for accurate deformation simulation and haptic rendering in surgical simulation. This soft tissue material model is implemented in a medical simulation system with haptic feedback. The gallbladder model is assigned with nonlinear hyperelastic properties. Haptic rendering utilizing the proposed model enables the user to feel the distinct force when the gallbladder is held or stretched. The nonlinear tissue model provides a highly realistic material model for advanced surgical simulation. Besides the gallbladder, this variational model is also applicable for simulation of other organs such as pancreas and stomach.

5.2 Haptic guidance for medical simulation

This section introduces the haptic guidance system that we are developing for medical simulation using variational minimization principles. Haptic emerged as effective interaction aid for improving the realism of virtual worlds, it has many applications in medical training, game entertainment, and education [94, 170, 171]. Haptic devices enable the user to interact with virtual/remote environment with force feedback, allowing him/her to feel the reaction forces generated when the virtual manipulated object interacts with the virtual environment [172].

Haptic devices can provide guidance force to train the user in the predefined virtual task, or to assist him in performing in a teleoperated remote mechanical system. The feedback force may constrain the user motions along a line or curve or over a given working plane or surface, helping the user to accomplish the virtual task[173].

In medical training, the master-apprentice tutelage model has been utilized effectively by the medical profession for centuries [174]. Training involves the exposure to errors, albeit under the guidance of an expert mentor. However, this leads to situations where the inexperienced surgeon performs an operation incorrectly, leading to largely avoidable patient discomfort and complications. The latter can prolong a patient's hospital stay or in the worst-case scenario can cause permanent damage or death.

Haptic guidance may provide a cost effective way for training of new surgeons [129, 175]. There are many studies in the literature which use haptic guidance to enhance training through constrained virtual path and feedback force guidance[176]. A remote diagnosis simulator was developed using a Phantom Desktop with a 3D surface model created from computed tomography data [177]. Based on Hertz's theory from contact mechanics, Chen et al. proposed an index finger palpation simulation of thigh tissue [178]. Chui et al. have developed a simulator for percutaneous vertebroplasty which is a minimally invasive procedure performed to bind spinal fracture components [179]. Integrated with a palpation interaction approach based on tissue dragging

algorithm, haptic palpation interaction for virtual reality-based medical simulator is developed [180]. The results of the study provide helpful insights for generic haptic interaction with rigid or deformable objects in virtual environments. However, there is no mentioning of a haptic guidance system that combines guidance and reaction forces.

There are patients who require tracheal reconstruction either for tracheal stenosis/malacia or following tumor extirpation. The purpose of tracheal reconstruction is to restore the patency of airways compromised by obstructing lesions or collapse of the tracheal wall[181]. We have been investigating new artificial implants for tracheal reconstruction. The reconstruction surgery is very challenging for the surgeons because of the limited operating space in the airway. In this study, a haptic guidance medical system is presented to simulate the incision procedure of tracheal reconstruction with the purpose of training new surgeons to perform the incision operation and investigating the feasibility of deploying our tracheal implants. Both haptic guidance and force feedback due to tissue interaction are included in the medical simulation system. We also describe an application on manipulation of a "Rubber Duck" to demonstrate its potential use in edutainment.

Our haptic guidance system consists of both guidance and reaction forces. The haptic guidance is rendered using a novel variational algorithm that generates the guidance force towards predefined path. A potential field is employed to model the potential energy around the path and a gradient descent is applied to solve the variational minimization problem. Following the minimization direction of the energy, the haptic force will constrain the object to move towards the lowest energy point which is located on the predefined path. This is integrated with the reaction force using a weighted function.

5.2.1 Haptic guidance for tracheal reconstruction simulation

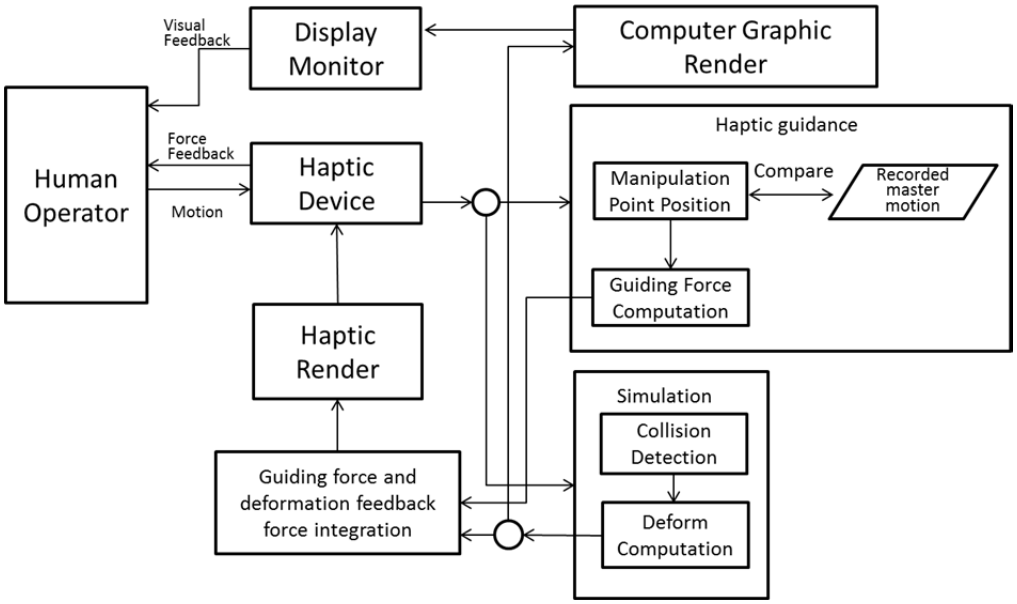

Figure.5.2.1 Overview of the haptic guidance and visual simulation system

The trachea serves as a specialized airway conduit between the larynx and bronchial tree. Up to half of the adult trachea (5–6 cm) can be resected and undergo primary anastomosis[182]. However, more than half of the tracheal length can be affected by disease. This condition could be arisen from extensive stenosis (either congenital or acquired), tracheomalacia, or neoplastic processes of the trachea or adjacent structures (thyroid, esophagus, larynx, or lung)[183]. A surgical solution is to cut off the affected segment on the tracheal and to stitch the healthy segments together.

Tracheal reconstruction is typically performed as an open surgery. During the surgery, the patient's neck will be "opened" and the tracheal exposed using a retractor. Resecting the diseased segments is complicated and requires good hand-eye coordination skill of the surgeon. Haptic guidance can be used to train the trainee surgeon in acquiring the necessary tissue resection technique.

In our medical simulation system, the motion of a master surgeon can be recorded. The motion path is reconstructed in our simulation system. It is used to guide the trainee surgeon in performing the resection of diseased tracheal segments. The haptic handle which is manipulated by the trainee surgeon can move freely within the constructed motion path, but would receive a force

when the manipulation point moves out of the desired motion path. The force which pushes the manipulation point back into the desired motion path is defined as guidance force. Figure.5.2.1 provides an overview of the augmentation of haptic guidance with force feedback from tissue-tool interaction.

We have included a force integration module in our simulation system. Haptic guiding force, *G* is generated when we start the simulation, and it will direct the manipulation point towards target point until the manipulation point reaches the predefined path. In addition to the guidance force, the trainee surgeon will also receive a force feedback, *R* from the interaction between the manipulation point and the virtual object. The virtual object is modeled as a mass-spring model. Details on the calculation of *R* can be found in[94].

F which is experienced by the user is defined as the weighted sum of the combined guidance force *G* and reaction force *R*:

$$F = w_1 \cdot G + w_2 \cdot R, \tag{5.2.1}$$

$$w_1 + w_2 = 1, \tag{5.2.2}$$

where w_1 and w_2 are the weighted coefficients for guidance force and reaction force. We have investigated three modes for the force integration module.

1). When $w_1 = 1, w_2 = 0$, the trainee will only receive the guidance force in order to learn the operation skills quickly.

2).When $w_1 = w_2 = 0.5$, in this equal guidance and reaction force mode, the trainee surgeon can improve their operation skills under the help of haptic guidance and feel the deformation feedback force of virtual object.

3). When $w_1 = 0, w_2 = 1$, this mode provides a non-guidance virtual reality environment for the trainee surgeon to test their operation skills.

5.2.2 Potential field modeling of haptic guidance force

The haptic guidance force is developed based on artificial potential field. Each point in the virtual environment around the predefined path is assigned with a storing energy, where the target point on the path possesses the lowest energy. The storing potential energy is calculated as:

$$U(q) = \frac{1}{2}\xi d^2(q, q_{goal}), \tag{5.2.3}$$

where q denotes the manipulation point and q_{goal} denotes the position of target point, ξ is the spring coefficient which determines potential energy density.

The distance between the manipulation point and target point is calculated as following:

$$d(q, q_{goal}) = \sqrt{(x - x_{goal})^2 + (y - y_{goal})^2 + (z - z_{goal})^2}, \tag{5.2.4}$$

where the *(x, y, z)* and *(x_{goal}, y_{goal}, z_{goal})* are the coordinates of the manipulation and target points, respectively.

An incremental potential field is utilized in the haptic guidance system. The potential energy distribution is divided into three energy intensity stages (ξ=3, 6, 9) with a decreasing order as the manipulation point getting closer to the virtual object. Three stages of energy distribution at different Z values are shown in Figure.5.2.2.

The guiding force will follow the descent direction of the potential energy and lead the manipulation point to the lowest energy position, which is the target point, calculated as follows:

$$\begin{aligned} F(q) &= -\nabla U(q) = -\nabla(\frac{1}{2}\xi d^2(q, q_{goal})) \\ &= -\frac{1}{2}\xi \nabla d^2(q, q_{goal}) = -\xi(q - q_{goal}) \end{aligned}. \tag{5.2.5}$$

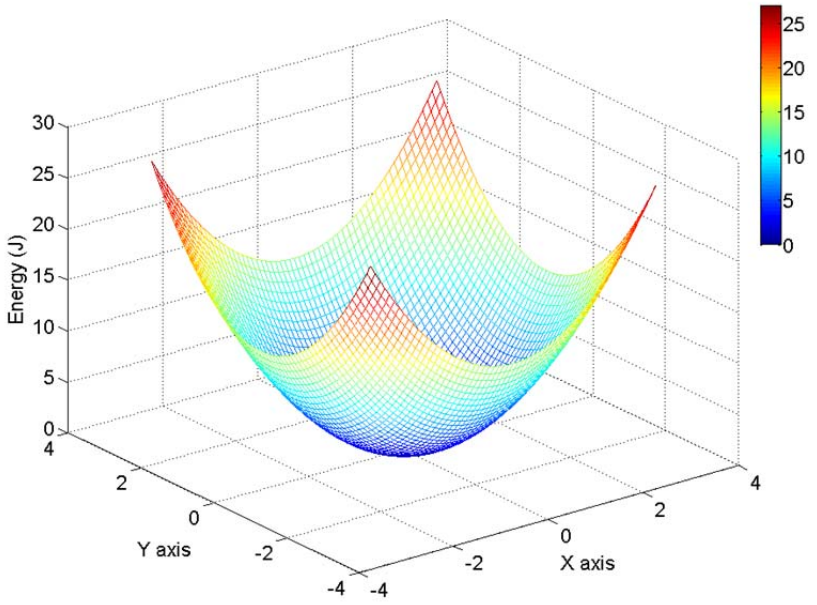
Energy (J)
30
25
20
15
10
5
0
4
2
0
-2
-4
Y axis
-4
-2
0
2
4
X axis
25
20
15
10
5
0

(a)

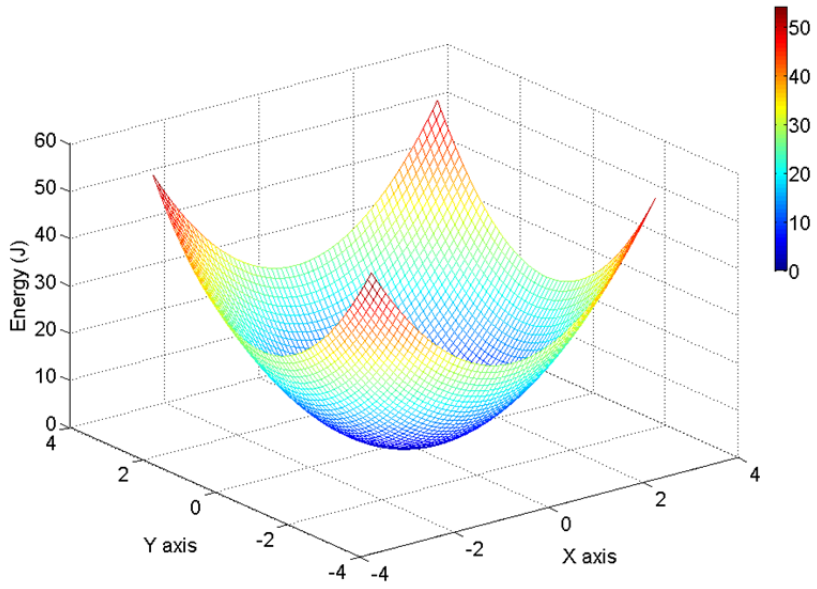
Energy (J)
60
50
40
30
20
10
0
4
2
0
-2
-4
Y axis
-4
-2
0
2
4
X axis
50
40
30
20
10
0

(b)

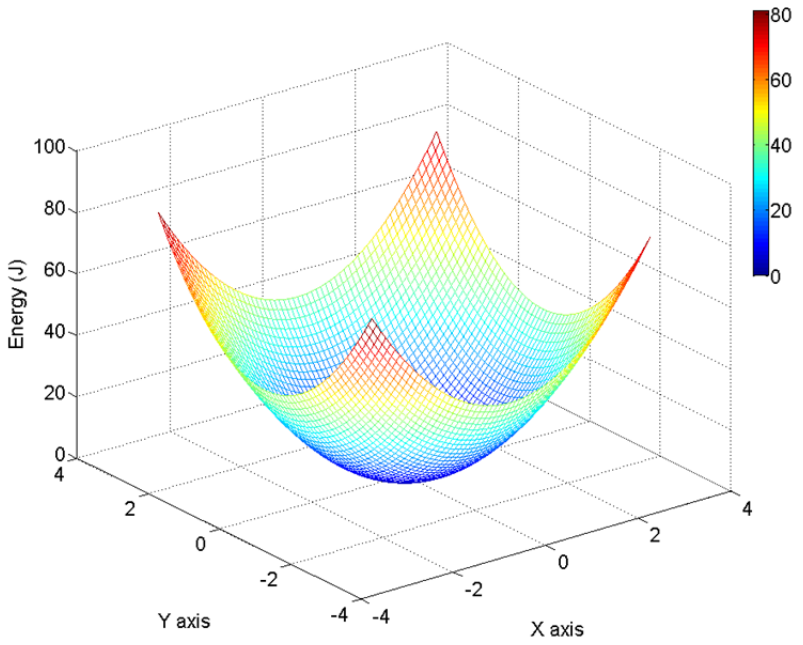

(c)

Figure.5.2.2 Three stages of potential energy (J) distribution around the predefined path: (a) ξ =3; (b) ξ=6; (c) ξ=9

Plain view of the guiding force towards the target point at a fixed value on Z axis is presented in Figure.5.2.3.

Following the gradient descent method, the energy is minimized by the negative gradient of the potential energy function, and the new position of the manipulation point is updated as following:

$$x_{new} = x_{old} - \alpha \cdot \nabla_x , \tag{5.2.6}$$

$$y_{new} = y_{old} - \alpha \cdot \nabla_y , \tag{5.2.7}$$

$$U_{new}(q_{new}) = \frac{1}{2}\xi d^2(q_{new}, q_{goal}) , \tag{5.2.8}$$

where α is a step coefficient which will determine the convergence steps; (x_{new}, y_{new}) and (x_{old}, y_{old}) denote the respective new and old positions of the manipulation point.

The solution to the iterative gradient descent would determine a minimal for the energy functional by traversing in the direction of the negative gradient, $-\nabla U(q)$ of the net energy functional that is to be minimized.

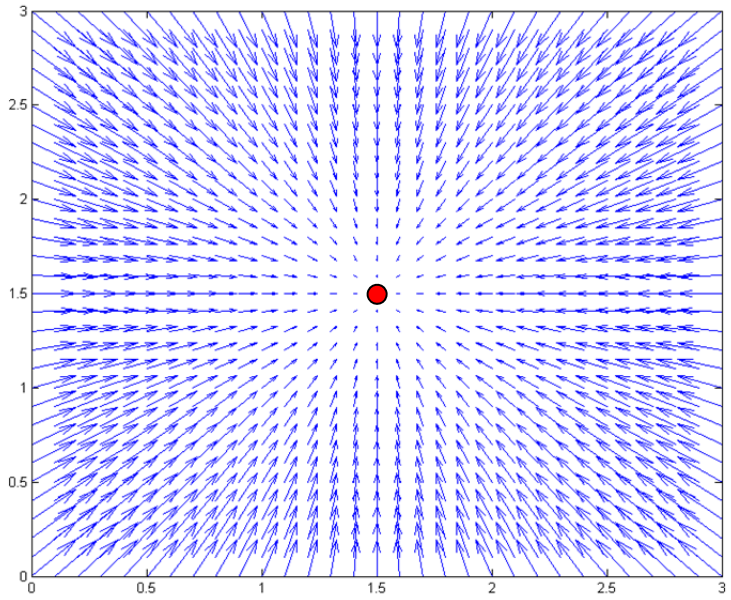

Figure.5.2.3 Potential field map at a fixed Z value around the path

5.2.3 Haptic rendering algorithm

We first determine the target point on the predefined path with the nearest distance to the manipulation point. The predefined path is extracted from the master surgeon's recorded path. The potential energy of the manipulation point is then obtained using Eq. (5.2.3). The guidance force, which directs the manipulation point towards target point, is determined by gradient descent with Eq. (5.2.5). The algorithm is carried out iteratively until the manipulation point reaches the lowest energy point on the potential energy map. Figure.5.2.4 is the flow chart which illustrates the algorithm.

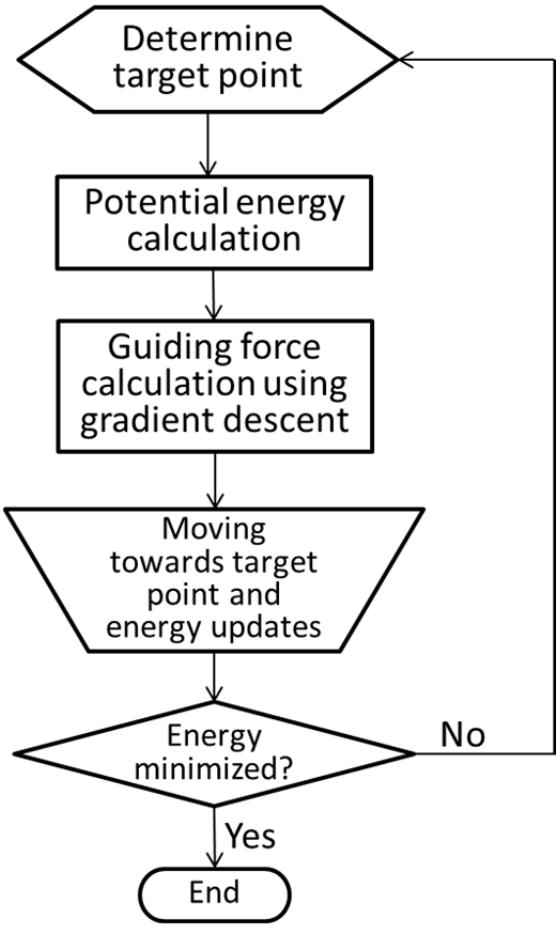

Figure.5.2.4 Flow chart of the algorithm

5.2.4 Haptic rendering results

The haptic guidance system is implemented on a PHANTOM desktop force feedback device with an update frequency of 1000Hz. It is implemented based on the open-source library Chai3D [184]and our proposed algorithm.

For tracheal reconstruction simulation (Figure.5.2.6 (a)), we have simulated the incision process on the trachea, which is accomplished by moving the cursor along the predefined path on the 3D tracheal model. The 3D tracheal model is obtained from CT scans of porcine tracheal as shown in Figure.5.2.5.

The guidance path is a white dash line as shown in Figure.5.2.6 (b) and Figure.5.2.6 (c). User will receive a guiding force when the ball is moving out of the path and pull the cursor back to the path, as shown by the red arrows in Figure.5.2.6 (b). In contrast, the user can move the cursor freely along the predefined path to finish the cutting task (Figure.5.2.6 (c)). The tool-tissue

interaction simulation is included when the tracheal body deforms due to a collision between the cursor and tracheal body. The three modes of force integration are available in the tracheal reconstruction simulation system.

Figure.5.2.5 3D tracheal model from CT scans; 3D tracheal model reconstructed from CT scans, a physical based model is generated from the model for virtual interaction

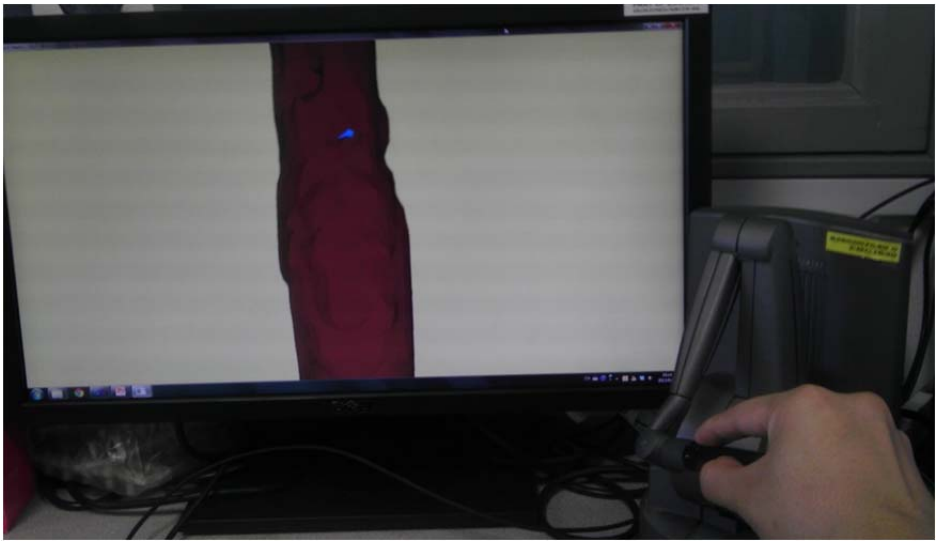

(a)

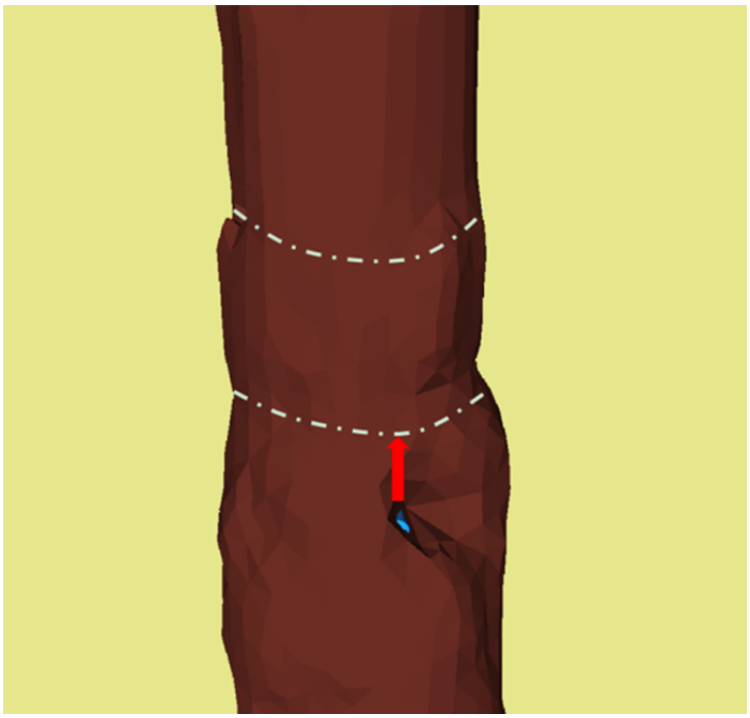

(b)

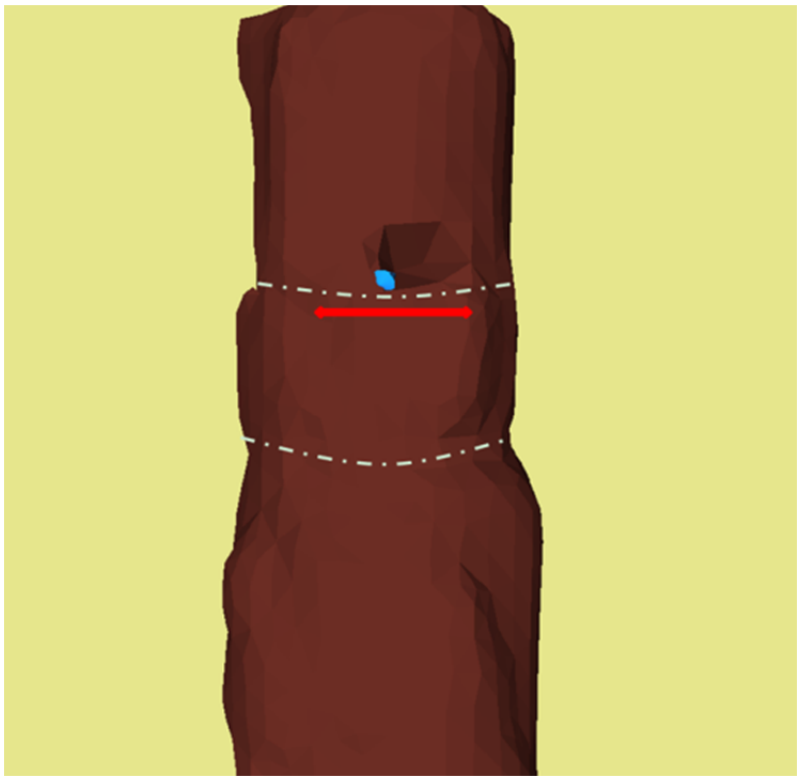

(c)

Figure.5.2.6 Haptic simulation of tracheal reconstruction. (a) Image of the simulation system;(b) and (c) Simulation images

5.2.5 Discussions and conclusions

A haptic guidance system is presented in this work, which can assist a user to finish a virtual task, or the system can be further developed into more complicated medical training system [173]. In the haptic guidance system, the operation paths are constrained by the guidance force with a predefined curve. An incremental potential field is employed to model the storing energy within virtual environment. A gradient descent method is utilized to determine the value and direction of guidance force.

As the potential field can obtain a global representation of the workspace [185], a continuous potential field gives a good indication of the distances to the target position so that necessary changes in following movements and orientation can be done in a smooth and continuous manner. When detecting collisions, combinatorial complexity of intersection detection performed with geometric representations is avoided. This is accomplished by eliminating the need for explicitly performing intersection detection through the use of a potential field that gives object distance information.

In order to solve the variational energy minimization problem, the steepest gradient descent method is employed since it can determine the following movement directly and efficiently. However, the gradient descent method is not applicable in cases when there are many obstacles in the space as it may encounter the local minima problem. During the simulation process, the haptic guiding force will always exist unless the manipulation point is on the predefined path. The feedback force due to collision of the virtual object can exist simultaneously. The priority of these two forces in rendering needs further consideration. More attention will be paid to these problems in our future research.

Besides the application of tracheal reconstruction surgery, we have also experiment the algorithm on another application with “Rubber Duck” (Figure.5.2.7 (a)). The cursor, which is represented with a grey ball, is constrained to move within the folded white line (Figure.5.2.7 (b)), and a resistance force will received when the ball is moving out of the path

(Figure.5.2.7 (c-d)). The duck will interact also with the manipulation ball in the virtual environment, as shown in Figure.5.2.7 (d).

This work describes our novice rendering method of haptic guidance in physics-based virtual reality simulation. There are few works on combining haptic guidance and force feedback in the literature. We demonstrated that haptic guidance can benefit human performance during virtual manipulations. In addition to its application on simulation based medical device design [186], the method may improve the effectiveness and realism of medical training. Further experiments will be required to investigate the effectiveness of this training method with both guidance and reaction forces rendered.

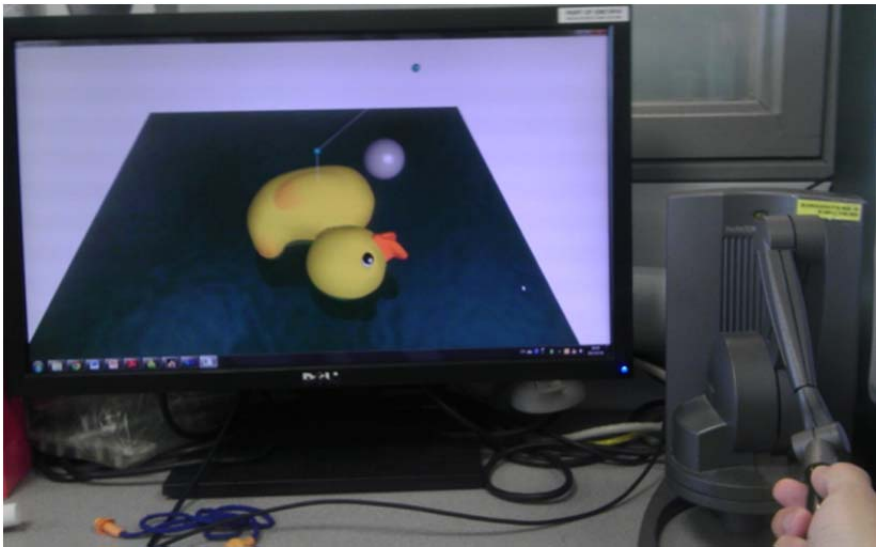

(a)

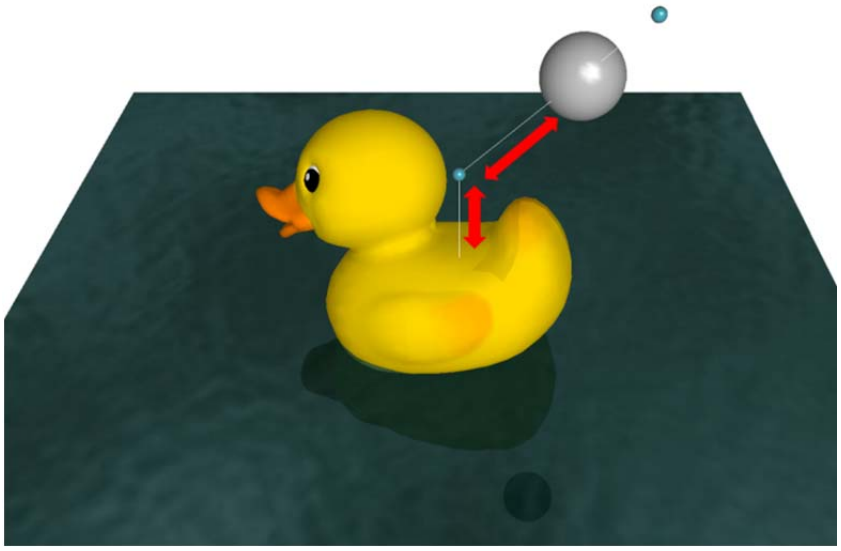

(b)

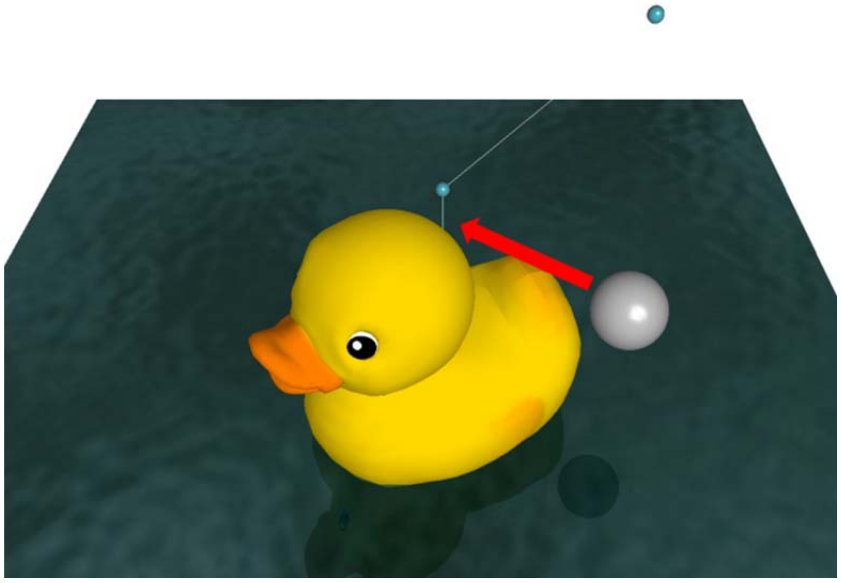

(c)

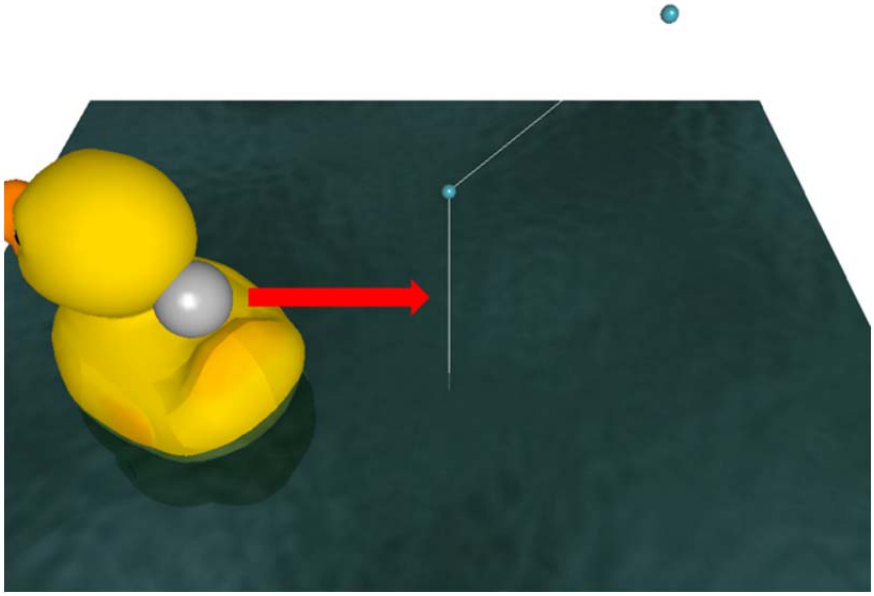

(d)

Figure.5.2.7 Haptic guidance application of “rubber duck”: (a) Overview of the application; (b) Manipulation point on the predefined path; (c) and (d) Manipulation point is out of the predefined path

Chapter 6 Modeling and Simulating Bioresorbable Material Degradation Process

In this chapter, the variational methods are applied to simulate the degradation process of bioresorbable materials which are utilized in laryngeal micro-surgery. Voice disorders seem to be the most common communication disorder across the lifespan [187]. Voice microsurgery (Laryngeal microsurgery) serves as an appropriate approach to treat the voice disorder problem. The challenge of voice surgery treatment lies in modulating wound healing process or managing tissue that has undergone reparative processes after surgery. This is due to restrictions imposed by the microsurgical instruments, reduced force feedback and loss of stereopsis. The surgeon has to be highly skilled to perform wound closure operation, and it is time consuming [188, 189]. In order to produce good wound healing result as well as reduce the operation time, surgical wound closure techniques have evolved from the earliest development of suturing materials to comprise resources that include synthetic sutures, biodegradable tapes, and adhesive compounds.

The surgical clip is an emerging type of wound closure device, and is a viable alternative to sutures. Suturing is difficult especially for microsurgery which is highly skill dependent. Surgical clip is a clinical viable alternative wound closure device to sutures or other wound closure devices such as adhesive glue. We have measured the duration for suturing during our animal experiments. A senior surgeon may require a few minutes to close a wound on the voice box using sutures but it may take up to 20 minutes for a less experience surgeon to complete the same suturing task. The task can be completed using our micro-clips in a few minutes regardless of the skill level of the surgeons [190, 191]. A surgical clip may provide excellent healing results, and can be easily exerted onto wound since it can be made to extremely small size and is able to withstand high vibration frequencies and shearing stresses during phonation. Some materials such as stainless steel, titanium and tantalum have been used for surgical clips following other difficult surgical dissections, such as ligating the cystic duct and artery in laparoscopic cholecystectomy [192]. Limitations of these devices include significant foreign body reaction, poor holding

strength and significant interference with roentgen logic studies like CT and MRI [193-195]. To address these limitations, use of bioresorbable materials in the design of implantable medical devices has been proposed. For instance, ligating clips manufactured from polydioxanone used in laparoscopic cholecystectomy can be completely absorbed in the process of ester bond hydrolysis over a period of 180 days [193].

Magnesium based micro-clips used in wound closure in laryngeal microsurgery involving vocal cord covers have been studied in previous works [190, 191, 196]. The clips would be completely degraded and absorbed after several weeks. The degradation of magnesium will have no influence on the properties of the connected tissue as magnesium metabolism of a living subject is dependent on the introduction of the magnesium [197]. Natural, oral administration of magnesium via, for instance food, essentially results in an intracellular enrichment of magnesium ions. Introducing magnesium implants into the tissue will lead to different decomposition behaviour. Magnesium in the artificial body electrolytes mainly produces magnesium hydroxide, magnesium oxide, and magnesium chloride. Due to the physiological metabolic processes, the organism will succeed in either excreting the above mentioned products or integrating them into the natural metabolic process. However, it is difficult to predict degradation in ex vivo experimental set-ups due to complexities in mimicking the complex internal environment of the human body [196]. Studies on mechanical properties during material degradation indicate that degradation may affect the structural integrity of the device [198, 199]. In this study, a numerical approach to model and simulate material degradation of a bioresorbable wound closure device for laryngeal microsurgery is proposed. It is important for the bioresorbable materials to be sufficiently strong to enhance wound healing when the wound is vulnerable, and maintain wound closure until the wound is completely healed. The numerical method can simulate the degradation process and serve as reference for strengthen the particular parts on the clips in order to maintain the structure mechanical integrity. The numerical method described in this work is also applicable to other application of small bioresorbable wound closure devices.

Section 6.1 describes related work in the field of computational modeling of bioresorable materials, and the novel modeling methodology and implementation is presented in Section 6.2. Sections 6.3 and 6.4 describe the results of our investigation and present a detailed discussion of the results respectively. This chapter is concluded in Section 6.5.

6.1 Related work in biodegradable materials

Biodegradable devices are able to perform a specified function within a certain time period and absorbed by the body gradually. Considering the healing time for wound varies among different kinds of tissues[200], and the biodegradable devices are needed to maintain stability until wound heals to a certain degree [201]. Degradation/corrosion mechanism of the biodegradable materials which can be used as reference for the design procedure of biodegradable device has received a lot of research interest. Many works had been devoted to study the corrosion mechanism of Mg alloy as a biodegradable material. Controlling of the degradation rate is an important develop direction for Mg alloy biodegradable devices [202]. Degradation measurements had been conducted in-vivo and in-vitro by Witte [203]. Influences of environmental conditions on degradation process of magnesium alloy were also studied [204, 205]. Studies showed that the rate of degradation depends on a variety of factors, including alloy composition [206], surface treatments and coatings [207], solution composition [208], solution transport conditions [209] and so on. Further studies also reported that mechanical loading, both static [210] and dynamic [211] may contribute to the degrade behavior of Mg alloy biodegradable devices. However, literature on degradation modeling of magnesium alloys in laryngeal environment is limited.

Physically simulating degradation in-vitro and in-vivo is constrained by difficulties mimicking and controlling the environment to which the clips are subjected; their minute size also makes in-vivo testing difficult. The degradation of clips is affected by many factors, such as stress, strain, pH, solute/solvent concentration and temperature.

Mathematical modeling of the degradation process provides useful insights into the degradation mechanism, since in-vivo and ex-vivo experiments are difficult to distinguish the effects of different factors. Liu and Schlesigner [212] proposed a mathematical model to deal with microgalvanic corrosion of magnesium alloy while Deshpande presented another model using the Arbitrary-Lagrangian-Eulerian(ALE) method accounting for microgalvanic activity within binary phase metal alloy [213]. Stress corrosion cracking mechanism of Mg alloy was studied by Dietzel with a mesoscale fiber bundle model [214]. Microscale models of corrosion based on diffusion-controlled processes also can be found in literature [215]. Computer based methods like finite element (FE) had been used to model and investigate mechanical properties for stents under different conditions: expansion[216, 217], flexibility [218, 219], fatigue [220, 221] and interaction with tissues [222]. Nevertheless, few studies pay attention to the degradation mechanism of biodegradation clips which has important use in wound closure application. This study discusses the strain effect on the degradation rate of biodegradable clip which is one of the major factors influencing the degradation process[223, 224]. The simulated degradation map can provide useful information on how to improve the structure integrity.

Degradation of bioresorbable material in this work is modeled as a strain energy minimization problem based on active contour. The energy minimization problem is solved using an incremental FE method [225]. The incremental FE method seeks to minimize the energy function so as to determine the stable energy state and corresponding device shape. The degradation rate is computed from a function that relates the properties of biodegradable materials with strain energy. In-vitro and in-vivo experiments have been conducted to validate the model as well as to evaluate the degradation properties of the device.

6.2 Modeling of the degradation process

Degradation starts from deployment of the micro-clips onto tissue and ends when the clips reach their minimum energy state (approximating zero in the stable state) known as the stable energy state. Integrative active contour [35]

and incremental FE method is implemented to solve this energy minimization problem. The modeling process consists of three steps. The first step is performed by using parametric active contour method and beam bending [226] to model the energy on each element. The active contour model is one such method that has wide applications in deformable object modeling [227]. The second step utilizes incremental FE method to solve energy minimization problem so as to find the stable energy state of the clip. Finally, the degradation process is simulated by transferring the intermediate energy obtained from the calculation process to degradation displacement in each element. The work process of this study is illustrated in Figure.6.1.

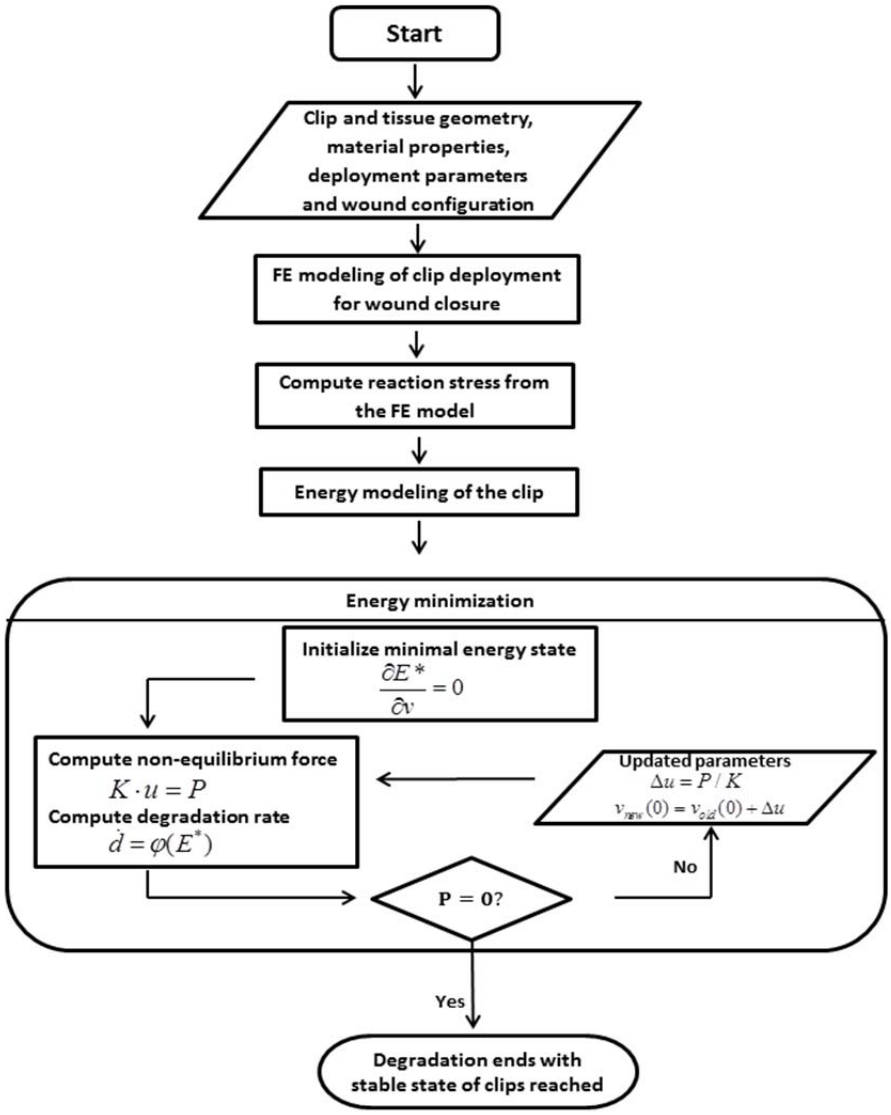

Figure.6.1 Work flow of the study

6.2.1 FE modeling of the tool-tissue interaction

A finite element (FE) model was created to simulate the interaction between the micro-clip and tissue in order to obtain the reaction stress of the clip elements in the balance state after deployment of clip into tissue. The clip was modeled as a FE structure with an assumed nonlinear material model of Young's modulus (45GPa), Yield strength (80-100MPa) and Poisson's ratio (0.35). The porcine tissue in this simulation was treated as a hyperelastic material while the model parameters were obtained from previous studies [228, 229]. The geometry of the tissue model is a square cuboid with an incision which simulates the wound on top face of the body. The size of the cuboid is $30 \times 30 \times 30$ mm with all its sides fixed. The clip is exerted onto the incision face and penetrates into the tissue until the wound is closed as shown in Figure.6.2.

The force on each element of the clip obtained from this study can serve as input data in the computation algorithm for degradation simulation. The FE simulation was performed using ABAQUS which is a commercial FE software. Figure.6.2 illustrates the simulation of deformation of the clip.

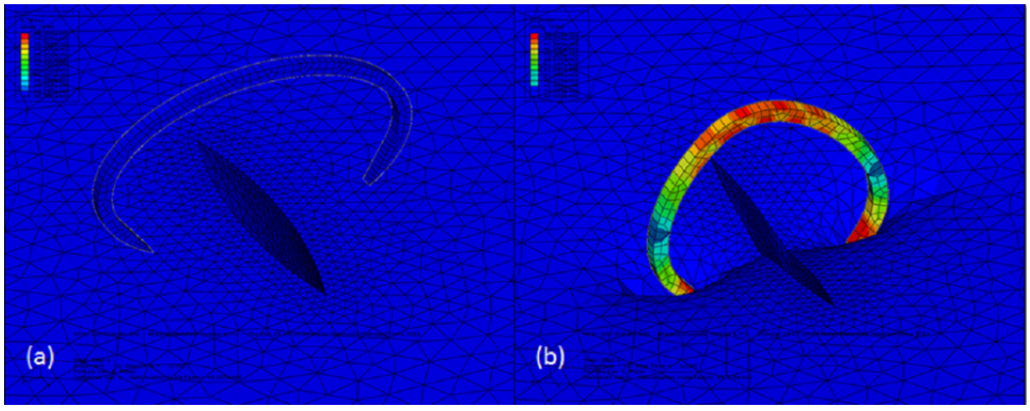

Figure.6.2 Computer simulation of clip-tissue interaction using ABAQUS: (a) Image before deformation; (b) Image after deployment of clip into tissue

Reaction force on each element can be calculated from the stress. The areas in which the clip experience maximum force were identified to be in the middle of the clip and at the two sections of its legs where the clip was in contact with

tissue. These three areas possibly experienced maximum strain during deformation. Typical deformation for the clips is about 1mm.

6.2.2 Energy modeling

The clip is made of magnesium. Loading conditions and material properties may affect the degradation process, and they are required to be considered in the energy modeling section. The total energy of the clip during degradation is modeled as following:

$$E^* = E_m + E_{ext}, \tag{6.1}$$

where E_m denotes the energy of magnesium, and E_{ext} is the work done by the external force.

The clip is divided into *N* beam elements (*N* is the number of elements in FE simulation). The centroids of all elements can be represented as an elastic curve *C(s)=(x(s),y(s),z(s))* parameterized by $s \in [0,1], s=x/L$, *L* denotes the length of the beam element. Assuming that each element is fixed at two ends, elastic displacement in x direction under external force is given as

$$d_x(s) = \frac{Fx}{12EI}\left(\frac{3L^2}{4} - x^2\right), \tag{6.2}$$

where d_x indicates displacement in *x* direction; *F* denotes the external force or reaction force on each element which is normal to the element surface, it is obtained from the previous section on FE modeling; *E* is the Young's modulus of clip; *I* and *L* are the moment of inertia and length of the beam element, respectively. This is applied similarly for the *y* and *z* components of the displacement vector in case that the clip elements are under pressure. At this step, *C(s)* is a straight line connecting the points *C(s=0)* and *C(s=1)*. Active contour model [35] is applied model the physical energy of magnesium as following:

$$E_m = \sum_i^N \left(\alpha \left|\frac{\partial d_i(s)}{\partial s}\right|^2 + \beta \left|\frac{\partial^2 d_i(s)}{\partial s^2}\right|^2\right), \tag{6.3}$$

where i and N denote the element number and total number of elements within the clip. The first term in Eq. (6.3) represents elasticity while the second term represents rigidity [35]. α and β are scalar coefficients for stretching and bending respectively.

The work done by external force is described as:

$$E_{ext} = -\sum_{i=1}^{N} F_i \cdot v_i \,, \tag{6.4}$$

F_i and v_i are external force and displacement of element i, respectively.

Substituting Eq. (6.3) and (6.4) into (6.1), the energy is formulated as following:

$$E^* = \sum_{i}^{N} (\int_0^1 (\alpha \left| \frac{\partial d_i(s)}{\partial s} \right|^2 + \beta \left| \frac{\partial^2 d_i(s)}{\partial s^2} \right|^2) ds) - \sum_{i=1}^{N} F_i \cdot v_i \,. \tag{6.5}$$

Based on the element force calculated from previous FE modeling, energy distribution computed from Eq.(6.5) is displayed in Figure.6.3 and is depicted from highest (red) to lowest (blue). As shown in Figure.6.3, three separate sections of the clip possess a relatively higher physical energy. The largest deformation occurs at the top section of the clip and results in the largest inner stress. In order to maintain equilibrium, the contact areas at the left and right legs of the micro-clip experience two reaction forces from the tissue in contact. These three areas possess a relatively higher load and hence higher physical energy.

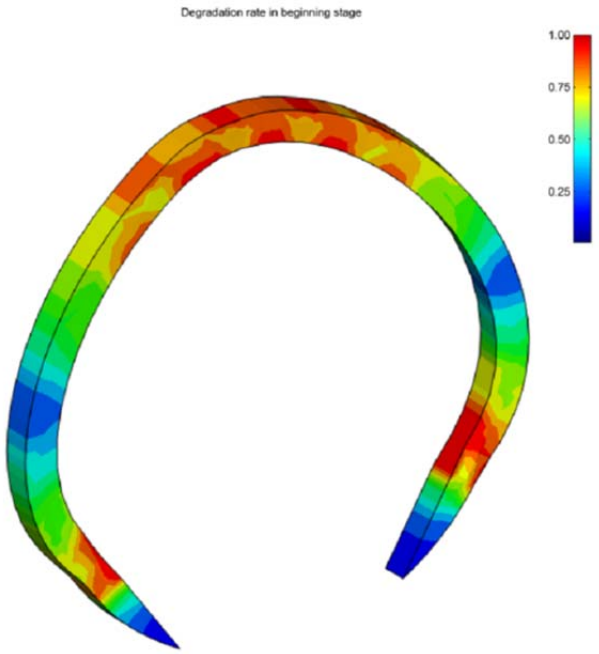

Figure.6.3 Energy distribution on clip at initial deployment before degradation, energy is indicated from highest (red) to lowest (blue)

6.2.3 Energy minimization and stable energy state

When total energy of the clip E^* is minimized, the system will reach a local minimum associated with a contour of the clip shape, and degradation ceases to evolve until the force on the clip is changed. For a system with N nodes, the total energy is shown in Eq. (6.5), and position of all nodes is represented by $v = (x, y) = [(x_1, y_1,), (x_2, y_2),(x_3,y_3)\ldots(x_N, y_N)]$.

The state of minimal energy min E^* corresponds to

$$\frac{\partial E^*}{\partial v} = 0\,. \tag{6.6}$$

Apply Taylor expansion of E^* around an initial guess $v(0)= (x(0), y(0)) = [(x_1(0), y_1(0)), (x_2(0), y_2(0)),(x_3(0),y_3(0))\ldots(x_N(0),y_N(0))]^T$ of the equilibrium state gives

$$E^* \approx E^*(v(0)) + \left.\frac{\partial E^*}{\partial v}\right|_{v=v(0)} \bullet (v - v(0)) + \frac{1}{2}(v - v(0))^T \bullet \left.\frac{\partial^2 E^*}{\partial v \partial v}\right|_{v=v(0)} \bullet (v - v(0))\,. \tag{6.7}$$

Substitute Eq. (6.7) into Eq. (6.6) yields the following governing equation of the element displacement u,

$$K \cdot u = P \,, \tag{6.8}$$

where

$$K = \left. \frac{\partial^2 E^*}{\partial v \partial v} \right|_{v=v(0)} = \left. \frac{\partial^2 E_m}{\partial v \partial v} \right|_{v=v(0)} \,, \tag{6.9}$$

$$P = -\left. \frac{\partial E^*}{\partial v} \right|_{v=v(0)} = F - \left. \frac{\partial E_m}{\partial v} \right|_{v=v(0)} \,. \tag{6.10}$$

K denotes the stiffness and P denotes the non-equilibrium force of the clip element. For the clip, Eq. (6.8) must be solved iteratively until P reaches zero, $P=0$, which represents the absence of non-equilibrium force that will drive the element to move. During each iteration step, the state variables are updated via

$$\Delta u = P / K \,, \tag{6.11}$$

$$v_{new}(i+1) = v_{old}(i) + \Delta u \,. \tag{6.12}$$

For minimization problems, FE model will converge and will achieve stability if the total energy E^* decreases during every iteration step. Since the non-equilibrium force $P = -\left. \frac{\partial E^*}{\partial v} \right|_{v=v_{new}(0)}$ represents the steepest descent direction of total energy E^*, the stability and convergence are ensured if

$$P \cdot u > 0 \,, \tag{6.13}$$

where u is the displacement increment. A sufficient condition for Eq. (6.13) is that the stiffness matrix K is positive definite.

After applying the above algorithm, each element will reach its minimum energy, which results in the stable energy state of the whole clip.

6.2.4 Simulating clip degradation

The material property of a biodegradable material changes during the degradation process. α and β which used to control the elasticity and rigidity of the material also vary as the degradation proceeds:

$$\alpha = \alpha_0(1-d), \tag{6.14}$$

$$\beta = \beta_0(1-d), \tag{6.15}$$

where d represents the 3D spatially and time dependent degradation field [230]. We assume $d=0$ for a virgin material while $d=1$ for a completely degraded material. These reaction equations would take place along the degradation and updated in the energy minimization procedure.

Degradation process is simulated by integrating degradation rate calculated from intermediate energy of each element during the computational procedure. A new function which relates the strain energy and degradation rate is proposed in this work to calculate the degradation of each element. In the case of uni-axial extension, degradation rate $\dot{d}$ of each element is calculated by mathematical transformation function $\varphi(E^*)$:

$$\dot{d}_i = \varphi_i(E_i^*) = \tau_D^{-1} \cdot (1-d(t)) \cdot (E_i^*)^{1/2}, \tag{6.16}$$

where τ_D is a characteristic time scale of degradation, i denotes the element number of clip.

By taking Laplace transforms on Eq. (6.16), mass loss of the degradable clips based on time can be deduced as following:

$$d = \frac{(E^*)^{1/2}}{\tau_D} \cdot e^{-\frac{(E^*)^{1/2}}{\tau_D} \cdot t}. \tag{6.17}$$

In calibrating the degradation model, the value of model parameter τ_D is determined based on the in-vitro immersion experimental results.

6.3 Experiments set up

6.3.1 In-vivo experiments

In-vivo experiments were carried out using micro-laryngeal surgery on porcine models [191] (IACUC Protocol No.045/08). An epithelial flap was created on each vocal fold and 3-5 clips per vocal fold were applied to close the wound (Figure.6.4). The clips were exerted onto the wound part with two ends penetrating into the tissue and clamped into a round shape for wound closure. After four weeks, the vocal fold was excised for clip degradation assessment as seen in Figure.6.5.

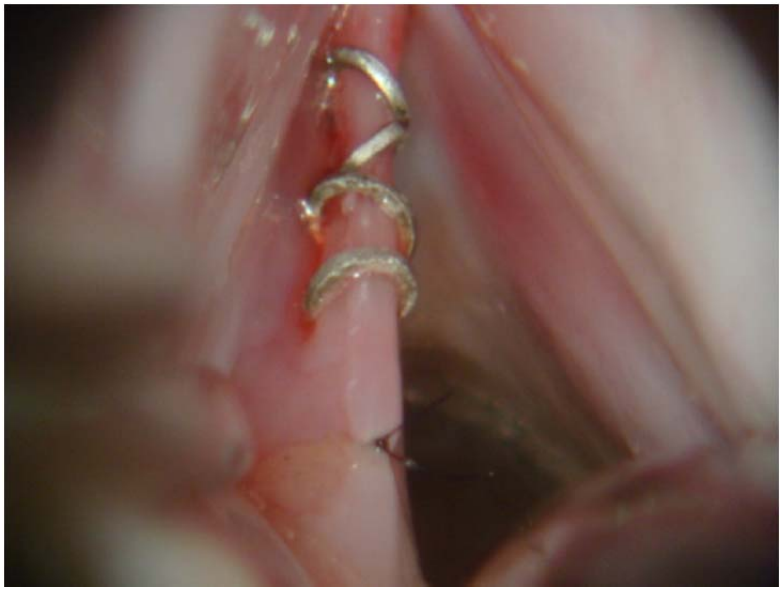

Figure.6.4 In-vivo application of micro-clips on porcine vocal cord. Four micro-clips of thickness 0.25mm are applied to appose the edges of the created epithelial flaps in order to promote primary intention

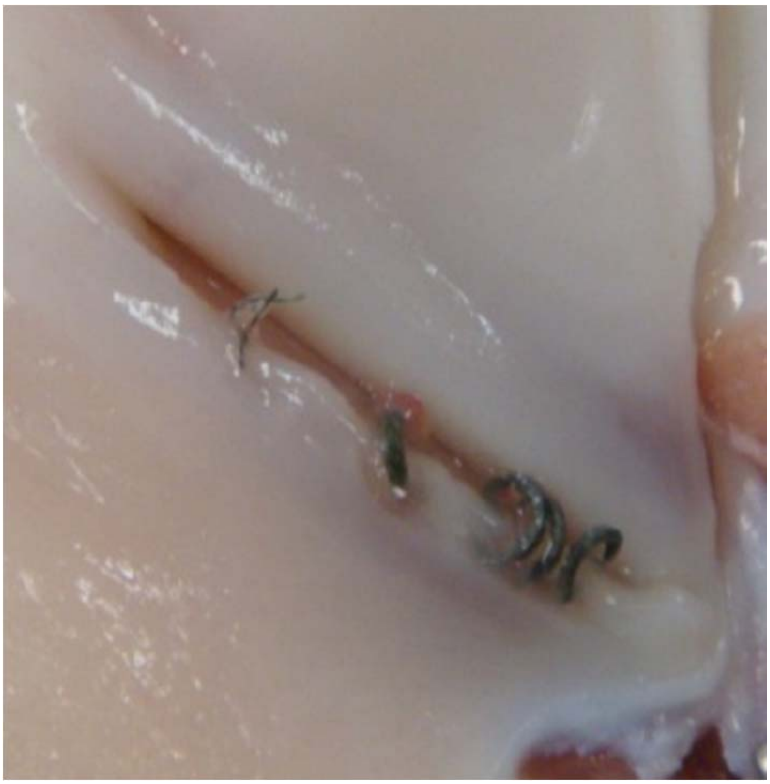

Figure.6.5 Excised vocal folds with embedded micro-clips 2 weeks after deployment. Micro-clips surface show various levels of degradation

6.3.2 In-vitro experiments

In-vitro immersion tests were carried out with two groups of clips (Figure.6.6). Both groups of clips were immersed in a solution made of 10:1 concentration of Hanks's balanced salt solution (HBSS; Sigma Aldrich) for the same amount of time. One group of clips was tested under tension (Figure 6.6(b)), the clips were first clamped into a round shape and then fixed onto the screws using thread. Tension force on the thread was set to 5N by torque gauge. The clips under tension were then immersed into HBSS. Another group of clips was immersed in the solution (Figure 6.6(a)) without any physical constraints. They were known as loaded and unloaded groups respectively. Tension force in the loaded group was set to 5N by torque gauge. Each group contained five sets of clips, and each set contained five clips. To expedite the process of corrosion testing, the temperature was maintained around 37℃ and the concentration of NaCl was maintained at 8 gl^{-1} as compared to the documented concentration of 0.85 gl^{-1} [231]. A minimum volume to surface area of specimen exposed of 0.22 mm^2 ml^{-1} was ensured to nullify effects of

oversaturation, according to the ASTM-G31-72 [232]. In order to prevent limiting effects of concentration polarization of the cathodic hydrogen evolution, a magnetic stirrer with a rotation speed of 60 rpm was placed at the bottom of the conical flasks. The pH of the solution was first record at 7.36 and maintained at the same level during the one month period of immersion tests. Specimens were subjected to atmospheric drying in a dry cabinet for 48h before their corrosion products were removed manually with silicon carbide 2000 grit paper and their weight was recorded.

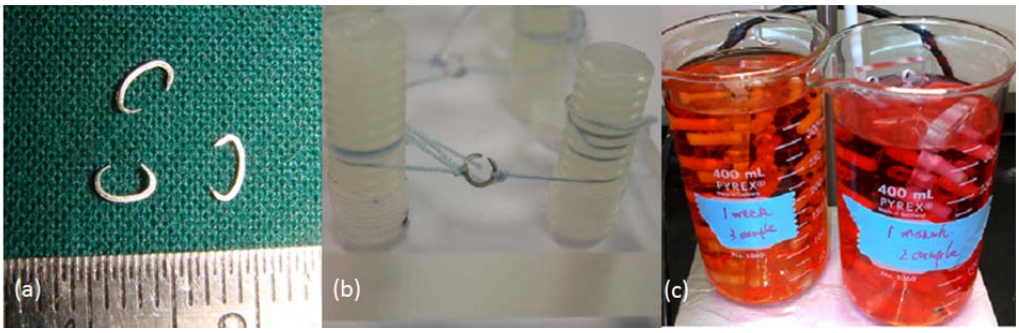

Figure.6.6 Images of the in-vitro experiment: (a) Unloaded clips used in the experiments; (b) Clips suspended and placed in tension using thread; (c) Clips immersed in HBSS during the study

6.4 Model calibration and validation

The degradation model is calibrated based on the results of in-vitro immersion tests. The predicted mass remaining vs. time curve should quantitatively match that observed in in-vitro experiment. The experimental mass loss and fitting results are shown in following Figure.6.7. The mass of the first group (Figure.6.7 (a)) of clips was measured on the first day, third day, first week, second week and fourth week while the mass of the clips in the second group (Figure.6.7 (b)) were measured every 3.5 days. The degradation model is capable of capturing the experimentally observed rate of mass loss over time. The value of time characteristic parameter τ_D of both groups is shown in the following Table.

Table.6.1 Value of time characteristic parameter

Group No	τ_D	R^2	RMSE
1	241.41	0.9829	0.0474
2	245.31	0.9942	0.0249

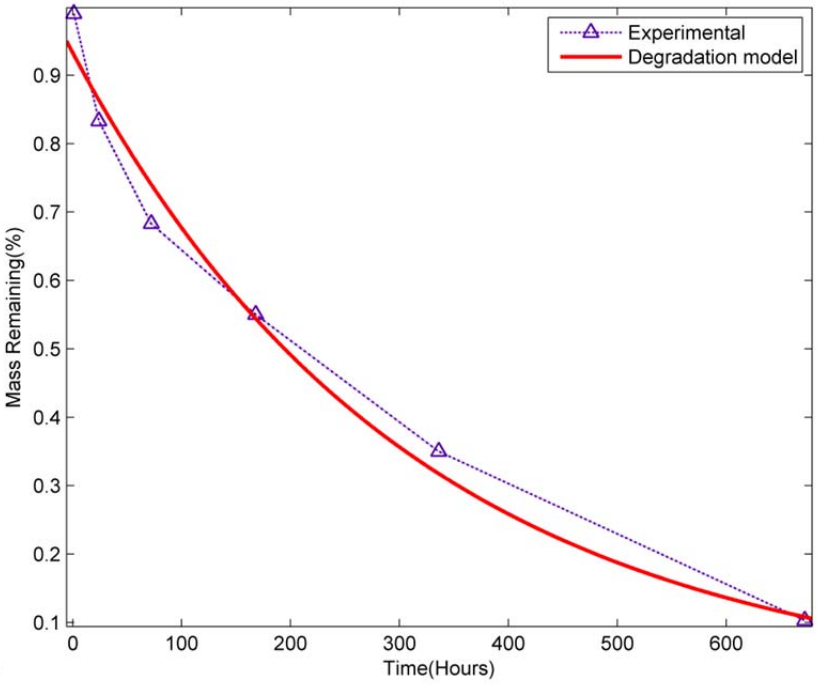

(a)

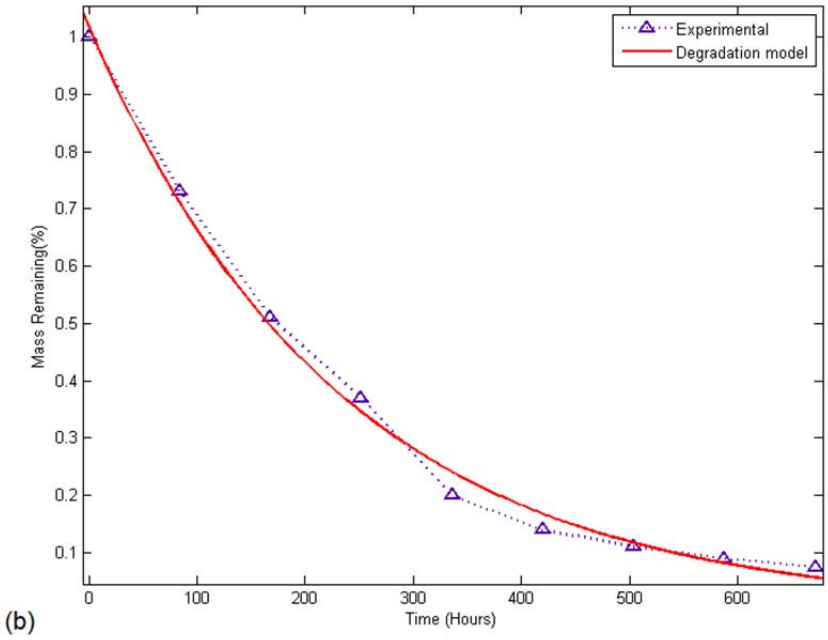

Figure.6.7 Plot of percentage mass remaining over different time intervals based on the results of in-vitro immersion test (dash line).The degradation model mass remaining prediction is also included (red line). (a) First group; (b) Second group

Displacements of each element due to degradation are also obtained by accumulating Δu to previous position based on Eq.(6.11) and (6.12). Note that the energy distribution is updated as the elasticity and rigidity parameters α and β are changed during degradation. Simulation of the in-vitro degradation process is conducted based on time. Five stages of degradation are illustrated in Figure.6.8. Each stage represents a certain time period according to the in-vitro degradation experiment. The simulated results, loaded clip group and unloaded clip group are represented by column one, two and three, respectively. Both groups of clips underwent immersion treatment for one month. Only the first five stages of both groups are presented since rate of weight loss would slow down in the later stages. For ease of illustration, the projected *XY* view of the clip is displayed.

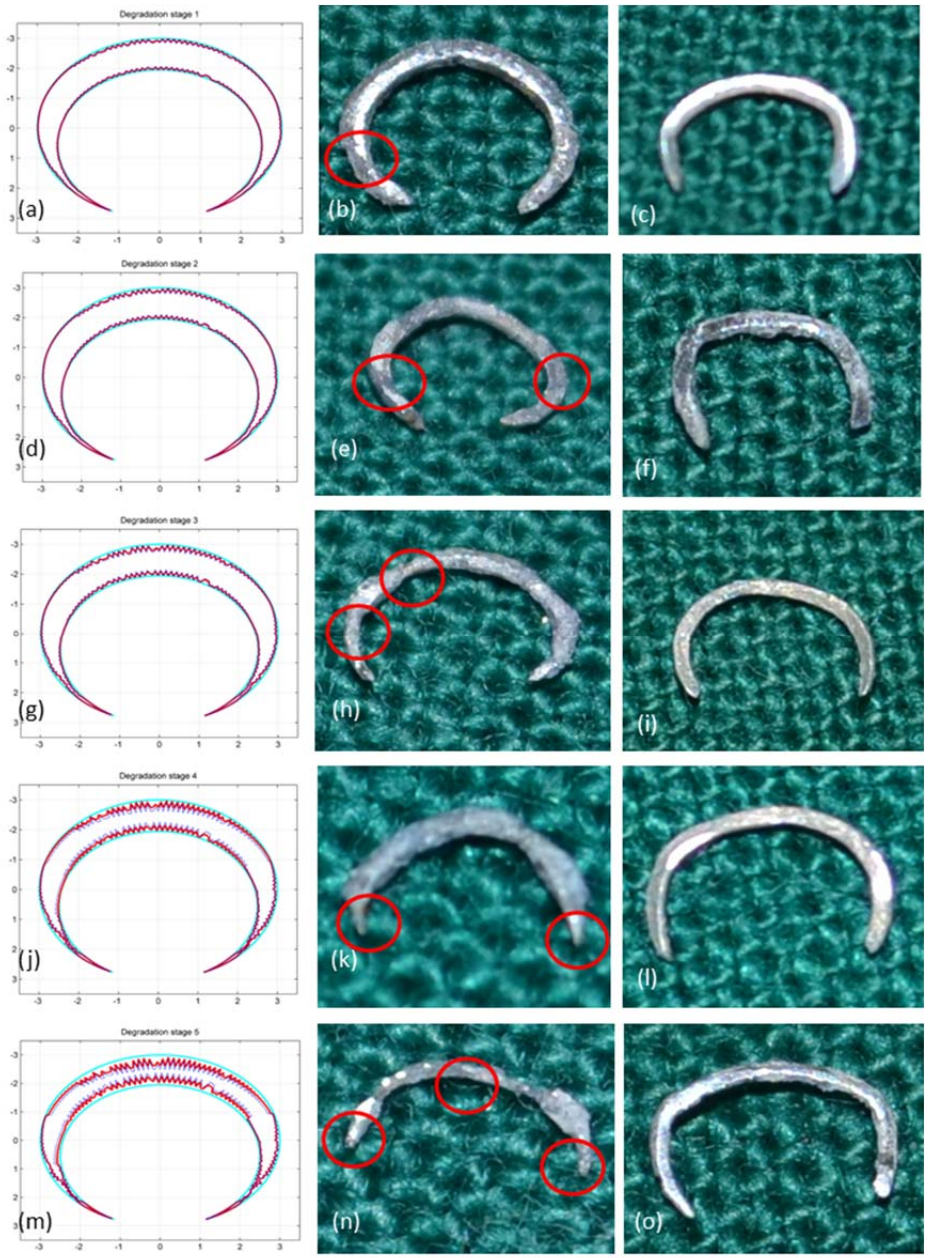

Figure.6.8 Degradation stages of the clip: five stages of degradation are simulated from (a) to (l) in pairs with a certain time period:(a)-(c) 0.5 week; (d)-(f) 1 week; (g)-(i) 1.5 weeks; (j)-(l) 2 weeks; (m)-(o) 2.5 weeks. The Green line indicates the original shape of the clip; red line illustrates the degradation shape of previous stage; blue line shows the degradation shape of current stage

As deformation was inhomogeneous due to complexity of the tool-tissue interaction process as well as geometry of the clip, the increase in degradation was also inhomogeneous. As seen in the figures, the three parts of the clip (middle part and two legs) subjected to greater deformations degraded faster than other parts in the first week (Figure.6.8 (a)-Figure.6.8 (f)). Two sections of the legs were found to be fracture from the second week due to degradation

(Figure.6.8 (g) and Figure.6.8 (h)) and the rest would continue to degrade as shown in Figure.6.8 (i) and Figure.6.8 (j). Areas highlighted with the red circles indicate the inhomogeneous degradation results between loaded and unloaded clips.

6.5 Discussions and conclusions

The degradation model is parameterized based on results of the in-vitro experiment. By obtaining best fitted time parameters, degradation simulation of the in-vitro immersion experiment is performed. Since the results from the degradation model developed in this work is capable of describing observed inhomogeneous degradation behaviors, strain deformation on the clips is a primary factor in accelerating the degradation process.

From the simulated degradation results (Figure.6.8), predicted degradation completes with only the distal ends of the clip remaining. This concurs with our in-vivo experimental results that only the distal ends remained in the tissue after four weeks[191]. While in-vivo experiments may provide the most realistic environment for investigation, their results can be heavily affected by many uncontrollable factors. For example, the coughing of the experimental subjects due to irritation experienced during wound healing may make the clip to vibrations and force it out of the tissue. Hence, it is conceded that using in-vivo experimental results to validate the simulation results for this work may not be conclusive. In-vitro experiment thus serves as a reasonable validation for the simulated strain-induced degradation results. The potential of the proposed variational approach for degradation modeling and simulation for degradation prediction has been demonstrated.

In the in-vivo test, degradation of the biodegradable material began with the micro-clip clasped by wound tissue experiencing a cyclic force from the tissue during the degradation process. Similarly, in the in-vitro immersion tests, degradation began when the clips which were kept in tension, were soaked in HBS solution. The structural integrity of the biodegradable device was also affected by inhomogeneous degradation due to the inhomogeneous deformation of the micro-clip. Sections of the clip undergoing larger

deformation experience greater degradation, whereas some parts do not degrade as they remain almost unstrained during the tool-tissue interaction. The in-vitro experimental results concur with the assumption that degradation has a strong dependence on the strain distribution within the body. Due to the boundary condition in FE modeling, simulation results of the degradation process would have different results since the loading force and/or shape of the degradation material varies.

Biodegradable implant design will be enhanced by the development of precise modeling methods of the degradation process. As material degradation could affect structural integrity of the biodegradable device leading to unpredictable failure, pre-clinical assessment of the device using computer models could significantly reduce unanticipated device failure. The constitutive model in this work helps with the numerical simulation of the degradation process. Degradation is quantified by accumulating the displacements in the computational process to the original position of each element. The inhomogeneous degradation highlighted by the red circles validate that different strain level would result in different degradation rate. Degradation rate is strain dependent since intermediate physical energy is decided by reaction stress. The parts under large tension, especially the two legs, would have more physical energy than other parts which leads to higher degradation rate. Thus, the degradation process that takes place with a strain-dependent degradation rate and the biodegradable material illustrate an inhomogeneous degradation process based on strains distribution within the body.

This study focuses on the mechanical aspects of strain-energy modulated degradation. Compared to other degradation modeling methods on metallic stents or polymers, this work provides important insights into the fundamental degradation mechanisms of biodegradable clips. The degradation model in this work is in agreement with previous works that strain-controlled degradation plays an important role in the degradation [210, 211, 233, 234]. However, previous works confines their study to exploring the effects of degradation on specimens' mechanical integrity. Our work investigates the effect of strain energy in degradation. Degradation simulation carried out based on strain

energy distribution and its experimental validation contributes to the study of bioresorbable device for medical applications. The ability to make accurate prediction of degradation is of particular relevance in the development of new degradable wound closure devices. In order to attain clinical requirements, strengthening the sections of device which would degrade faster based on the degradation model could ensure completion of the healing process before the device loses its mechanical integrity.

We have demonstrated the potential of micro-clips as a reliable wound closure device. Experiments were conducted to compare the performance of magnesium based micro-clips and compatible sutures. The experiments are designed as following: Two strings of thin silicon sheet were first tied together using three clips or one circle of 5-0 suture; the silicon sheets were then pulled towards opposite direction until the connection part was broken. The pulling force during test was measured and recorded at regular time intervals. The typical strength of a single magnesium clip is 3N. A typical wound closure in voice microsurgery will require three clips to complete the closure or two circles of sutures. The strength of one circle of 5-0 suture is about 5 N. The total force for clips and sutures is more or less the same. Thus, the magnesium clips will provide the same mechanical support as that of the equivalent sutures.

The degradation model developed in this work has some limitations. Since this work only focuses on the strain effect on degradation, the in-vitro experiments were designed for strain-induced degradation. Other degradation relevant factors, such as temperature and autocatalysis due to degradation byproducts and diffusion of water inside the body were not investigated. Future studies will be carried out to include the effects of these factors. Multi-physics simulation will be used instead of the conventional finite element methods.

To conclude, computer modeling and simulation of the degradation of a bioresorbable micro-clip for voice microsurgery is presented. The degradation process which is defined as an energy minimization problem, has considered the material and geometry of the device as well as its deployment in the wound closure site. A novel approach combining active contour and

incremental FE method has been employed to solve the energy minimization problem to determine the stable state of the clip after deployment. The degradation rate and geometries of the clip during degradation is computed based on the physical energy, and has been validated by experimental results. The numerical method described in this study is also applicable to other application of bioresorbable wound closure devices.

Chapter 7 Conclusions and Future works

7.1 Conclusions

This thesis focuses on studying the mechanical properties of biological soft tissue using variational approaches. The findings of this study make several contributions to the realistic modeling and simulation of tool tissue interaction. The theoretical scheme of these variational approaches is first introduced in Chapter 3, which discussed the mathematical models that are utilized in following chapters.

Our first investigation is to study the mechanical properties of vascular soft tissue. We analyzed the uncertainties of mechanical properties of human iliac arteries in tensile experiments, and then proposed a GA based probabilistic material characterization approach to quantitatively study the stiffness variations in human artery tissue. Probabilistic uncertainty analysis was conducted to model the uncertainties of human artery tissue. The relationship between the uncertainties on the observations and the estimated parameters is a major phenomenon to consider in modeling tissue properties. This is the first study which utilizes a statistical model to investigate the inhomogeneous mechanical properties of human arterial tissue. The proposed method is applicable for accurate modelling of soft biological tissue properties and realistic medical simulation.

In addition, we investigated the mechanical properties of vascular soft tissue during division after statistically modeling the human arterial tissue properties. A mass-spring model was utilized to analyze the mechanical response of human vascular tissue during cutting process. Division experiments were performed on the human iliac arteries using laparoscopic scissors. Characterization of the elasticity modulus was performed by solving a variational problem. Validation of the proposed elasticity equation was carried out by plotting experimental data and predicted data together which demonstrated the feasibility of this approach. An optimization method based on genetic algorithm was also proposed to improve elasticity reconstruction problem. The proposed mechanical model was used to study the structural

mechanics of the human artery tissue whereas the genetic algorithm was utilized to optimize the model accuracy.

The second contribution of this dissertation is on the variational modeling of nonlinear mechanical properties of gallbladder organ and virtual simulation with haptic rendering. To study the nonlinear mechanical properties of gallbladder tissue, a variational approach based on exponential strain energy function is proposed for the gallbladder organ. The material constants for the exponential strain energy model were determined from the uniaxial mechanical tests and characterized by solving a minimization problem. The genetic algorithm demonstrates good applicability in characterizing the material parameters. The predicted stress-strain relationship fits closely to the experimental data, which validates the feasibility of the proposed model and the reliability of the material constants to represent the properties of gallbladder organ. The nonlinear variational model serves as an appropriate approach for accurate simulation of soft tissue deformation with haptic rendering. The soft tissue material model was implemented in a medical simulation system with haptic force feedback. The physical based gallbladder model was assigned with nonlinear hyperelastic properties. Haptic rendering utilizing the proposed model enables the user to feel the distinct force when the gallbladder is held or stretched. The nonlinear tissue model provides an accurate material model for advanced surgical simulation.

Besides the gallbladder organ haptic simulation system, haptic guidance system is developed and presented in second section of Chapter 5. The operation paths of the system were constrained by the guidance force within the predefined curve. Incremental potential field was employed to model the storing energy around the predefined path. Gradient descent method was utilized for variationally determine the value and direction of guidance force. Guidance force and reaction force was integrated together in the tracheal reconstruction simulation system.

Finally, our study contributes to new knowledge on tool-tissue interaction which affects the degradation process of biodegradable materials. We proposed a novel energy minimization approach to model degradation of

bioresorbable micro-clips for wound closure. The degradation of the biodegradable clips is assumed to be highly related to the strain energy on the clips resulted from tool-tissue interaction process. The degradation process which considers both material properties and geometry of the device as well as its deployment was modeled as an energy minimization problem that is iteratively solved using active contour and incremental finite element methods. Strain energy of the micro-clip during degradation was computed using active contour. The degradation rate was then calculated from strain energy using a transformation formulation. By relating strain energy to material degradation, the degradation rates and geometries of the micro-clip during degradation were represented using a degradation map. Computer modeling and simulation of the degradation of a bioresorbable micro-clip for voice microsurgery was presented based on the computation results. The computer simulation of the degradation of the micro-clips agreed with the in-vivo and in-vitro experimental results which demonstrate the reliability of this study.

7.2 Future works

Using the proposed variational modeling methods, many applications could be achieved. Possible future research directions are suggested as follows:

- **Haptic guidance and augmented reality system**

In medical training, the apprenticeship model has been utilized effectively by the medical profession for centuries [174]. Currently, there is unremitting pressure to update and reform conventional medical training modes. Patient safety in particular has been regarded as the most important issue to consider during the medical procedures. These concerns has led surgical management adapting innovative minimal access approaches, which in turn raise further challenges of training the increasingly complex skills required. In this case, virtual medical simulations offer a potential effective approach for pre-training of practitioners, which can meet the requirement of aforementioned issues as well as reproduce the abdominal environment of patients realistically.

As haptic feedback alone does not provide enough information to produce an immersive medical training simulation, invariably visual and sometimes auditory feedback is incorporated. Integrating augmented reality with the haptic guidance system presented in Chapter 5 will provide an economical and effective method for construction of high fidelity medical training system.

- **Degradation simulation on voice prosthesis**

Despite the wound closure devices, this invention can also applied to model the degradation process of voice surgery implant-voice prosthesis.

Total laryngectomy (TL) is often used as treatment for advanced staged laryngeal cancers. The subsequent loss of voice impairs communication with disabling psychosocial and economic consequences for the patient. Prosthetic voice restoration provides the closest approximation to normal laryngeal voice and is considered to be the gold standard of choice. Prosthetic voice restoration involves the implantation of voice prosthesis (VP) in a surgically created fistula between the posterior tracheal wall and the anterior esophageal wall.

The voice prosthesis can be made of two layers, one layer is made of plastic and the other layer is made of biodegradable materials, as shown by the following figure.

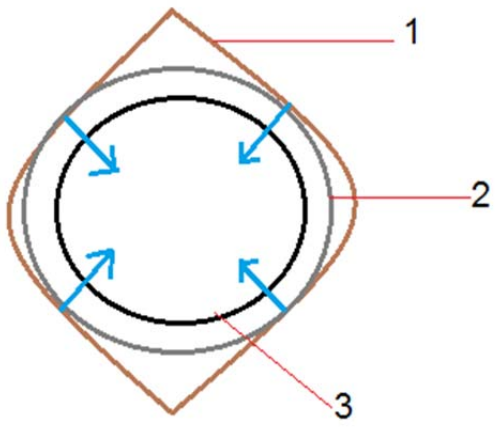

Figure.7.1 Image shows the working condition of voice prosthesis. 1. Wound on the tissue; 2.Biodegradable material layer; 3.Foundation layer

When the voice prosthesis is inserted into the wound, it will receive a pressure from the contact face. The biodegradable layer will degraded to fit the shape of wound while the wound is healing. The shape of wound and voice prosthesis will reach a stable state after a certain period of time.

This degradation process can also be modeled using the above algorithm. By taking the above modeling steps, we can predicate the shape of voice prosthesis after degradation. The predication can be used as reference to improve the design of voice prosthesis, with the purpose of protecting the foundation layer as well as extending the lifespan of the device.

- **Investigation the mechanical properties of other organs using the proposed variational approach**

Based on the theories introduced in Chapter 3, we have modeled the nonlinear mechanical properties of both gallbladder and human vascular tissues. Under the assumption that a variety of soft tissues are comprised of similar constituents (collagen, cells, extracellular fluid, etc.) and sharing the same incompressible feature to some extent, the models developed in this work could be further developed to model the nonlinear mechanical response of other perfused, solid, abdominal, organs such as liver, spleen and kidney. A unique set of material parameters will be obtained for particular tissue depending on the amount and type of constituent within the tissue. For example, as liver has been shown to have a stiffer response than spleen[74], it would present a higher value in the elastic parameters compared with the spleen tissue. The situation for the kidney would be opposite, which demonstrates a stiffer response than the liver [235]. In this way, a comprehensive database of different tissue properties could be identified, which can be further utilized in the virtual simulation system.

Reference

1. Rosen, J., et al. *The BlueDRAGON-a system for measuring the kinematics and dynamics of minimally invasive surgical tools in-vivo*. in *Robotics and Automation, 2002. Proceedings. ICRA'02. IEEE International Conference on*. 2002. IEEE.
2. Issenberg, S.B., et al., *Simulation technology for health care professional skills training and assessment.* JAMA: the journal of the American Medical Association, 1999. **282**(9): p. 861-866.
3. Tendick, F., et al., *A virtual environment testbed for training laparoscopic surgical skills.* Presence: Teleoperators & Virtual Environments, 2000. **9**(3): p. 236-255.
4. Liu, A., et al., *A survey of surgical simulation: applications, technology, and education.* Presence: Teleoperators & Virtual Environments, 2003. **12**(6): p. 599-614.
5. Delingette, H., *Toward realistic soft-tissue modeling in medical simulation.* Proceedings of the IEEE, 1998. **86**(3): p. 512-523.
6. Dobrin, P.B. and T.R. Canfield, *Elastase, collagenase, and the biaxial elastic properties of dog carotid artery.* American Journal of Physiology-Heart and Circulatory Physiology, 1984. **247**(1): p. H124-H131.
7. Guinea, G.V., et al., *Thermomechanical behavior of human carotid arteries in the passive state.* Am J Physiol Heart Circ Physiol, 2005. **288**(6): p. H2940-H2945.
8. Sommer, G., et al., *Biaxial mechanical properties of intact and layer-dissected human carotid arteries at physiological and supraphysiological loadings.* American Journal of Physiology-Heart and Circulatory Physiology, 2010. **298**(3): p. H898-H912.
9. Lally, C., A. Reid, and P. Prendergast, *Elastic behavior of porcine coronary artery tissue under uniaxial and equibiaxial tension.* Annals of Biomedical Engineering, 2004. **32**(10): p. 1355-1364.
10. Ebenstein, D.M., et al., *Nanomechanical properties of calcification, fibrous tissue, and hematoma from atherosclerotic plaques.* Journal of Biomedical Materials Research Part A, 2009. **91**(4): p. 1028-1037.
11. Chui, C., et al., *Transversely isotropic properties of porcine liver tissue: experiments and constitutive modelling.* Medical and Biological Engineering and Computing, 2007. **45**(1): p. 99-106.
12. Yang, T., et al., *Quasi-linear viscoelastic modeling of arterial wall for surgical simulation.* International Journal of Computer Assisted Radiology and Surgery, 2011. **6**(6): p. 829-838.
13. Kerdok, A.E., *Characterizing the nonlinear mechanical response of liver to surgical manipulation*, 2006, Harvard University Cambridge, MA.
14. Nesme, M., et al., *Physically realistic interactive simulation for biological soft tissues.* Recent Research Developments in Biomechanics, 2005. **2**: p. 1-22.
15. James, D.L. and D.K. Pai. *ArtDefo: accurate real time deformable objects*. in *Proceedings of the 26th annual conference on Computer graphics and interactive techniques*. 1999. ACM Press/Addison-Wesley Publishing Co.
16. Müller, M., et al. *Point based animation of elastic, plastic and melting objects*. in *Proceedings of the 2004 ACM SIGGRAPH/Eurographics symposium on Computer animation*. 2004. Eurographics Association.
17. Hauser, K.K., C. Shen, and J.F. O'brien. *Interactive deformation using modal analysis with constraints*. in *Graphics Interface*. 2003.

18. Teschner, M., et al. *A versatile and robust model for geometrically complex deformable solids*. in *Computer Graphics International, 2004. Proceedings*. 2004. IEEE.
19. Müller, M., et al. *Meshless deformations based on shape matching*. in *ACM Transactions on Graphics (TOG)*. 2005. ACM.
20. Kojić, M., et al., *Computer modeling in bioengineering: theoretical background, examples and software*2008: Wiley.
21. Ortiz, M. and L. Stainier, *The variational formulation of viscoplastic constitutive updates.* Computer methods in applied mechanics and engineering, 1999. **171**(3): p. 419-444.
22. Radovitzky, R. and M. Ortiz, *Error estimation and adaptive meshing in strongly nonlinear dynamic problems.* Computer methods in applied mechanics and engineering, 1999. **172**(1): p. 203-240.
23. Yang, Q., L. Stainier, and M. Ortiz, *A variational formulation of the coupled thermo-mechanical boundary-value problem for general dissipative solids.* Journal of the Mechanics and Physics of Solids, 2006. **54**(2): p. 401-424.
24. Ortiz, M. and A. Pandolfi, *A variational Cam-clay theory of plasticity.* Computer methods in applied mechanics and engineering, 2004. **193**(27): p. 2645-2666.
25. Weinberg, K., A. Mota, and M. Ortiz, *A variational constitutive model for porous metal plasticity.* Computational Mechanics, 2006. **37**(2): p. 142-152.
26. Fancello, E., J.-P. Ponthot, and L. Stainier, *A variational framework for nonlinear viscoelastic models in finite deformation regime.* Journal of Computational and Applied Mathematics, 2008. **215**(2): p. 400-408.
27. Ogden, R., *Large deformation isotropic elasticity-on the correlation of theory and experiment for incompressible rubberlike solids.* Proceedings of the Royal Society of London. A. Mathematical and Physical Sciences, 1972. **326**(1567): p. 565-584.
28. Ardagh, M., *May we practise endotracheal intubation on the newly dead?* Journal of Medical Ethics, 1997. **23**(5): p. 289-294.
29. Xu, H., S. Teoh, and Y. Sun, *Computational Models for Mechanical Deformation of Soft Tissues of the Central Nervous System.* 2002.
30. Rueckert, D., et al., *Nonrigid registration using free-form deformations: application to breast MR images.* Medical Imaging, IEEE Transactions on, 1999. **18**(8): p. 712-721.
31. Soncul, M. and M.A. Bamber, *Evaluation of facial soft tissue changes with optical surface scan after surgical correction of Class III deformities.* Journal of oral and maxillofacial surgery, 2004. **62**(11): p. 1331-1340.
32. Delingette, H., S. Cotin, and N. Ayache, *Efficient linear elastic models of soft tissues for real-time surgery simulation.* Studies in Health Technology and Informatics, 1999: p. 100-101.
33. Bro-Nielsen, M., *Finite element modeling in surgery simulation.* Proceedings of the IEEE, 1998. **86**(3): p. 490-503.
34. Sederberg, T.W. and S.R. Parry. *Free-form deformation of solid geometric models*. in *ACM SIGGRAPH Computer Graphics*. 1986. ACM.
35. Kass, M., A. Witkin, and D. Terzopoulos, *Snakes: Active contour models.* International Journal of Computer Vision, 1988. **1**(4): p. 321-331.
36. Moore, P. and D. Molloy. *A survey of computer-based deformable models*. in *Machine Vision and Image Processing Conference, 2007. IMVIP 2007. International*. 2007. IEEE.

37. Barr, A.H. *Global and local deformations of solid primitives*. in *ACM SIGGRAPH Computer Graphics*. 1984. ACM.
38. Coquillart, S., *Extended free-form deformation: a sculpturing tool for 3D geometric modeling*. Vol. 24. 1990: ACM.
39. Coquillart, S. and P. Jancene, *Animated free-form deformation: an interactive animation technique*. Vol. 25. 1991: ACM.
40. Rueckert, D., et al., *Nonrigid registration using free-form deformations: application to breast MR images.* Medical Imaging, IEEE Transactions on, 1999. **18**(8): p. 712-721.
41. Rohlfing, T., et al., *Modeling liver motion and deformation during the respiratory cycle using intensity-based free-form registration of gated MR images.* 2001: p. 337-348.
42. Rohlfing, T., et al., *Volume-preserving nonrigid registration of MR breast images using free-form deformation with an incompressibility constraint.* Medical Imaging, IEEE Transactions on, 2003. **22**(6): p. 730-741.
43. Schein, S. and G. Elber. *Discontinuous free form deformations*. in *Computer Graphics and Applications, 2004. PG 2004. Proceedings. 12th Pacific Conference on*. 2004. IEEE.
44. Sela, G., et al., *Real-time haptic incision simulation using FEM-based discontinuous free-form deformation.* Computer-Aided Design, 2007. **39**(8): p. 685-693.
45. Ng-Thow-Hing, V., et al. *Shape reconstruction and subsequent deformation of soleus muscle models using b-spline solid primitives*. in *BiOS'98 International Biomedical Optics Symposium*. 1998. International Society for Optics and Photonics.
46. Schreibmann, E., G.T. Chen, and L. Xing, *Image interpolation in 4D CT using a BSpline deformable registration model.* International Journal of Radiation Oncology* Biology* Physics, 2006. **64**(5): p. 1537-1550.
47. Luo, G. and P.A. Heng, *LV shape and motion: B-spline-based deformable model and sequential motion decomposition.* Information Technology in Biomedicine, IEEE Transactions on, 2005. **9**(3): p. 430-446.
48. Richa, R., P. Poignet, and C. Liu, *Three-dimensional motion tracking for beating heart surgery using a thin-plate spline deformable model.* The International Journal of Robotics Research, 2010. **29**(2-3): p. 218-230.
49. Terzopoulos, D. and K. Waters, *Physically‐based facial modelling, analysis, and animation.* The journal of visualization and computer animation, 1990. **1**(2): p. 73-80.
50. Gibson, S.F. *3D chainmail: a fast algorithm for deforming volumetric objects*. in *Proceedings of the 1997 symposium on Interactive 3D graphics*. 1997. ACM.
51. Baumann, R., et al., *Force feedback for virtual reality based minimally invasive surgery simulator.* Studies in Health Technology and Informatics, 1996. **29**: p. 564.
52. Meseure, P. and C. Chaillou. *Deformable body simulation with adaptive subdivision and cuttings*. in *Proceedings of the WSCG*. 1997. Citeseer.
53. Waters, K., *A muscle model for animation three-dimensional facial expression.* ACM SIGGRAPH Computer Graphics, 1987. **21**(4): p. 17-24.
54. Waters, K. *Physical model of facial tissue and muscle articulation derived from computer tomography data*. in *Visualization in Biomedical Computing*. 1992. International Society for Optics and Photonics.

55. Chadwick, J.E., D.R. Haumann, and R.E. Parent. *Layered construction for deformable animated characters*. in *ACM SIGGRAPH Computer Graphics*. 1989. ACM.
56. Waters, K. and D. Terzopoulos, *Modelling and animating faces using scanned data.* The journal of visualization and computer animation, 1991. **2**(4): p. 123-128.
57. Castaneda, M.P. and F.A. Cosío. *Computer simulation of prostate resection for surgery training*. in *Engineering in Medicine and Biology Society, 2003. Proceedings of the 25th Annual International Conference of the IEEE*. 2003. IEEE.
58. Delingette, H., et al. *Craniofacial surgery simulation testbed*. in *Visualization in Biomedical Computing 1994*. 1994. International Society for Optics and Photonics.
59. d'Aulignac, D., R. Balaniuk, and C. Laugier. *A haptic interface for a virtual exam of the human thigh*. in *Robotics and Automation, 2000. Proceedings. ICRA'00. IEEE International Conference on*. 2000. IEEE.
60. d'Aulignac, D., C. Laugier, and M. Cavusoglu. *Towards a realistic echographic simulator with force feedback*. in *Intelligent Robots and Systems, 1999. IROS'99. Proceedings. 1999 IEEE/RSJ International Conference on*. 1999. IEEE.
61. Nealen, A., et al. *Physically based deformable models in computer graphics*. in *Computer Graphics Forum*. 2006. Wiley Online Library.
62. Basafa, E., F. Farahmand, and G. Vossoughi, *A non-linear mass-spring model for more realistic and efficient simulation of soft tissues surgery.* Studies in Health Technology and Informatics, 2008. **132**: p. 23.
63. Schwartz, J.-M., et al., *Modelling liver tissue properties using a non-linear visco-elastic model for surgery simulation.* Medical Image Analysis, 2005. **9**(2): p. 103.
64. Villard, P.-F., W. Bourne, and F. Bello, *Modelling organ deformation using mass-springs and tensional integrity*, in *Biomedical Simulation*2008, Springer. p. 221-226.
65. Delingette, H. and N. Ayache, *Soft tissue modeling for surgery simulation.* Handbook of Numerical Analysis, 2004. **12**: p. 453-550.
66. Zhu, B. and L. Gu, *A hybrid deformable model for real-time surgical simulation.* Computerized Medical Imaging and Graphics, 2012.
67. Natsupakpong, S. and M. Cenk Çavuşoğlu, *Determination of elasticity parameters in lumped element (mass-spring) models of deformable objects.* Graphical Models, 2010. **72**(6): p. 61-73.
68. Fung, Y.C., *Biomechanics : mechanical properties of living tissues / Y.C. Fung*1981, New York :: Springer-Verlag.
69. Holzapfel, G.A., T.C. Gasser, and R.W. Ogden, *A new constitutive framework for arterial wall mechanics and a comparative study of material models.* Journal of Elasticity, 2000. **61**(1): p. 1-48.
70. Ogden, R.W., *Large Deformation Isotropic Elasticity: On the Correlation of Theory and Experiment for Compressible Rubberlike Solids.* Proceedings of the Royal Society of London. A. Mathematical and Physical Sciences, 1972. **328**(1575): p. 567-583.
71. Bro‐Nielsen, M. and S. Cotin. *Real‐time Volumetric Deformable Models for Surgery Simulation using Finite Elements and Condensation*. in *Computer graphics forum*. 1996. Wiley Online Library.
72. Basdogan, C., C.H. Ho, and M.A. Srinivasan, *Virtual environments for medical training: graphical and haptic simulation of laparoscopic common bile duct*

exploration. Mechatronics, IEEE/ASME Transactions on, 2001. **6**(3): p. 269-285.
73. Picinbono, G., H. Delingette, and N. Ayache, *Non-linear anisotropic elasticity for real-time surgery simulation.* Graphical Models, 2003. **65**(5): p. 305-321.
74. Carter, F., et al., *Measurements and modelling of the compliance of human and porcine organs.* Medical Image Analysis, 2001. **5**(4): p. 231-236.
75. Davies, P.J., F.J. Carter, and A. Cuschieri, *Mathematical modelling for keyhole surgery simulations: a biomechanical model for spleen tissue.* IMA journal of applied mathematics, 2002. **67**(1): p. 41-67.
76. Hu, T. and J.P. Desai, *Characterization of soft-tissue material properties: large deformation analysis*, in *Medical Simulation*2004, Springer. p. 28-37.
77. Chui, C., et al., *Combined compression and elongation experiments and non-linear modelling of liver tissue for surgical simulation.* Medical and Biological Engineering and Computing, 2004. **42**(6): p. 787-798.
78. Mooney, M., *A theory of large elastic deformation.* Journal of applied physics, 1940. **11**(9): p. 582-592.
79. Rivlin, R.S. and D. Saunders, *Large elastic deformations of isotropic materials. VII. Experiments on the deformation of rubber.* Philosophical Transactions of the Royal Society of London. Series A, Mathematical and Physical Sciences, 1951. **243**(865): p. 251-288.
80. Holzapfel, G.A., T.C. Gasser, and R.W. Ogden, *A new constitutive framework for arterial wall mechanics and a comparative study of material models.* Journal of elasticity and the physical science of solids, 2000. **61**(1-3): p. 1-48.
81. Ahn, B. and J. Kim, *Measurement and characterization of soft tissue behavior with surface deformation and force response under large deformations.* Medical Image Analysis, 2010. **14**(2): p. 138-148.
82. Mikhlin, S.G.e. and T. Boddington, *Variational methods in mathematical physics*. Vol. 1. 1964: Pergamon Press Oxford.
83. Horrigmoe, G. and P.G. Bergan, *Incremental variational principles and finite element models for nonlinear problems.* Computer methods in applied mechanics and engineering, 1976. **7**(2): p. 201-217.
84. Levenston, M., E. Frank, and A. Grodzinsky, *Variationally derived 3-field finite element formulations for quasistatic poroelastic analysis of hydrated biological tissues.* Computer methods in applied mechanics and engineering, 1998. **156**(1): p. 231-246.
85. Fancello, E., J.P. Ponthot, and L. Stainier, *A variational formulation of constitutive models and updates in non‐linear finite viscoelasticity.* International Journal for Numerical Methods in Engineering, 2006. **65**(11): p. 1831-1864.
86. Cotin, S., H. Delingette, and N. Ayache, *A hybrid elastic model for real-time cutting, deformations, and force feedback for surgery training and simulation.* The Visual Computer, 2000. **16**(8): p. 437-452.
87. Venkataraman, K., S. Lodha, and R. Raghavan, *A kinematic-variational model for animating skin with wrinkles.* Computers & Graphics, 2005. **29**(5): p. 756-770.
88. El Sayed, T., et al., *A variational constitutive model for soft biological tissues.* Journal of Biomechanics, 2008. **41**(7): p. 1458-1466.
89. Franceschini, G., et al., *Brain tissue deforms similarly to filled elastomers and follows consolidation theory.* Journal of the Mechanics and Physics of Solids, 2006. **54**(12): p. 2592-2620.

90. Schröder, J., P. Neff, and D. Balzani, *A variational approach for materially stable anisotropic hyperelasticity.* International Journal of Solids and Structures, 2005. **42**(15): p. 4352-4371.
91. Massoptier, L. and S. Casciaro. *Fully automatic liver segmentation through graph-cut technique*. in *Engineering in Medicine and Biology Society, 2007. EMBS 2007. 29th Annual International Conference of the IEEE*. 2007. IEEE.
92. Casciaro, S., et al., *A method for fast and automatic segmentation of soft organs from CT and MR images.* International Journal of Computer Assisted Radiology and Surgery, 2006. **1**: p. 470.
93. Fancello, E., J.M. Vassoler, and L. Stainier, *A variational constitutive update algorithm for a set of isotropic hyperelastic–viscoplastic material models.* Computer methods in applied mechanics and engineering, 2008. **197**(49): p. 4132-4148.
94. Xiong, L., C.-K. Chui, and C.-L. Teo, *Reality based modeling and simulation of gallbladder shape deformation using variational methods.* International Journal of Computer Assisted Radiology and Surgery, 2013: p. 1-9.
95. Ogden, R.W., G. Saccomandi, and I. Sgura, *Fitting hyperelastic models to experimental data.* Computational Mechanics, 2004. **34**(6): p. 484-502.
96. Sermesant, M., et al., *Patient-specific electromechanical models of the heart for the prediction of pacing acute effects in CRT: a preliminary clinical validation.* Medical Image Analysis, 2012. **16**(1): p. 201-215.
97. Konukoglu, E., et al., *Efficient probabilistic model personalization integrating uncertainty on data and parameters: Application to eikonal-diffusion models in cardiac electrophysiology.* Progress in Biophysics and Molecular Biology, 2011. **107**(1): p. 134-146.
98. Chuong, C. and Y. Fung, *Three-dimensional stress distribution in arteries.* Journal of Biomechanical Engineering, 1983. **105**(3): p. 268.
99. Fung, Y., S. Liu, and J. Zhou, *Remodeling of the constitutive equation while a blood vessel remodels itself under stress.* Journal of Biomechanical Engineering, 1993. **115**(4B): p. 453.
100. Zulliger, M.A., et al., *A strain energy function for arteries accounting for wall composition and structure.* Journal of Biomechanics, 2004. **37**(7): p. 989-1000.
101. Rhodin, J.A.G., *Architecture of the Vessel Wall*, in *Comprehensive Physiology*2011, John Wiley & Sons, Inc.
102. Du, X., A. Sudjianto, and W. Chen, *An integrated framework for optimization under uncertainty using inverse reliability strategy.* Journal of mechanical design, 2004. **126**(4): p. 562-570.
103. Du, X., J. Guo, and H. Beeram, *Sequential optimization and reliability assessment for multidisciplinary systems design.* Structural and Multidisciplinary Optimization, 2008. **35**(2): p. 117-130.
104. Baldwin, M.A., et al., *Efficient probabilistic representation of tibiofemoral soft tissue constraint.* Computer Methods in Biomechanics and Biomedical Engineering, 2009. **12**(6): p. 651-659.
105. Fu, Y.B., C.K. Chui, and C.L. Teo, *Liver tissue characterization from uniaxial stress–strain data using probabilistic and inverse finite element methods.* Journal of the Mechanical Behavior of Biomedical Materials, 2013. **20**(0): p. 105-112.
106. Chui CK, G.P., Wang ZL, Ong CJ, Teoh SH, and Sakuma I, *Constitutive modelling of blood vessels using combined energy function for surgical simulation*, in *2nd MRS-S Conference on Advanced Materials*2006: Singapore.

107. Tanaka, T.T. and Y.-C. Fung, *Elastic and inelastic properties of the canine aorta and their variation along the aortic tree.* Journal of Biomechanics, 1974. **7**(4): p. 357-370.
108. Shapiro, S.S. and M.B. Wilk, *An analysis of variance test for normality(complete samples)*, JSTOR.
109. Dey, A. and S. Mahadevan, *Ductile structural system reliability analysis using adaptive importance sampling.* Structural safety, 1998. **20**(2): p. 137-154.
110. Ding, K., Z. Zhou, and C. Liu, *Latin hypercube sampling used in the calculation of the fracture probability.* Reliability Engineering & System Safety, 1998. **59**(2): p. 239-242.
111. Moarefzadeh, M. and R. Melchers, *Directional importance sampling for ill-proportioned spaces.* Structural safety, 1999. **21**(1): p. 1-22.
112. McKay, M., R. Beckman, and W. Conover, *A comparison of three methods for selecting values of input variables in the analysis of output from a computer code.* Technometrics, 2000. **42**(1): p. 55-61.
113. Helton, J.C. and F.J. Davis, *Latin hypercube sampling and the propagation of uncertainty in analyses of complex systems.* Reliability Engineering & System Safety, 2003. **81**(1): p. 23-69.
114. Amar, J.G., *The Monte Carlo method in science and engineering.* Computing in science & engineering, 2006. **8**(2): p. 9-19.
115. Pukelsheim, F., *The Three Sigma Rule.* The American Statistician, 1994. **48**(2): p. 88-91.
116. Yamada, H. and F.G. Evans, *Strength of biological materials*1970: Williams & Wilkins.
117. Sommer, G., *Mechanical Properties of Healthy and Diseased Human Arteries: Insights Into Human Arterial Biomechanics and Related Material Modeling*2010: Verlag der Techn. Univ. Graz.
118. Apostolakis, G., *The concept of probability in safety assessments of technological systems.* Science, 1990. **250**(4986): p. 1359-1364.
119. He, Y. and D. Keyes, *Reconstructing parameters of the FitzHugh–Nagumo system from boundary potential measurements.* Journal of Computational Neuroscience, 2007. **23**(2): p. 251-264.
120. Weizsäcker, H., *Passive elastic properties of the rat abdominal vena cava.* Pflügers Archiv, 1988. **412**(1-2): p. 147-154.
121. Hayashi, K., K. Mori, and H. Miyazaki, *Biomechanical response of femoral vein to chronic elevation of blood pressure in rabbits.* American journal of physiology. Heart and circulatory physiology, 2003. **284**(2): p. H511-8.
122. Silver, F., P. Snowhill, and D. Foran, *Mechanical Behavior of Vessel Wall: A Comparative Study of Aorta, Vena Cava, and Carotid Artery.* Annals of Biomedical Engineering, 2003. **31**(7): p. 793-803.
123. Minten, J., et al., *Correlation between mechanical properties and wall composition of the canine superior vena cava.* Arch Physiol Biochem, 1986. **94**(5): p. 349-362.
124. Schmitt, L.M., *Theory of genetic algorithms.* Theoretical Computer Science, 2001. **259**(1): p. 1-61.
125. Kanber, B. and K.V. Ramnarine, *A Probabilistic Approach to Computerized Tracking of Arterial Walls in Ultrasound Image Sequences.* ISRN Signal Processing, 2012. **2012**: p. 11.
126. El-Baz, A., et al. *Probabilistic Modeling of Blood Vessels for Segmenting MRA Images*. in *Pattern Recognition, 2006. ICPR 2006. 18th International Conference on*. 2006. IEEE.

127. Mountney, P., et al., *A probabilistic framework for tracking deformable soft tissue in minimally invasive surgery*, in *Medical Image Computing and Computer-Assisted Intervention–MICCAI 2007*2007, Springer. p. 34-41.
128. Satava, R.M., *Accomplishments and challenges of surgical simulation.* Surgical Endoscopy, 2001. **15**(3): p. 232-241.
129. Basdogan, C., et al., *Haptics in minimally invasive surgical simulation and training.* Computer Graphics and Applications, IEEE, 2004. **24**(2): p. 56-64.
130. Rosen, J., et al., *Force controlled and teleoperated endoscopic grasper for minimally invasive surgery-experimental performance evaluation.* Biomedical Engineering, IEEE Transactions on, 1999. **46**(10): p. 1212-1221.
131. Greenish, S., et al., *Measurement, analysis, and display of haptic signals during surgical cutting.* Presence: Teleoperators & Virtual Environments, 2002. **11**(6): p. 626-651.
132. Hayashi, K., *Experimental approaches on measuring the mechanical properties and constitutive laws of arterial walls.* Journal of Biomechanical Engineering, 1993. **115**(4B): p. 481-488.
133. Mahvash, M., V. Hayward, and J. Lloyd. *Haptic rendering of tool contact*. in *Proc. Eurohaptics*. 2002.
134. Mahvash, M., et al., *Modeling the forces of cutting with scissors.* Biomedical Engineering, IEEE Transactions on, 2008. **55**(3): p. 848-856.
135. Hayashi, K., et al., *Stiffness and elastic behavior of human intracranial and extracranial arteries.* Journal of Biomechanics, 1980. **13**(2): p. 175-184.
136. Buchthal, F., *The rheology of the cross striated muscle fibre: with particular reference to isotonic conditions*. Vol. 21. 1951: I kommission hos Munksgaard.
137. Viidik, A., *Biomechanics and Functional Adaption of Tendons and Joint Ligaments*, in *Studies on the Anatomy and Function of Bone and Joints*, F.G. Evans, Editor 1966, Springer Berlin Heidelberg. p. 17-39.
138. Hauth, M., et al., *Soft tissue simulation based on measured data*, in *Medical Image Computing and Computer-Assisted Intervention-MICCAI 2003*2003, Springer. p. 262-270.
139. Khalil, A.S., B.E. Bouma, and M.R.K. Mofrad, *A combined FEM/genetic algorithm for vascular soft tissue elasticity estimation.* Cardiovascular Engineering, 2006. **6**(3): p. 93-102.
140. Wang, C., et al., *Three-dimensional mechanical properties of porcine coronary arteries: a validated two-layer model.* American Journal of Physiology-Heart and Circulatory Physiology, 2006. **291**(3): p. H1200-H1209.
141. Yang, T., et al. *Modeling cutting force of laparoscopic scissors*. in *Biomedical Engineering and Informatics (BMEI), 2010 3rd International Conference on*. 2010. IEEE.
142. Skovoroda, A., S. Emelianov, and M. O'Donnell, *Tissue elasticity reconstruction based on ultrasonic displacement and strain images.* Ultrasonics, Ferroelectrics and Frequency Control, IEEE Transactions on, 1995. **42**(4): p. 747-765.
143. Bjorkman, G. and R. Richards, *Harmonic Holes---An Inverse Problem in Elasticity.* Journal of Applied Mechanics, 1976. **43**: p. 414.
144. Goldberg, D.E., *Genetic algorithms in search, optimization, and machine learning.* 1989.
145. Paschold, M., et al., *Virtual reality laparoscopy: which potential trainee starts with a higher proficiency level?* International Journal of Computer Assisted Radiology and Surgery, 2011. **6**(5): p. 653-662.

146. Satava, R., *Accomplishments and challenges of surgical simulation.* Surgical Endoscopy, 2001. **15**(3): p. 232-241.
147. De, S., et al., *Assessment of Tissue Damage due to Mechanical Stresses.* The International Journal of Robotics Research, 2007. **26**(11-12): p. 1159-1171.
148. Leong, F., W.-H. Huang, and C.-K. Chui, *Modeling and analysis of coagulated liver tissue and its interaction with a scalpel blade.* Medical & biological engineering & computing, 2013: p. 1-9.
149. Basdogan, C., et al., *Haptics in minimally invasive surgical simulation and training.* Computer Graphics and Applications, IEEE, 2004. **24**(2): p. 56-64.
150. Demiray, H., *Incremental elastic modulus for isotropic elastic bodies with application to arteries.* Journal of Biomechanics, 1983. **105(3)**(0148-0731 (Print)): p. 308-9.
151. Miller, K., et al., *Modelling brain deformations for computer-integrated neurosurgery.* International Journal for Numerical Methods in Biomedical Engineering, 2010. **26**(1): p. 117-138.
152. Velardi, F., F. Fraternali, and M. Angelillo, *Anisotropic constitutive equations and experimental tensile behavior of brain tissue.* Biomechanics and Modeling in Mechanobiology, 2006. **5**(1): p. 53-61.
153. Gasser, T.C., R.W. Ogden, and G.A. Holzapfel, *Hyperelastic modelling of arterial layers with distributed collagen fibre orientations.* Journal of The Royal Society Interface, 2006. **3**(6): p. 15-35.
154. Holzapfel, G., T. Gasser, and R. Ogden, *A New Constitutive Framework for Arterial Wall Mechanics and a Comparative Study of Material Models.* Journal of Elasticity, 2000. **61**(1): p. 1-48.
155. Holzapfel, G.A., *Nonlinear Solid Mechanics: A Continuum Approach for Engineering Science.* Meccanica, 2002. **37**(4): p. 489-490.
156. Ogden, R.W., *Nonlinear elasticity, anisotropy, material stability and residual stresses in soft tissue.* Biomechanics of Soft Tissue in Cardiovascular Systems, 2003. **108**(Springer-Verlag): p. 65-108.
157. T. S. Lee, C.K.J., and W. Choi, *Virtual laparoscopic cholecystectomy simulator using force-feedback device.* J Korean Soc Med Inform, 2001. **7**(2): p. 113-121.
158. R. Webster, R.S.H., G. Zoppetti, A. Benson, J. Boyd, N. Charles, J. Reeser, and S. Sampson, *A haptic surgical simulator for laparoscopic cholecystectomy using real-time deformable organs.* in Proceedings of the IASTED International Conference on Biomedical Engineering, 2003: p. 219-222.
159. Misra, S., K.T. Ramesh, and A.M. Okamura, *Modelling of non-linear elastic tissues for surgical simulation.* Computer Methods in Biomechanics and Biomedical Engineering, 2010. **13**(6): p. 811-818.
160. Doll, S. and K. Schweizerhof, *On the Development of Volumetric Strain Energy Functions.* Journal of Applied Mechanics, 2000. **67**(1): p. 17-21.
161. Horgan, C.O. and J.G. Murphy, *On the volumetric part of strain-energy functions used in the constitutive modeling of slightly compressible solid rubbers.* International Journal of Solids and Structures, 2009. **46**(16): p. 3078-3085.
162. Fung, Y.C., K. Fronek, and P. Patitucci, *Pseudoelasticity of arteries and the choice of its mathematical expression.* American Journal of Physiology - Heart and Circulatory Physiology, 1979. **237**(5): p. H620-H631.
163. Zhang, J., et al. *Gallbladder modeling and simulation in laparoscopic cholecystectomy*. in *Industrial Electronics and Applications (ICIEA), 2011 6th IEEE Conference on*. 2011.

164. Huang, W., et al. *3D shape decomposition and comparison for gallbladder modeling*. 2011. Lake Buena Vista, Florida, USA: SPIE.
165. Frobert O Fau - Gregersen, H., J.P. Gregersen H Fau - Bagger, and J.P. Bagger, *Mechanics of porcine coronary arteries ex vivo employing impedance planimetry: a new intravascular technique.* Annals of Biomedical Engineering, 1995. **24**(0): p. 148-155.
166. Fung, Y., *Biomechanics. Motion, flow, stress, and growth* New York, Springer-Verlag, 1990.
167. Duch, B.U., et al., *Elastic properties in the circumferential direction in isolated rat small intestine.* Acta Physiologica Scandinavica, 1996. **157**(2): p. 157-163.
168. Duch Bu Fau - Andersen, H., H. Andersen H Fau - Gregersen, and H. Gregersen, *Mechanical properties of the porcine bile duct wall.* BioMedical Engineering OnLine, 2004. **3:23**(1475-925X (Electronic)).
169. Zhou, J. and Y.C. Fung, *The degree of nonlinearity and anisotropy of blood vessel elasticity.* Proceedings of the National Academy of Sciences, 1997. **94**(26): p. 14255-14260.
170. Srinivasan, M.A. and C. Basdogan, *Haptics in virtual environments: Taxonomy, research status, and challenges.* Computers & Graphics, 1997. **21**(4): p. 393-404.
171. Feygin, D., M. Keehner, and R. Tendick. *Haptic guidance: Experimental evaluation of a haptic training method for a perceptual motor skill*. in *Haptic Interfaces for Virtual Environment and Teleoperator Systems, 2002. HAPTICS 2002. Proceedings. 10th Symposium on*. 2002. IEEE.
172. Rosell, J., et al., *Motion planning for haptic guidance.* Journal of Intelligent and Robotic Systems, 2008. **53**(3): p. 223-245.
173. Yang, T., et al., *Mechanism of a Learning Robot Manipulator for Laparoscopic Surgical Training*, in *Frontiers of Intelligent Autonomous Systems*2013, Springer. p. 297-308.
174. Coles, T.R., D. Meglan, and N.W. John, *The role of haptics in medical training simulators: a survey of the state of the art.* Haptics, IEEE Transactions on, 2011. **4**(1): p. 51-66.
175. Basdogan, C., C.-H. Ho, and M.A. Srinivasan, *Virtual environments for medical training: graphical and haptic simulation of laparoscopic common bile duct exploration.* Mechatronics, IEEE/ASME Transactions on, 2001. **6**(3): p. 269-285.
176. Yamamoto, T., et al., *Augmented reality and haptic interfaces for robot‐assisted surgery.* The International Journal of Medical Robotics and Computer Assisted Surgery, 2012. **8**(1): p. 45-56.
177. MDl, J.S. and T.W.M. PhDl, *Haptic palpation of Head and Neck cancer patients Implications for education and telemedicine.* Medicine Meets Virtual Reality 2001: Outer Spaces, Inner Space, Virtual Space, 2001. **81**: p. 471.
178. Chen, H., et al., *Dynamic touch‐enabled virtual palpation.* Computer Animation and Virtual Worlds, 2007. **18**(4‐5): p. 339-348.
179. Chui, C.-K., et al., *Haptics in computer-mediated simulation: Training in vertebroplasty surgery.* Simulation & Gaming, 2006. **37**(4): p. 438-451.
180. Ullrich, S. and T. Kuhlen, *Haptic palpation for medical simulation in virtual environments.* Visualization and Computer Graphics, IEEE Transactions on, 2012. **18**(4): p. 617-625.

181. Sandberg, W., *Anesthesia and airway management for tracheal resection and reconstruction.* International anesthesiology clinics, 2000. **38**(1): p. 55-75.
182. Grillo, H.C., *The history of tracheal surgery.* Chest Surg Clin, N. Am, 2003. **13**: p. 175-189.
183. Rich Jt Fau - Gullane, P.J. and P.J. Gullane, *Current concepts in tracheal reconstruction.* Curr Opin Otolaryngol Head Neck, Surg, 2012 Aug. **20(4)**: p. 246-53.
184. Conti, F., et al., *CHAI: An Open-Source Library for the Rapid Development of Haptic Scenes.* 2005.
185. Hwang, Y.K. and N. Ahuja, *A potential field approach to path planning.* Robotics and Automation, IEEE Transactions on, 1992. **8**(1): p. 23-32.
186. Chui, C.-K., H.-T. Loh, and J.-F. Yam, *Simulation Method for Developing Multiple-Use Medical Devices from Re-using and Enhancing Design of Single-Use Device.* Procedia CIRP, 2013. **5**: p. 37-41.
187. Berry, D.A., et al., *A quantitative output-cost ratio in voice production.* Journal of Speech, Language and Hearing Research, 2001. **44**(1): p. 29.
188. Woo, P., et al., *Endoscopic microsuture repair of vocal fold defects.* Journal of voice : official journal of the Voice Foundation, 1995. **9**(3): p. 332-339.
189. W, X., et al., *Shape memory alloy fixator system for suturing tissue in minimal access surgery.* Annals of Biomedical Engineering, 1999(0090-6964 (Print)).
190. Chng, C.B., et al., *A bioabsorbable microclip for laryngeal microsurgery: Design and evaluation.* Acta Biomaterialia, 2012. **8**(7): p. 2835-2844.
191. Lau, D.P., et al., *Development of a microclip for laryngeal microsurgery: Initial animal studies.* The Laryngoscope, 2012. **122**(8): p. 1809-1814.
192. Charara, J., Y.-M. Dion, and R. Guidoin, *Mechanical characterization of endoscopic surgical staples during an experimental Hernia repair.* Clinical Materials, 1994. **16**(2): p. 81-89.
193. Klein, R.D., et al., *Comparison of titanium and absorbable polymeric surgical clips for use in laparoscopic cholecystectomy.* Surgical Endoscopy, 1994. **8**(7): p. 753-758.
194. Min Tan, T. and M. Okada, *The efficiency of absorbable clips in minimally invasive surgery.* Surgery Today, 1999. **29**(8): p. 828-831.
195. Staiger, M.P., et al., *Magnesium and its alloys as orthopedic biomaterials: A review.* Biomaterials, 2006. **27**(9): p. 1728-1734.
196. Choo, J.Q., et al., *Design of a Mechanical Larynx With Agarose as a Soft Tissue Substitute for Vocal Fold Applications.* Journal of Biomechanical Engineering, 2010. **132**(6): p. 065001-7.
197. Seitz, J.M., et al., *Magnesium degradation products: Effects on tissue and human metabolism.* Journal of Biomedical Materials Research Part A, 2013(00A): p. p.000-000.
198. Peng, Q., et al., *Effects of backward extrusion on mechanical and degradation properties of Mg–Zn biomaterial.* Journal of the Mechanical Behavior of Biomedical Materials, 2012. **10**(0): p. 128-137.
199. Heljak, M.K., et al., *Evolutionary design of bone scaffolds with reference to material selection.* International Journal for Numerical Methods in Biomedical Engineering, 2012. **28**(6-7): p. 789-800.
200. Cukjati, D., S. Reberšek, and D. Miklavčič, *A reliable method of determining wound healing rate.* Medical and Biological Engineering and Computing, 2001. **39**(2): p. 263-271.

201. Haisch, A., et al., *Preparation of a pure autologous biodegradable fibrin matrix for tissue engineering.* Medical and Biological Engineering and Computing, 2000. **38**(6): p. 686-689.
202. Song, G., *Control of biodegradation of biocompatable magnesium alloys.* Corrosion Science, 2007. **49**(4): p. 1696-1701.
203. Witte, F., et al., *In vitro and in vivo corrosion measurements of magnesium alloys.* Biomaterials, 2006. **27**(7): p. 1013-1018.
204. Gu, X., et al., *In vitro corrosion and biocompatibility of binary magnesium alloys.* Biomaterials, 2009. **30**(4): p. 484-498.
205. Witte, F., et al., *Degradable biomaterials based on magnesium corrosion.* Current Opinion in Solid State and Materials Science, 2008. **12**(5–6): p. 63-72.
206. Kirkland, N.T., et al., *A survey of bio-corrosion rates of magnesium alloys.* Corrosion Science, 2010. **52**(2): p. 287-291.
207. Song, Y., et al., *Electrodeposition of Ca–P coatings on biodegradable Mg alloy: In vitro biomineralization behavior.* Acta Biomaterialia, 2010. **6**(5): p. 1736-1742.
208. Mueller, W.-D., M. Lucia Nascimento, and M.F. Lorenzo de Mele, *Critical discussion of the results from different corrosion studies of Mg and Mg alloys for biomaterial applications.* Acta Biomaterialia, 2010. **6**(5): p. 1749-1755.
209. Lévesque, J., et al., *Design of a pseudo-physiological test bench specific to the development of biodegradable metallic biomaterials.* Acta Biomaterialia, 2008. **4**(2): p. 284-295.
210. Bobby Kannan, M., et al., *Stress corrosion cracking of rare-earth containing magnesium alloys ZE41, QE22 and Elektron 21 (EV31A) compared with AZ80.* Materials Science and Engineering: A, 2008. **480**(1–2): p. 529-539.
211. Gu, X.N., et al., *Corrosion fatigue behaviors of two biomedical Mg alloys – AZ91D and WE43 – In simulated body fluid.* Acta Biomaterialia, 2010. **6**(12): p. 4605-4613.
212. Liu, L.J. and M. Schlesinger, *Corrosion of magnesium and its alloys.* Corrosion Science, 2009. **51**(8): p. 1733-1737.
213. Deshpande, K.B., *Numerical modeling of micro-galvanic corrosion.* Electrochimica Acta, 2011. **56**(4): p. 1737-1745.
214. Dietzel, W., M. Pfuff, and N. Winzer, *Testing and mesoscale modelling of hydrogen assisted cracking of magnesium.* Engineering Fracture Mechanics, 2010. **77**(2): p. 257-263.
215. Scheiner, S. and C. Hellmich, *Stable pitting corrosion of stainless steel as diffusion-controlled dissolution process with a sharp moving electrode boundary.* Corrosion Science, 2007. **49**(2): p. 319-346.
216. Gervaso, F., et al., *On the effects of different strategies in modelling balloon-expandable stenting by means of finite element method.* Journal of Biomechanics, 2008. **41**(6): p. 1206-1212.
217. Kiousis, D., A. Wulff, and G. Holzapfel, *Experimental Studies and Numerical Analysis of the Inflation and Interaction of Vascular Balloon Catheter-Stent Systems.* Annals of Biomedical Engineering, 2009. **37**(2): p. 315-330.
218. Mori, K. and T. Saito, *Effects of Stent Structure on Stent Flexibility Measurements.* Annals of Biomedical Engineering, 2005. **33**(6): p. 733-742.
219. Petrini, L., et al., *Numerical investigation of the intravascular coronary stent flexibility.* Journal of Biomechanics, 2004. **37**(4): p. 495-501.
220. Marrey, R.V., et al., *Fatigue and life prediction for cobalt-chromium stents: A fracture mechanics analysis.* Biomaterials, 2006. **27**(9): p. 1988-2000.

221. Pelton, A.R., et al., *Fatigue and durability of Nitinol stents.* Journal of the Mechanical Behavior of Biomedical Materials, 2008. **1**(2): p. 153-164.
222. Pericevic, I., et al., *The influence of plaque composition on underlying arterial wall stress during stent expansion: The case for lesion-specific stents.* Medical engineering & physics, 2009. **31**(4): p. 428-433.
223. Miller, N.D. and D.F. Williams, *The in vivo and in vitro degradation of poly(glycolic acid) suture material as a function of applied strain.* Biomaterials, 1984. **5**(6): p. 365-368.
224. Chu, C.C., *Strain-Accelerated Hydrolytic Degradation of Synthetic Absorbable Sutures*. Surgical Research - Recent Developments, ed. C.W. Hall1985, New York: Pergamon Press.
225. Liu, B. and Y. Huang, *The Stable Finite Element Method for Minimization Problems.* Journal of Computational and Theoretical Nanoscience, 2008. **5**(7): p. 1251-1254.
226. Young, W.C. and R.G. Budynas, *Roark's formulas for stress and strain*. Vol. 6. 2002, New York: McGraw-Hill.
227. Zimmer, C., et al., *Segmentation and tracking of migrating cells in videomicroscopy with parametric active contours: a tool for cell-based drug testing.* IEEE Transactions on Medical Imaging, 2002. **21**(10): p. 1212-1221.
228. Brown, J.D., et al., *In-vivo and in-situ compressive properties of porcine abdominal soft tissues.* Studies in Health Technology and Informatics, 2003: p. 26-32.
229. Choi, A.P.C. and Y.P. Zheng, *Estimation of Young's modulus and Poisson's ratio of soft tissue from indentation using two different-sized indentors: Finite element analysis of the finite deformation effect.* Medical and Biological Engineering and Computing, 2005. **43**(2): p. 258-264.
230. Moore, J., J. Soares, and K. Rajagopal, *Biodegradable stents: biomechanical modeling challenges and opportunities.* Cardiovascular Engineering and Technology, 2010. **1**(1): p. 52-65.
231. A Preetha, R.B., *Comparison of Artificial Saliva Substitutes.* Trends in Biomaterials and Artificial Organs, 2005. **Vol 18**: p. 178-86.
232. *ASTM G31 - 72: Standard Practice for Laboratory Immersion Corrosion Testing of Metals*2004, Philadelphia, PA: Annual Book of ASTM Standards, American Society for Testing and Materials.
233. Grogan, J.A., et al., *A corrosion model for bioabsorbable metallic stents.* Acta Biomaterialia, 2011. **7**(9): p. 3523-3533.
234. Wu, W., et al., *Finite element analyses for design evaluation of biodegradable magnesium alloy stents in arterial vessels.* Materials Science and Engineering: B, 2011. **176**(20): p. 1733-1740.
235. Melvin, J., et al. *Impact injury mechanisms in abdominal organs*. in *Proceedings: Stapp Car Crash Conference*. 1973. Society of Automotive Engineers SAE.

List of publication

Journals:

L. Xiong, C.K. Chui, and C.L. Teo: 'Reality based modeling and simulation of gallbladder shape deformation using variational methods', **International Journal of Computer Assisted Radiology and Surgery**, 2013. **8**(5):p. 857-865.

L.F. Xiong, C.K. Chui, C.L. Teo, D.P.C. Lau. 'Modeling and simulation of material degradation in biodegradable wound closure devices'. **J Biomed Mater Res Part B**, 2013.00B:p.000–000.

L.F. Xiong, C.K. Chui,Y.B. Fu, C.L. Teo. 'Characterization of human artery tissue using probabilistic approach and genetic algorithms'. Submitted to **International Journal of Computer Assisted Radiology and Surgery**.

Conferences:

L.F.Xiong, C.K. Chui, C.L. Teo, D. Lau. 'Incremental Potential Field Based Haptic Guidance for Medical Simulation'. **2013 IEEE/SICE Internal Symposium on System Integration** (**SII-2013**) 2013, pp.772-777.

Xiong, L.; Yang, T.; Chui, C.K.; Teo, C.L.;Huang, W.;Liu, J.;Su, Y.;Chang, S.: 'Analysis of Vascular Soft Tissue Division with Laparoscopic scissors'. **International Conference on Biomedical Engineering and Biotechnology (BEB),** 2011, Oral presentation.

Xiong Linfei; Chui Chee Kong; Teo Chee Leong; 'Elasticity Estimation of Material Properties for Soft Tissue Deformation using Genetic Algorithm'. **7th Asian Conference on Computer-Aided Surgery** (ACCAS), 2011, Oral presentation.

Yang, T.; Xiong, L.; Zhang, J.; Yang, L.; Huang, W.; Zhou, J.; Liu, J.; Su, Y.; Chui, C.K.; Teo, C.L.; Chang, S.: 'Modeling cutting force of laparoscopic scissors', **Biomedical Engineering and Informatics (BMEI)**, 2010, pp. 1764 – 1768.

C.K. Chui, L.F. Xiong, C.L. Teo, D. Lau. 'Modeling and Simulating Material Degradation in Bioresorbable Wound Closure Devices'. **Computer Graphics International(CGI),** 2011, Poster section.